COMPUTATIONAL AND HYBRID SIMULATION OF HIGH PERFORMANCE FIBER REINFORCED CONCRETE COUPLED WALL SYSTEMS

by

Chung-Chan Hung

A dissertation submitted in partial fulfillment
of the requirements for the degree of
Doctor of Philosophy
(Civil Engineering)
in The University of Michigan
2010

Doctoral Committee:

Professor Sherif El-Tawil, Chair
Professor Carlos E. S. Cesnik
Professor James K. Wight
Associate Professor Gustavo J. Parra-Montesinos

DEDICATION

To my parents
Ping-Ho Hung and Kang-Yu Hung

To my wife
Shan-Ni Chen

To my sisters and brothers in law

ACKNOWLEDGMENTS

I would like to dedicate this dissertation to my beloved family. Your eternal love for me transforms into the greatest support and inspiration in my life. I am pursuing my life for distributing our boundless love.

Thanks to my doctoral dissertation advisor, Prof. Sherif El-Tawil, for the profound inspiration and guide you have consistently given to me both for my research work and life. What I have learned from you will benefit my entire life deeply. Thanks to my dissertation committee members, Prof. James K. Wight, Prof. Gustavo J. Parra-Montesinos, and Prof. Carlos E. S. Cesnik, for your help at the different stages of my pursuit for the Ph.D. degree. Thanks to Prof. Jeremy Lynch for being a great guide and friend. Thanks to the entire CEE community at the University of Michigan, Ann Arbor, for providing such a comfortable environment for me to live and learn.

I am also lucky to have a group of supportive colleagues, Dr. Kittinun, Dr. Khandelwal, Dr. Ekiz, Dr. Kim, Dr. Supat, Dr. Yasser, Dr. Wille, Remy, Matt, Phillip, Honghao, and Jieshi. Thank you for always being so generous in giving me your kindness and help.

Thanks to all my friends in Ann Arbor and Taiwan for sharing your love with me.

TABLE OF CONTENTS

LIST OF FIGURES

LIST OF TABLES

ABSTRACT

High performance fiber reinforced concretes (HPFRCs) are characterized by pseudo-ductile tensile strain-hardening behavior, large energy absorption prior to crack localization and confined-like compressive response. These properties imply that HPFRCs have the potential to serve as highly damage tolerant and energy absorbing materials under severe loading conditions. A structural system that could significantly benefit from the use of HPFRC is reinforced concrete (RC) coupled wall systems (CWSs). Therefore, the overall objective of this work is to investigate, through computational and hybrid simulation techniques, the seismic behavior of RC CWSs in which HPFRC is used to replace regular concrete in vulnerable regions of the structure.

In order to simulate the hysteretic behavior of HPFRC structural components under random displacement reversals, an inelastic HPFRC material model is developed using a new mixed rotating/fixed smeared crack formulation. Two 18-story CWSs, one RC and the other containing HPFRC in the coupling beams and wall plastic hinge zones, are designed and their seismic responses investigated. The latter system is designed with less reinforcing steel and reduced detailing than the former in recognition of the beneficial effects of HPFRC. Comparisons between the seismic performances of both systems indicate that the HPFRC system has an enhanced energy dissipation pattern and less post-

event damage than the RC system despite the reduction in reinforcement quantity and detailing.

In addition to conventional computational simulation, hybrid simulation is also employed to model the seismic behavior of HPFRC CWSs. A strategy for estimating the tangent stiffness of structures during hybrid simulation is proposed. It is shown that when the strategy is combined with the widely used Operator Splitting Method (OSM) for hybrid simulation, the simulation accuracy is enhanced compared to the traditional OSM. A new conditionally stable algorithm, called Full Operator Method (FOM) is also developed. It is shown that FOM has enhanced accuracy compared to OSM and that it is possible to modify FOM into an unconditionally stable algorithm for cases where the estimated tangent stiffness is larger than the real tangent stiffness. Hybrid simulation of an 18-story prototype with FOM indicates that the new technique is able to model seismic behavior of CWSs with reasonable accuracy.

CHAPTER 1

INTRODUCTION

1.1 GENERAL

High performance fiber reinforced concrete (HPFRC) is a class of materials that have properties that are attractive to structural engineers. These materials are characterized by pseudo-ductile tensile strain-hardening behavior after first cracking (Fig. 1.1) accompanied by multiple cracks and large energy absorption prior to crack localization (Li 2003; Naaman and Reinhardt 2006). After crack localization, which typically occurs at strains ranging between 0.5% and 4% (about 2 orders of magnitude greater than traditional concrete), the material strain-softens gradually and further deformation demand is accommodated within a single growing crack or band of cracks (Kim et al. 2009). In compression, HPFRC materials behave like confined concrete, i.e. the material has greater ductility compared to regular concrete due to the confining effect introduced by the fibers. These properties imply that HPFRC have the potential to serve as highly damage tolerant and energy absorbing materials under severe loading conditions. In fact, good response has been observed in HPFRC members subjected to tension, shear, and bending under both monotonic and reversed cyclic loading (Otter and Naaman 1998; Parra-Montesinos 2005; Canbolat et al. 2005; Parra-Montesinos et al. 2006; Parra-

Montesinos and Chompreda 2007). An advantage of the confining effect introduced by the embedded fibers in HPFRC is that it makes it feasible to reduce required confining reinforcement in critical regions of a structure, simplifying construction details, eliminating steel congestion and reducing construction costs (Parra-Montesinos 2005; Parra-Montesinos et al. 2006; Parra-Montesinos and Chompreda 2007; Canbolat et al. 2005). The potential of using HPFRC materials for structural retrofit applications has also been recognized and explored (Kesner and Billington 2005).

A structural system that could potentially benefit from the use of HPFRC is reinforced concrete (RC) coupled wall systems. Such systems are often used in mid- to high-rise structural systems in zones of high seismic risk to provide lateral resistance to earthquake loading. Coupled wall systems are comprised of two or more wall piers in series connected via RC coupling beams (Fig. 1.2). Under seismic action, the coupling beams must transfer adequate force between adjacent walls and, at the same time, are expected to contribute significantly to energy dissipation when undergoing inelastic deformation. These stringent requirements usually result in a dense configuration of reinforcement, which complicates erection of RC coupled wall systems. Furthermore, as a result of the way a coupled wall system deforms (Fig. 1.3), most of the inelastic behavior in wall piers takes place in a limited plastic hinge zone at the base of the piers. Since the deformation demands are expected to be high in plastic hinge zones, such regions are usually heavily confined to assure good response under reversed cyclic behavior. The good characteristics of HPFRC have the potential for alleviating some of the previously

mentioned difficulties, by reducing reinforcement congestion in the coupling beams and plastic hinge zones.

Experimental studies on individual coupling beams have shown that using HPFRC to replace traditional concrete material can allow a reduction in reinforcing details while still providing satisfactory performance, i.e. strength and deformation capacity (Canbolat et al. 2005; Wight and Lequesne 2008; Lequesne et al. 2009). Other studies have also shown that the use of HPFRC in the plastic hinge zone is beneficial (Parra-Montesinos et al. 2006) by reducing confinement steel and required shear reinforcement. As indicated, only a few sets of studies were performed on single structural components, and there have been only limited studies (Lequesne et al. 2010) to confirm and study the overall effectiveness of using HPFRC in RC coupled wall systems.

The premise of this dissertation is that using HPFRC to replace regular concrete in critical parts of coupled wall systems, namely coupling beams and plastic hinge zones, will result in good seismic response of the system. This acceptable performance will, however, be achieved with a significant reduction in steel detailing requirements, and perhaps overall steel reinforcement. It is hypothesized that the expected improvements in contstructibility, manifested as a reduction in construction time and cost, as well as reduction in steel reinforcement, will offset the added cost of using HPFRC in selected small portions of the system. The effectiveness of using HPFRC for improving system response is studied using two modeling techniques applied to a coupled wall prototype system, namely traditional computational simulation and the hybrid simulation method.

1.1.1 Computational simulation of coupled wall systems

Traditional computational simulation models as applied to HPFRC can be broadly categorized by their resolution in modeling nonlinear behavior as micro-scale models, macro-scale models, and structural-scale models. Micro-scale models describe the behavior of and interaction among the three phases of the material, i.e. fiber, matrix, and interfacial zones. Macro-scale models, on the other hand, focus on phenomenological behavior at the point level. They are capable of explicitly accounting for key phenomena such as hardening and softening in compression, crushing behavior, and post-cracking and post-peak response in tension. Structural-scale models implicitly capture the essence of structural behavior at the domain level, for example, cross-sectional moment versus curvature behavior and panel shear force versus distortion relationships. They are generally favored by practitioners because they are computationally expedient and because they produce data that is intuitive and that deals directly with design variables such as moments, rotations, etc. Sirijaroonchai (2009) discusses examples of HPFRC models for each of these categories.

Since micro-scale models focus on the behavior of the constituents of HPFRC, they have high computational demands that severely limit their use in analysis applications involving large structures. Structural-scale models lack the resolution needed to understand detailed structural response. Macro-scale models, on the other hand, are significantly more computationally efficient than micro-scale models because they capture the overall response and at the same time can provide detailed information about

local response. They can therefore be practically used in continuum finite element simulations of large structural systems. Based on this rationale, the focus of this dissertation is to develop a 2-D macro-scale model for computational simulation of HPFRC structural systems.

1.1.2 Hybrid simulation of coupled wall systems

Over the past 3 decades, the development of the hybrid simulation technique for evaluation of structural seismic performance has evolved rapidly (Takanashi et al. 1978; Shing and Mahin 1984; Takanashi and Nakashima 1987; Mahin and Shing 1985; Thewalt and Mahin 1987; Nakashima et al. 1990; Shing et al. 1990; Shing and Vannan 1991; Nakashima et al. 1992; Shing et al. 1994; Thewalt and Mahin 1994; Combescure and Pegon 1997; Molina et al. 1999; Nakashima and Masaoka 1999; Darby et al. 1999; Darby et al. 2001; Wu et al. 2005; Zhang et al. 2005; Pan et al. 2006; Ghaboussi et al. 2006; Pan et al. 2006; Bonnet et al. 2007; Wu et al. 2007; Ahmadizadeh and Mosqueda 2008; Hung and Sherif 2009a,b). Hybrid simulation is a technique, which combines the advantage of physical testing and conventional numerical simulation for evaluation of a structure's seismic behavior. In hybrid simulation, a structure can be divided into several substructures. Each of these structures is either physically tested in a laboratory or numerically modeled in a computer. Like the conventional numerical method, hybrid simulation uses a discrete-mass model to represent the continuous system and uses time-stepping integration method to calculate the history response of a structure under an earthquake. The major difference between hybrid simulation and traditional numerical method is that the term of the restoring force in the equation of motion, representing the

discrete mass system, is obtained directly from each substructure that is tested either physically or numerically. One advantage of hybrid simulation is that it allows geographically-distributed simulation (Kwon et al. 2008), in which substructures are tested or simulated at different sites and the information of the substructures' responses at each time step is sent to a main computer through a network to calculate the system response of the next time step. Furthermore, using hybrid simulation allows combining the capabilities of various finite element analysis packages. Due to its capabilities, the hybrid simulation technique is used to study the seismic behavior of HPFRC coupled wall systems in addition to the traditional computational method.

1.2 RESEARCH OBJECTIVES

The overall goal of this study is to investigate, through computational and hybrid simulation techniques, the inelastic dynamic response of coupled wall systems in which HPFRC is used to replace regular concrete in critical, damage prone parts of the system, such as coupling beams and wall plastic hinge zones. Specific objectives are:

1) Develop a robust HPFRC macro model capable of modeling the hysteretic response of regular concrete and at the same time able to address the unique strain hardening behavior of HPFRC.

2) Use traditional computational simulation to compare between the seismic responses of traditional RC coupled wall systems and modified systems in which HPFRC is employed.

3) Develop new hybrid simulation tools that can be applied to model the inelastic behavior of coupled wall systems.

1.3 DISSERTATION OUTLINE

This dissertation is comprised of 7 chapters. Chapter 1 is an introduction. Chapter 2 addresses research objective 1, while Chapter 3 addresses objective 2. Chapters 4 to 6 address objective 3, while Chapter 7 summarizes the work and draws key conclusions. Following is a more detailed description of each chapter.

Chapter 1: *Introduction*. This chapter provides an overview of the research. The objectives and the structure of the dissertation are also provided.

Chapter 2: *Hybrid rotating/fixed-crack model for high performance fiber reinforced cementitious composites*. This chapter presents a new HPFRC material model based on a plane-stress, orthogonal, mixed rotating/fixed-crack approach that can be used for modeling the 2-D behavior of HPFRC structural members and systems subjected to reversed cyclic loading. The performance of the proposed material model is demonstrated through comparisons of experimental and numerical results from a series of tests on various HPFRC structural components.

Chapter 3: *Seismic behavior of a coupled-wall system with HPFRC materials in critical regions*. This chapter investigates the effectiveness of using HPFRC material in the critical components of a coupled wall system for enhanced seismic performance. The

seismic performance of the prototype HPFRC coupled wall system is evaluated using several parameters, such as the interstory drift and the rotation of coupling beams and shear walls. The seismic performance of the HPFRC system is compared with that of a conventional RC coupled wall system.

Chapter 4: *A method for estimating specimen tangent stiffness for hybrid simulation*. This chapter suggests a method to estimate structures' tangent stiffness during hybrid simulation. The use of estimated tangent stiffness is shown to be able to increase the simulation accuracy when combined with existing hybrid simulation algorithms. The enhanced simulation accuracy is shown via an energy error index.

Chapter 5: Full Operator algorithm for hybrid simulation. This chapter presents a new algorithm for hybrid simulation. The algorithm, consisting of a predictor and a corrector, is shown to be a good candidate to simulate structures with nonlinear behavior. The effect of displacement control errors on the proposed algorithm is studied. In addition, the stability characteristics of the newly developed Full Operator Method are investigated. Based on the investigation result, a modified Full Operator Method is proposed for improved stability. The stability and accuracy characteristics of the modified Full Operator Method are then discussed.

Chapter 6: *Hybrid simulation of HPFRC coupled wall systems*. An interface connecting the hybrid simulation platform, UI-SimCor, and a finite element analysis package, LS-DYNA, is developed in this chapter. The enhanced Full Operator Method is combined

with the interface to conduct hybrid simulation of the prototype HPFRC coupled wall system. The capabilities of hybrid simulation and the modified Full Operator Method are discussed in light of the simulation result.

Chapter 7: *Summary, conclusions, and future research*. This chapter provides a summary of this research study. Conclusions from the results and from the previous chapters are drawn and future work is recommended.

1.4 PUBLICATIONS FROM THIS DISSERTATION

In this dissertation, Chapter 4 and the first half of Chapter 5 are published as journal papers. Chapter 2 and the second half of Chapter 5 have been submitted for publication, and Chapter 3 and 6 are in preparation and will soon be submitted for publication. Details are listed as below:

C.C. Hung, S. El-Tawil. Hybrid Rotating/Fixed-Crack Model for High Performance Fiber Reinforced Cementitious Composites. *ACI Materials Journal (submitted, July 2009).* **(Chapter 2)**

C.C. Hung, S. El-Tawil. Seismic Performance of Midrise High Performance Fiber Reinforced Cementitious Composite Coupled Wall Systems. *Journal of Structural Engineering (in preparation).* **(Chapter 3)**

C.C. Hung, S. El-Tawil. A Method for Estimating Specimen Tangent Stiffness for Hybrid Simulation. *Earthquake Engineering and Structural Dynamics*. V38, p115-p134, 2009. **(Chapter 4)**

C.C. Hung, S. El-Tawil. Full Operator Algorithm for Hybrid Simulation. *Earthquake Engineering and Structural Dynamics* V38, p1545-1561, 2009. **(Chapter 5)**

C.C. Hung, S. El-Tawil. Stability Characteristics of the Full Operator Method for HybridSimulation. *Engineering Structures (submitted).* **(Chapter 5)**

C.C. Hung, S. El-Tawil. Numerical Hybrid Simulation of a High Performance Fiber Reinforced Cementitious Composites Coupled Wall System. *Earthquake Engineering and Structural Dynamic (in preparation).* **(Chapter 6)**

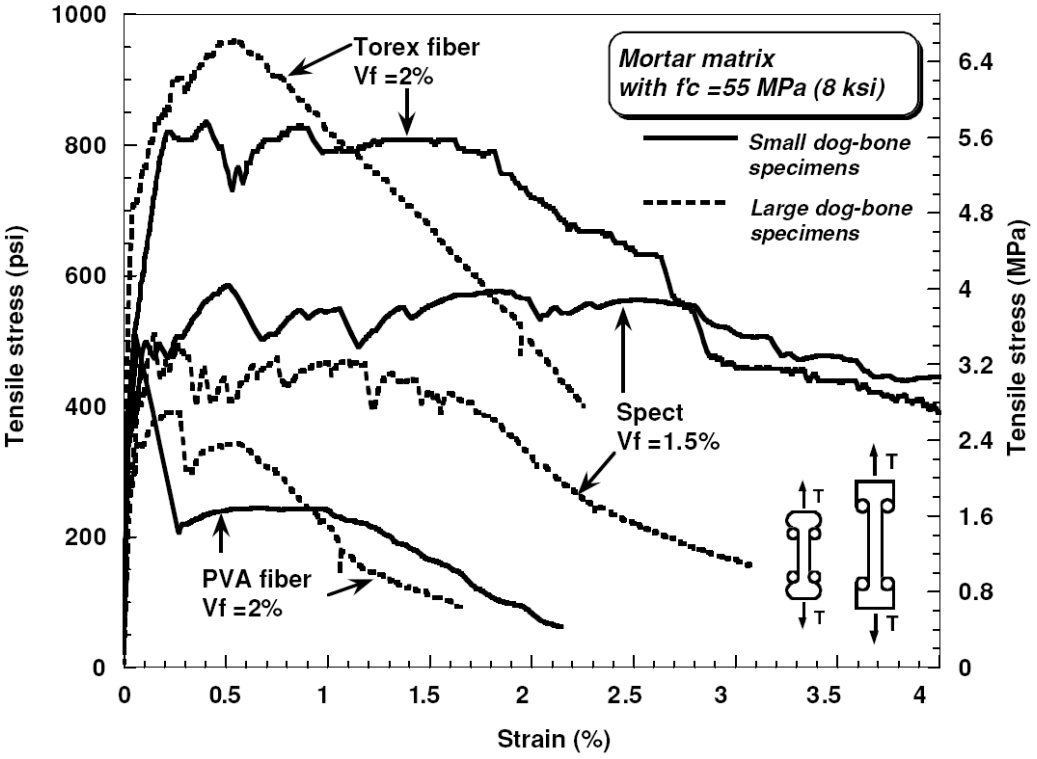

Fig. 1.1 - Typical monotonic stress-strain relationship of HPFRC materials (Naaman and Reinhardt 2006)

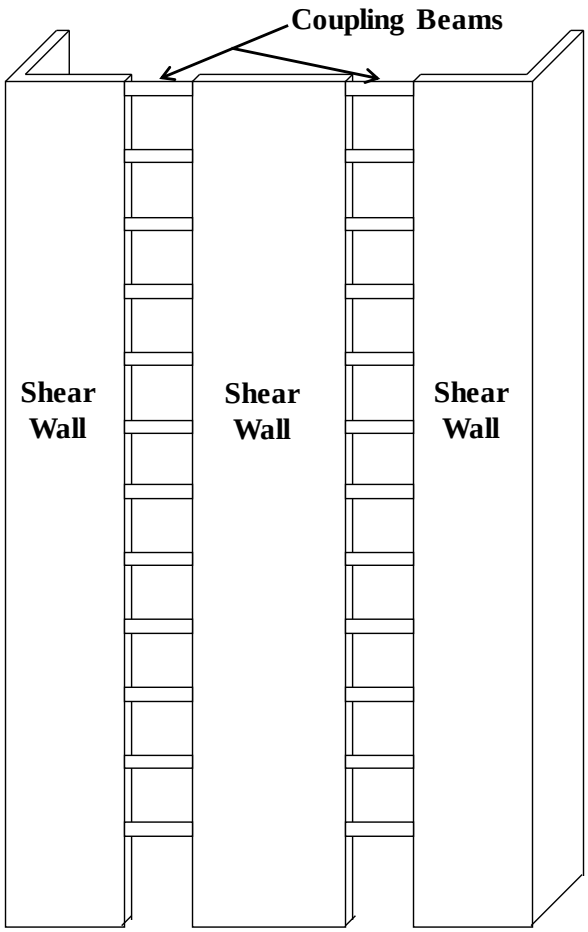

Fig. 1.2 - Coupled wall system

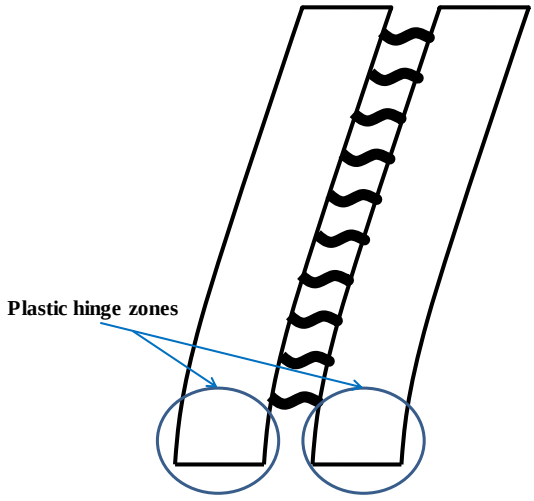

Fig. 1.3 - Deformed coupled wall system

1.5 REFERENCES

Ahmadizadeh MA, Mosqueda G. Hybrid simulation with improved operator-splitting integration using experimental tangent stiffness matrix estimation. Journal of Structural Engineering (ASCE) 2008; 134(12):1829-1838.

Bonnet P, Lim C, Williams M, Blakeborough A, Neild S, Stoten D, Taylor C. Real-time hybrid experiments with Newmark integration, MCSmd outer-loop control and multi-tasking strategies. Journal of Earthquake Engineering and Structural Dynamics 2007; 36:119–141.

Canbolat BA, Parra-Montesinos GJ, and Wight JK. Experimental study on the seismic behavior of high-performance fiber reinforced cement composite coupling beams. ACI Structural Journal 2005; 102(1):159-166.

Combescure D, Pegon P. α-operator splitting time integration technique for pseudodynamic testing. error propagation analysis, Soil Dynamics and Earthquake Engineering 1997; 16(7-8): 427-443.

Darby AP, Blakeborough A, Williams MS. Real-time substructure tests using hydraulic actuator. Journal of Engineering Mechanics (ASCE) 1999; 125(10):1133-1139.

Darby AP, Blakeborough A, Williams MS. Improved control algorithm for real-time substructure testing. Earthquake Engineering and Structural Dynamics 2001; 30:431-448.

Ghaboussi J, Yun G, Hashash Y. A novel predictor-corrector algorithm for sub-structure pseudo-dynamic testing. Journal of Earthquake Engineering and Structural Dynamics 2006; 35:453–476.

Hung C, El-Tawil S. A method for estimating specimen tangent stiffness for hybrid simulation. Earthquake Engineering and Structural Dynamics 2009a; 38: 115-134.

Hung C, El-Tawil S. Full operator algorithm for hybrid simulation. Earthquake Engineering and Structural Dynamics 2009b; 38:1545-1561.

Kesner KE, Billington SL. Investigation of infill panels made from engineered cementitious composites for seismic strengthening and retrofit. Journal of Structural Engineering (ASCE) 2005; 131(11):1712-1720.

Kim DJ, El-Tawil S, Naaman AE. Rate-dependent tensile behavior of high performance fiber reinforced cementitious composites. Materials and Structures 2009; 42(3): 399-414.

Kwon O, Elnashai AS, Spencer BF. A framework for distributed analytical and hybrid Simulations. Structural Engineering and Mechanics 2008; 30(3): 331-350.

Lequesne RD, Setkit M, Parra-Montesinos GJ, Wight JK. Seismic detailing and behavior of coupling beams incorporating high-performance fiber reinforced concrete. Antoine E. Naaman Symposium – Four decades of progress in prestressed concrete, fiber reinforced concrete, and thin laminate composites, SP-XX, American Concrete Institute, Farmington Hills, MI, 2009; 14 pp.

Lequesne RD, Wight JK, Parra-Montesinos GJ. Seismic detailing and behavior of coupled-wall systems with high-performance fiber-reinforced concrete," Joint 9USN/10CCEE Conference Proceedings, Toronto, Canada, July 25-29,2010; 10 pp

Li VC. On engineered cementitious composites (ECC) – A Review of the Material and Its Applications. Journal of Advanced Concrete Technology 2003; 1(3): 215-230.

Mahin SA, Shing PB. Pseudodynamic method for seismic testing. Journal of Structural Engineering (ASCE) 1985; 111(7):1482-1503.

Molina FJ, Verzeletti G, Magonette G, Buchet P, Geradin M. Bi-directional pseudodynamic test of a full-size three-storey building. Earthquake Engineering and Structural Dynamics 1999; 28:1541-1566.

Naaman AE, Reinhardt HW. Proposed classification of HPFRC composites based on their tensile response. Materials and Structures 2006; 39:547-555.

Nakashima M, Kaminosono T, Ishida M, Ando K. Integration techniques for substructure pseudo dynamic test. 4th U.S. National Conference on Earthquake Engineering, Palm Springs, California, 1990; 515-524.

Nakashima M, Kato H, Takaoka E. Development of real-time pseudo dynamic testing. Earthquake Engineering and Structural Dynamics 1992; 21:79-92.

Nakashima M, Masaoka N. Real-time on-line test for MDOF systems. Earthquake Engineering and Structural Dynamics 1999; 28:393-420.

Otter DE, Naaman AE. Properties of steel fiber reinforced concrete under cyclic loading. ACI Materials Journal 1988; 85(4): 254-261.

Pan P, Tomofuji H, Wang T, Nakashima M, Ohsaki M, Mosalam KM. Development of peer-to-peer (P2P) Internet online hybrid test system. Journal of Earthquake Engineering and Structural Dynamics 2006; 35:867-890.

Parra-Montesinos GJ. High-performance fiber reinforced cement composites: an alternative for seismic design of structures. ACI Structural Journal 2005; 102(5):668-675.

Parra-Montesinos GJ, Canbolat BA, Jeyaraman G. Relaxation of confinement reinforcement requirements in structural walls through the use of fiber reinforced cement composites. 8th National Conference on Earthquake Engineering Apr. 2006, San Francisco, CA.

Parra-Montesinos, GJ, Chompreda P. Deformation capacity and shear strength of fiber reinforced cement composite flexural members subjected to displacement reversals. Journal of Structural Engineering (ASCE) 2007; 133(3):421-431.

Shing PB, Mahin SA. Pseudodynamic test method for seismic performance evaluation: Theory and implementation. Report No. UCB/EERC-84/12. Earthquake Engineering Research Center, University of California, Berkeley, 1984.

Shing PB, Vannan MT, Carter E. Evaluation of reinforced masonry shear wall components by pseudodynamic testing. Proceedings of the 4th U.S. National Conference on Earthquake Engineering, Palm Springs, California, 1990; 829-838.

Shing PB, Vannan MT, Cater E. Implicit time integration for pseudodynamic tests. Earthquake Engineering and Structural Dynamics 1991; 20:551-576.

Shing PB, Bursi OS, Vannan MT. Pseudodynamic tests of a concentrically braced frame using substructuring techniques. Journal of Constructional Steel Research 1994; 29:121-148.

Sirijaroonchai K. A macro-scale plasticity model for high performance fiber cement composites. Ph.D. Dissertation, Department of Civil and Environmental Engineering, the University of Michigan, Ann Arbor, 2009.

Takanashi K, Udagawa K, Seki M, Okada T, Tanaka K. Earthquake response analysis of steel frames by computer-actuator on-line system. Proceedings of the 5th Japan Earthquake Engineering Symposium, Tokyo, Japan, November 1978; 1321-1328.

Takanashi K, Nakashima M. Japanese activities on on-line testing. Journal of Structural Engineering (ASCE) 1987; 113(7):1014-1032.

Thewalt CR, Mahin SA. Hybrid solution techniques for generalized pseudodynamic testing. Report No. UCB/EERC-87/09, Earthquake Engineering Research Center, University of California, Berkeley, 1987.

Thewalt CR, Mahin SA. An unconditionally stable hybrid pseudodynamic algorithm. Earthquake Engineering and Structural Dynamics 1994; 24:723-731.

Wight JK, Lequesne RD. Earthquake-resistant design of coupling beam elements incorporating high-performance fiber reinforced concrete. Proceedings of International Seminar on Seismic-Resistant Design of Reinforced Concrete Structures, Bogota, D.C., Columbia, May 15 2008; 97-108.

Wu B, Bao H, Ou J, Tian S. Stability and accuracy analysis of central difference method for real-time substructure testing. Earthquake Engineering and Structural Dynamics 2005; 34:705-718.

Wu B, Xu G, Wang Q, Williams M. Operator-splitting method for real-time substructure testing. Journal Earthquake Engineering and Structural Dynamics 2006; 35:293–314.

Wu B, Wang QY, Shing PB, Ou JP. Equivalent force control method for generalized real-time substructure testing with implicit integration. Journal of Earthquake Engineering and Structural Dynamics 2007; 36:1127–1149.

Zhang Y, Sause R, Ricles JM, Naito CJ. Modified predictor-corrector numerical scheme for real-time pseudo dynamic tests using state-space formulation. Earthquake Engineering and Structural Dynamics 2005; 34:271-288.

CHAPTER 2

HYBRID ROTATING/FIXED-CRACK MODEL FOR HIGH PERFORMANCE FIBER REINFORCED CEMENTITIOUS COMPOSITES[1]

2.1 INTRODUCTION

High performance fiber reinforced cementitious composite (HPFRCC) materials are distinguished from conventional concrete materials by their unique strain hardening behavior in tension, which translates into enhanced shear and bending resistance at the structural level (Naaman and Reinhardt 2006). The favorable properties of HPFRCC have motivated researchers to explore using the material to replace traditional concrete in critical elements of a structure for seismic applications and structural retrofit (Parra-Montesinos 2005; Canbolat et al. 2005; Parra-Montesinos et al. 2006; Parra-Montesinos and Chompreda 2007; Kesner and Billington 2005). While many of the investigations to date have been experimental in nature, there is demand for robust and expedient inelastic computational models that can be used to better understand member and system response. In order to predict the behavior of HPFRCC components under various loading conditions, a material model based on a plane stress, orthogonal, hybrid rotating/fixed crack approach, is developed in this study. The developed material model addresses the

[1] Chapter 2 is based on a submitted paper manuscript:
C.-C. Hung, S El-Tawil. "Hybrid rotating/fixed-crack model for high performance fiber reinforced cementitious composites." ACI Materials Journal. (submitted)

material's pronounced strain hardening behavior and takes into account its loading/unloading/reloading characteristics. The proposed 2-D macro-scale model for HPFRCC is based upon a model previously proposed by Han et al. (2003) (hereon designated HFB model). The proposed model differs from the HFB model on a number of fronts. In particular, the HFB model is based on a rotating crack model, whereas the current model is based on a hybrid rotating/fixed crack representation. There are also differences in constitutive relationships employed for both tension and compression and in the way shear response is computed, which make the proposed model able to accurately capture shear distortions at the structural level. The validity of the developed material model is shown through extensive comparisons between experimental data and numerical results for test specimens exhibiting varied structural responses. The comparison results indicate that the developed HPFRCC material model is capable of simulating the behavior of HPFRCC structures with reasonable accuracy.

2.2 CONSTITUTIVE MODEL

2.2.1 Crack modeling

The two methods commonly used to represent cracks in concrete models are the discrete crack approach and the smeared crack approach. In the former, the crack is modeled by generating finite elements at opposite sides of a crack to represent the discontinuity and by inserting specialized elements between opposing elements to represent local crack behavior, such as aggregate interlock and crack closing. The smeared crack approach, which was introduced by Rashid (1968), assumes that cracks exist in a uniform continuous sense. Rather than explicitly modeling a discontinuity, the presence of a crack

is modeled through local modification of material response. Although the discrete crack approach is able to describe physical cracks more realistically than the smeared crack model, its complex and intensive computational demands make it less popular, especially when it is applied to model two or more intersecting cracks. On the other hand, the smeared crack approach is able to simulate models containing well-distributed cracking with much less complexity. In addition, it also allows multiple cracks to occur simultaneously with different orientations at an integration point. Other advantages of the smeared crack approach can be found in Bolander and Wight (1989).

The smeared crack modeling approach has an extensive history. Some important developments can be found in the works by Balakrishnan and Murray (1988). and Cervenka (1985). Most existing smeared crack models have been developed for monotonic loading, however, some researchers have attempted to model concrete behavior under cyclic loading conditions (Han et al. 2003; Sittipunt and Wood 1995; Hassan 2004; Mo et al. 2008; Mansour and Hsu 2005). In this work, the smeared crack approach is adopted to model the influence of cracks on the cyclic response of HPFRCC material. Cracks are allowed to open and close and cracking orthogonal to an original crack is permitted to occur.

2.2.2 Crack orientation and growth

Two different approaches are commonly used to determine crack orientation after crack formation, namely fixed crack model and rotating crack model. In the former, the orientation of the crack plane is fixed after the crack forms. The stress-strain response at

the fixed crack plane and the plane perpendicular to it is then computed according to the loading history. Applications of the fixed crack model can be found in the studies by Sittipunt and Wood (1995), and Said et al. (2005). Vecchio and Collins (1982) suggested that the fixed crack approach may over constrain the problem, resulting in a higher predicted stiffness. In contrast, the rotating crack model assumes that the crack orientation continues to change with the principal direction after the crack initiates. This implies that damage in concrete is temporary, and is criticized by Bazant (1983) that it violates the basic concept of permanency of damage in concrete members.

HPFRCC materials undergo multiple fine cracks prior to crack localization (i.e. formation of a major crack, see Fig. 2.1a). In this work, the material is assumed to remain homogenous in a macro-sense during the multiple cracking stage until crack localization occurs. The effect of multiple cracking is, however, taken into account by recognizing that the material's tensile properties change once the elastic limit is exceeded, as described next. In essence, the material is assumed to be characterized by a rotating crack model in which crack directions can change orientation arbitrarily until crack localization occurs. After localization, the crack direction is fixed. The proposed HPFRCC model is therefore a hybrid rotating/fixed-crack model.

Crack initiation in the proposed model is defined using a strain criterion. A fixed crack is assumed to initiate when the principal strain at a certain integration point reaches the crack localization strain (ε_{tp}) of the HPFRCC material (Fig. 2.1a). Using this approach,

cracks are generated on the principal planes, and the directions and values of the principal strain vector are determined using Mohr's circle.

2.2.3 Stress-strain relationship – backbone curves

In the proposed crack model, the stress-strain relationships in both principal directions are assumed to behave uniaxially. In other words, the stress-strain relationship in one plane is assumed to be uncoupled from the other one. External confinement effects in HPFRCC are, however, assumed to follow the model by Mander et al. (1988) and are accounted for in the analysis by adjusting parameters in the unconfined model to reflect the additional strength and ductility due to confinement as was done in El-Tawil et al. (1999).

The monotonic uniaxial stress-strain relationship of HPFRCC materials is defined next based on experimental results in Liao et al. (2007), as shown in Fig. 2.1. The monotonic tensile behavior is assumed to consist of 3 segments (Fig. 2.1a). The 1st segment is the linear elastic portion. This is followed by strain hardening behavior (segment II) until crack localization occurs. After crack localization, the tensile behavior starts to linearly strain soften (segment III) until it is no longer able to support tensile stress. The failure envelope in tension is expressed as

$$\sigma = \begin{cases} \dfrac{\varepsilon}{\varepsilon_{tc}}\sigma_{tc} & for \quad 0 \le \varepsilon < \varepsilon_{tc} \\ \sigma_{tc} + \left(\sigma_{tp} - \sigma_{tc}\right)\left(\dfrac{\varepsilon - \varepsilon_{tc}}{\varepsilon_{tp} - \varepsilon_{tc}}\right) & for \quad \varepsilon_{tc} \le \varepsilon < \varepsilon_{tp} \\ \sigma_{tp}\left(1 - \dfrac{\varepsilon - \varepsilon_{tp}}{\varepsilon_{tu} - \varepsilon_{tp}}\right) & for \quad \varepsilon_{tp} \le \varepsilon < \varepsilon_{tu} \\ 0 & for \quad \varepsilon_{tu} \le \varepsilon \end{cases} \qquad (2.1)$$

The monotonic compressive behavior of HPFRCC materials is also assumed to be composed of 3 stages (segments I through III in Fig. 2.1b). In the first segment, the compressive stress starts from zero and progressively increases until reaching the compressive strength. Hognestad's parabolic function (Park and Paulay 1988) is used to simulate the hardening behavior in stage 1. The 1st stage is then followed by a linear softening portion (denoted segment II) until the residual strength is reached. In the 3rd stage, the stress is assumed to remain constant, i.e. a plateau stress is reached. The overall envelope for the monotonic compressive behavior can be expressed using the following equations.

$$\sigma = \begin{cases} f'_{cc}\left[2\left(\dfrac{\varepsilon}{\varepsilon_{cp}}\right) - \left(\dfrac{\varepsilon}{\varepsilon_{cp}}\right)^2\right] & for \quad \varepsilon_{cp} \le \varepsilon < 0 \\ \sigma_{cp}\left(1 - \dfrac{\varepsilon - \varepsilon_{cp}}{\varepsilon_{cu} - \varepsilon_{cp}}\right) & for \quad \varepsilon_{cu} \le \varepsilon < \varepsilon_{cp} \\ k_0 f'_{cc} & for \quad \varepsilon \le \varepsilon_{cu} \end{cases} \qquad (2.2)$$

2.2.4 Stress-strain relationship – cyclic models

Under random cyclic loading, the stress-strain functions in the HFB model (Han et al. 2003) are adopted. In tension, the stress can be calculated as (Han et al. 2003)

$$\sigma = \begin{cases} \dfrac{\varepsilon}{\varepsilon_{tc}}\sigma_{tc} & for \quad 0 \le \varepsilon_{t\max} < \varepsilon_{cp} \\ \max\left\{0, \sigma^{*}_{t\min}\left(\dfrac{\varepsilon-\varepsilon_{tul}}{\varepsilon^{*}_{t\max}-\varepsilon_{tul}}\right)^{\alpha t}\right\} & for \quad \varepsilon_{tc} \le \varepsilon_{t\max} < \varepsilon_{tp}, \dot{\varepsilon} < 0 \\ \min\left\{0, \sigma^{*}_{tul} + \left(\sigma_{t\max}-\sigma^{*}_{tul}\right)\left(\dfrac{\varepsilon-\varepsilon^{*}_{tul}}{\varepsilon^{*}_{t\max}-\varepsilon^{*}_{tul}}\right)\right\} & for \quad \varepsilon_{tc} \le \varepsilon_{t\max} < \varepsilon_{tp}, \dot{\varepsilon} \ge 0 \\ \max\left\{0, \sigma^{*}_{t\max}\left(\dfrac{\varepsilon-\varepsilon_{tul}}{\varepsilon^{*}_{t\max}-\varepsilon_{tul}}\right)\right\} & for \quad \varepsilon_{tp} \le \varepsilon_{t\max} < \varepsilon_{tu} \\ 0 & for \quad \varepsilon_{tu} \le \varepsilon_{t\max} \end{cases} \quad (2.3$$

where $\varepsilon^{*}_{t\max} = \varepsilon_{t\max}$ for initial unloading; $\varepsilon^{*}_{t\max} = \varepsilon_{tprl}$ for unloading followed by partial reloading; $\varepsilon^{*}_{tul} = \varepsilon_{tul} = \beta t \times \varepsilon_{t\max}$ for initial unloading; βt is a constant for tensile unloading curve; $\varepsilon^{*}_{tul} = \varepsilon_{tpul}$ for unloading followed by partial reloading.

When HPFRCC materials are under random cyclic displacements in compression, the stress state can be calculated as

$$\sigma = \begin{cases} f'_{cc}\left[2\left(\dfrac{\varepsilon}{\varepsilon_{cp}}\right)-\left(\dfrac{\varepsilon}{\varepsilon_{cp}}\right)^2\right] & \text{for} \quad \varepsilon_{cp} \le \varepsilon_{c\min} < 0 \\ \min\left\{0, \sigma^*_{c\min}\left(\dfrac{\varepsilon-\varepsilon_{cul}}{\varepsilon^*_{c\min}-\varepsilon_{cul}}\right)^{\alpha c}\right\} & \text{for} \quad \varepsilon_{cu} \le \varepsilon_{c\min} < \varepsilon_{cp},\ \dot{\varepsilon} > 0 \\ \min\left\{0, \sigma^*_{cul}+\left(\sigma_{c\min}-\sigma^*_{cul}\right)\left(\dfrac{\varepsilon-\varepsilon^*_{cul}}{\varepsilon_{c\min}-\varepsilon^*_{cul}}\right)\right\} & \text{for} \quad \varepsilon_{cu} \le \varepsilon_{c\min} < \varepsilon_{cp},\ \dot{\varepsilon} \le 0 \\ 0 & \text{for} \quad \varepsilon_{c\min} \le \varepsilon_{cu} \end{cases} \tag{2.4}$$

where $\varepsilon^*_{c\min} = \varepsilon_{c\min}$ for initial unloading conditions; $\varepsilon^*_{c\min} = \varepsilon_{cprl}$ for unloading conditions followed by partial reloading; $\varepsilon^*_{cul} = \varepsilon_{cul} = \beta c \times \varepsilon_{c\min}$ for initial unloading conditions; βc is a constant for compressive unloading curve; $\varepsilon^*_{cul} = \varepsilon_{cpul}$ for unloading followed by partial reloading. Fig. 2.2 shows an illustration of the stress values of a single element subjected to random cyclic displacements.

2.2.5 Shear stiffness reduction

Shear stiffness decreases after cracking occurs. Within the fixed crack context, some studies (Chung and Ahmad 1995; Hu and Schnobrich 1990) used a fixed reduction factor to reduce the shear modulus of concrete to differentiate between intact and cracked material. The fixed reduction factor was usually taken between 0 and 1. A more refined approach (Balakrishnan and Murray 1988; Cervenka 1985) assumes that the shear stiffness varies as a function of the strain perpendicular to the crack direction. More recently, Said et al. (2005) proposed a shear function to account for the shear stress-strain relationship for reinforced concrete.

To account for the reduced shear modulus of damaged HPFRCC material, a retention factor for the shear stiffness is introduced in the developed material model as is commonly done for regular concrete models (Balakrishnan and Murray 1988; Hassan 2004). The retention factor is assumed to vary as a function of the normal strain on the crack plane. As shown in Fig. 2.3, after crack localization, the retained shear stiffness is defined as $G_i = \mu G_{hpfrcc}$; where $G_{hpfrcc} = \dfrac{E_{hpfrcc}}{2(1+\nu)}$; i represents the direction, $i = 1$ for crack direction, and $i = 2$ for the direction perpendicular to crack direction. When the tensile strain exceeds the crack localization tensile strain, ε_{tp}, the shear stiffness is assumed to start decreasing linearly with an increase in the normal strain. The shear stiffness is assumed to reach a plateau, $G_{\min} = p_1 G_{hpfrcc}$, when the strain reaches $\varepsilon_{\min} = p_2 \varepsilon_{tp}$, where p_1 and p_2 are constants to define the minimum shear modulus and corresponding strain. The shear modulus in direction i can be expressed as

$$G_i = \begin{cases} G_{hpfrcc} & for \quad \varepsilon_{nn,i} < \varepsilon_{tp} \\ G_{hpfrcc}\left[\mu - (\mu - p_1)\left(\dfrac{\varepsilon_{nn,i} - \varepsilon_{tp}}{\varepsilon_{\min} - \varepsilon_{tp}}\right)\right] & for \quad \varepsilon_{tp} \le \varepsilon_{nn,i} < \varepsilon_{\min} \\ p_1 G_{hpfrcc} & for \quad \varepsilon_{nn,i} \ge \varepsilon_{\min} \end{cases} \qquad (2.5)$$

The total shear stiffness is then calculated using the local shear stiffnesses as

$$G_{cr} = 2.0\left[\frac{1}{G_1} + \frac{1}{G_2}\right]^{-1} \qquad (2.6)$$

For regular concrete, Hassan (2004) suggested that the value of μ depends on the type of the simulated structure, while Sittipunt and Wood (1995) proposed that the general values of μ, $\varepsilon_{\min}$ and p_1 are 0.2, $12.5\varepsilon_{tp}$, and 0.005, respectively, for regular concrete. In this work μ is assumed to be dependent on the type of fiber reinforcement used in the HPFRCC. Based on a calibration to the experimental data from a series of cyclic loading tests on HPFRCC structural members with various types and volume fractions of fibers (Chompreda 2005), μ is taken as 0.2 for HPFRCC with 1% to 2% by volume steel fibers and 0.1 for HPFRCC with 1% to 2% by volume polymeric fibers, while p_1 and p_2 are taken as 0.0001 and 12 respectively.

2.2.6 Mesh size dependency and material parameters

It is a well established fact that use of a softening material model in finite element analysis gives results which have first order mesh dependency i.e. the solution does not converge as the mesh becomes finer. This is because of a loss of hyperbolicity (in the dynamic case) or ellipticity (in the static case) of the underlying partial differential equations. Some of the existing techniques used to eliminate mesh sensitivity are non-local formulations, gradient based enhancements, visco-plastic formulations (Khandelwal and El-Tawil 2007), and the crack band approach (Bazant and Oh 1983; Cervenka and Papanikolaou 2008). A convenient way to solve the problem of mesh dependency is to make the material model dependent on element size, which is the approach adopted

herein. To achieve this objective, the ultimate tensile strain, ε_{tu}, for the numerical model is computed from a series of simulations of a dog-bone tensile test. The experimental value of the ultimate tensile strain is set as a target value, and a trial-and-error process is used to choose an appropriate numerical value for the ultimate tensile strain so that the computed load deflection response for the dog bone specimen matches the experimentally measured one for a given mesh density. The identified element size along with its corresponding ultimate tensile strain is then used in structural simulations. Mesh size dependency is only considered for elements in tension and not compression because tensile behavior is expected to dominate the response of structures considered in this research.

2.3 MATERIAL RESPONSE MODELING

The procedure for obtaining the current stress state at an integration point using the proposed approach is shown in Fig. 2.4. The current state of the global strain is first determined by adding the incremental strain to the strain state from the previous step. Then, depending upon whether the post cracking strain ε_{tp} has been previously reached, either the direction of the principal plane or the crack plane is calculated. After that, the corresponding local stresses are obtained using the current state of the local strain and the history variables. The orientations of the stress and strain in the principal/crack direction at each time instant are assumed to coincide. Therefore, the current state of global stresses can be computed using

$$\sigma_{xy}^{(j)} = T^T\left(\theta^{(j)}\right)\sigma_{12}^{(j)} \tag{2.7}$$

The proposed constitutive model for HPFRCC materials was implemented as a user-defined material model in LS-DYNA (Livermore Software Technology Corporation 2007). The subroutine for the user-defined model is compiled and linked to the LS-DYNA executable file to create a new executable file that can accommodate HPFRCC material behavior. At every time step, the user-defined model is fed strain and history information for each integration point and returns information on stresses, strains, and updated history variables. The solution is calculated in LS-DYNA using an explicit numerical integration scheme.

2.4 VALIDATION OF THE DEVELOPED HPFRCC MATERIAL MODEL

Three experimental tests are simulated using the developed numerical HPFRCC model to show that the model is able to accurately capture structural behavior. In these examples, which include a coupling beam, a dual cantilever beam, and a cantilever structural wall, steel reinforcement is modeled using nonlinear truss elements. Steel response is assumed to be elastic-plastic with kinematic hardening. The steel rebars used herein have a Young's modulus of 29000ksi (200 GPa), a hardening ratio of 1%, and yield strength specified in the studies in question. In addition, perfect bond is assumed between steel truss elements and the surrounding cementitious material.

2.4.1 Validation example 1 – coupling beam

A HPFRCC coupling beam with a 1.5% volume fraction of hooked fibers was tested under displacement reversals by Wight and Parra-Montesinos (Wight and Lequesne 2008). The dimensions of the coupling beam were $42in. \times 24in. \times 6in.$ ($106.7cm \times 61.0cm \times 15.2cm$) for $length \times height \times thickness$. A picture of the test set-up is shown in Fig. 2.5a, where cyclic displacements were imposed on the top concrete block, which was connected to the HPFRCC coupling beam. The bottom concrete block was fixed by bolting the subassemblage to the strong floor. To encourage the specimen to undergo pure shear deformation, vertical displacement of the top concrete block was guided by using 2 pinned steel struts connecting the top concrete block to the strong floor.

The reinforcement details for the specimen are shown in Fig. 2.5b. Longitudinal reinforcement was placed in two identical layers, and each layer consisted of 2 No. 3 and 2 No. 4 rebars. In addition, 4 No. 5 diagonal steel rebars were placed in the middle layer. No. 3 stirrups with a spacing of 2.75 in. (7.0 cm) were placed at the beam ends, and a spacing of 6 in. (15.2cm) was adopted for the middle portion of the beam. The yield strength for the steel rebars is 62 ksi (430 MPa).

The numerical model is shown in Fig. 2.6a, where the bottom concrete block is fixed and the vertical displacement of the top block is prevented to model the effect of the vertical struts constraining the motion of the specimen. A cyclic horizontal displacement was then imposed on the top concrete block. Material parameters used for the material models in this study are shown in Table 1 and were chosen based on data from material tests and previously discussed calibration data. The computed crack pattern is shown in Fig. 2.6b.

Fine cracking (in the hardening stage) are represented by thin line segments, while localized cracks with larger width are denoted by heavy lines, where heavier lines indicate larger crack width. Concrete crushing is denoted by solid circles.

At the end of the experimental test, a dense pattern of cracks accompanied by some concrete crushing at both ends of the coupling beam was observed as shown in Fig. 2.6c. Failure was, however, dominated by flexural response and flexural crack localization took place at the base and top of the specimen. The computed crack pattern and crush zones (Fig. 2.6b) match reasonably well the experimental configuration especially in the lower region of the specimen. However, the model over predicts the density of shear-related cracks in the middle portion of the specimen. A comparison between the computed and measured hysteretic responses is shown in Fig. 2.7. While the loading and unloading stiffnesses are well represented, the strength in the negative region is over predicted by 25% and in the positive region by 15%. Nevertheless, the degradation of strength with cycling is captured well, as is the pinching behavior.

2.4.2 Validation example 2 – dual cantilever beam

A dual cantilever beam (denoted as PE1.5-0.8-1.7 (Chompreda 2005; Parra-Montesinos and Chompreda 2007) with 1.5% polyethylene fibers, 0.8% transverse reinforcement, and 1.7% longitudinal reinforcement) was tested under reversed displacement. The specimen consisted of two beam components, which have dimensions of 4 in. (10.2 cm) by 10 in. (25.4 cm), connected by a middle block for the purpose of loading. Each cantilever beam had longitudinal reinforcement of 4 No. 5 steel rebars and was designed to evaluate the

interaction between transverse reinforcement and HPFRCC materials under large shear reversals. The yield strength for No. 2 rebars is 85 ksi (590 MPa) while that for all the other rebars is 62 ksi (430 MPa). Details of the beam dimensions and boundary conditions are shown in Fig. 2.8, while material properties are shown in Table 1. One side of the specimen was given slightly weaker material strength than the other (1% less) to initiate earlier inelastic response, thereby forcing deformation to preferentially localize there as was observed in the test.

The experimental result in Fig. 2.9a shows that the specimen exhibited a diagonal tension failure at a drift ratio of 10.2%, and no visible spalling of cover or buckling of longitudinal reinforcement was observed (Chompreda 2005; Parra-Montesinos and Chompreda 2007). The specimen response is successfully modeled by the numerical model as shown in Fig. 2.9b, where significant shear deformation and associated cracks in the plastic hinge region are observed. A comparison of the measured and computed hysteretic responses is shown in Fig. 2.10. It is clear that the load-drift hysteresis loops match each other closely and that stiffness, strength capacity, load/unloading/reloading slopes, and pinching behavior are all well represented. Fig. 2.11 shows the relationship between shear distortion and shear stress in the plastic hinge region. The shear distortion is computed from the numerical model in the same manner as Chompreda (2005), i.e. by computing diagonal deformations in the shear panel. Fig. 2.11 indicates that even though pinching is more pronounced in the computational model, the model still matches reasonably well the experimental data.

2.4.3 Validation example 3 – cantilever shear wall

The developed HPFRCC material model is further validated through a test of a slender structural wall (Parra-Montesinos et al. 2006). The structural wall has dimensions of $135.83in. \times 39.37in. \times 3.94in.$ $(345.0cm \times 100.0cm \times 10.0cm)$ for $height \times length \times thickness$ with details as shown in Fig. 2.12a. The structural wall was constructed using HPFRCC material with 1.5% volume fraction of steel twisted fibers in the lower portion with a height of 59.06 in. (150.0 cm) and regular concrete for the rest. Concrete behavior is simulated using the HPFRCC model adjusted so that the tensile strength is negligible. The material properties and reinforcement details of the structural wall are shown in Table 1 and Fig. 2.12a, respectively. Since the tensile properties of the HPFRCC in this experimental test were not documented (Parra-Montesinos et al. 2006), they are selected based a similar HPFRCC mix by Naaman and Reinhardt (2006). The yield strength for all the steel rebars is 62 ksi (430 MPa). The wall is fixed at its bottom end and is tested under reversed cyclic loading applied to its top.

As shown in Fig. 2.12b, the observed behavior of the structural wall was dominated by the flexural response (Parra-Montesinos et al. 2006). A dense array of flexural cracks accompanied by concrete crushing was observed in the lower section of the specimen as displayed in Fig. 2.12b. The crack pattern predicted by the developed numerical model is plotted in Fig. 2.12c, which indicates that the model reasonably captures the observed damage pattern. However, towards the end of the load regime, the model predicted minor crushing at the base of the wall, which was not observed experimentally. This may be attributed to the fact that the specimen suffered some local instability in plastic hinge

zone, which may have shielded it from excessive compressive demands that led to crushing in the model. The model could not represent this phenomenon because of its planar nature, i.e. it could not represent out-of-plane local buckling response. Nevertheless, good overall comparison is achieved for the load versus deflection (Fig. 2.13) and shear stress versus shear distortion responses (Fig. 2.14). Also, while the shear strain from the numerical model is about 15% less than that from the experimental result, the pinching behavior from the numerical simulation matches that from the experiment quite well.

2.5 SUMMARY

A numerical model for simulating the reversed, cyclic behavior of HPFRCC structural components is proposed in this study. The model, based upon a hybrid rotating/fixed-crack approach, allows orthogonal cracking and can be applied to plane stress problems. A retention factor that is a function of the crack normal strain is used to capture the effect of cracking on the shear response of HPFRCC materials. The developed model is validated through numerical simulations of various types of HPFRCC structures under reversed displacement, including a coupling beam with diagonal steel reinforcement, a dual steel-reinforced cantilever beam dominated by shear cracking, and a slender structural wall. Comparisons between numerical and experimental data show that the hysteretic response is generally reasonably well captured including load deflection behavior, shear stress versus shear distortion response, pinching response, loading and unloading stiffness and strength. Discrepancies between computed and measured results could be attributed to assumptions that were necessarily made due to lack of test data

characterizing the response of HPFRCC under cyclic loading. For example, the proposed model does not capture the effects of tension stiffening, tension softening, or bond slip. Size effects are also not considered. Such effects can be included in future versions of the proposed model once pertinent test data for HPFRCC under reversed cyclic loading becomes available.

2.6 **NOTATIONS**

i	=	direction
j	=	time step
μ	=	retention factor
T	=	strain transformation matrix
$\theta^{(j)}$	=	angle of the principal/crack plane
f'_{cc}	=	compressive strength of HPFRCC adjusted to account for confinement effects
k_0	=	ratio of residual compressive stress to f'_{cc}
αt	=	power for tensile unloading curve
αc	=	power for compressive unloading curve
βt	=	constant for tensile unloading curve
βc	=	constant for compressive unloading curve
p_1	=	constant associated with the minimum shear modulus
p_2	=	constant associated with $\varepsilon_{\min}$
v	=	Poisson's ratio
E_{hpfrcc}	=	Young's modulus
G_{cr}	=	shear stiffness
$G_{\min}$	=	minimum shear stiffness
G_{hpfrcc}	=	shear stiffness of the intact HPFRCC
G_i	=	shear stiffness in direction i
$\tau_{12}^{(j)}$	=	shear stress in local coordinate system
σ	=	stress
$\sigma_1^{(j)}$	=	1st principal stress
$\sigma_2^{(j)}$	=	2nd principal stress
$\sigma_{xy}^{(j)}$	=	stress vector in global coordinate system
$\sigma_{12}^{(j)}$	=	stress vector in local coordinate system
σ_{tc}	=	cracking stress
σ_{tp}	=	post-cracking stress
$\sigma^*_{t\min}$	=	minimum tensile stress for partial reloading
σ^*_{tul}	=	stress associated with ε^*_{tul}
$\sigma_{t\max}$	=	maximum experienced tensile stress
$\sigma^*_{t\max}$	=	maximum tensile stress for partial reloading
σ_{cp}	=	peak compressive stress
σ_{cu}	=	residual compressive stress

$\sigma^*_{c\min}$ = minimum compressive stress for partial reloading

$\sigma_{c\min}$ = minimum experienced compressive stress

σ^*_{cul} = stress associated with ε^*_{cul}

ε = strain

$\dot{\varepsilon}$ = strain rate

$\varepsilon_{\min}$ = strain associated with $G_{\min}$

$\varepsilon_{nn,i}$ = normal strain in direction i

$\varepsilon^{(j)}_{xy}$ = strain vector in global coordinate system

ε_{tc} = cracking strain

ε_{tp} = post-cracking strain

ε_{tu} = ultimate tensile strain

ε_{tul} = minimum tensile strain during unloading

ε^*_{tul} = minimum tensile strain for partial reloading

$\varepsilon_{t\max}$ = maximum experienced tensile strain

$\varepsilon^*_{t\max}$ = maximum tensile strain for partial reloading

ε_{tprl} = maximum tensile strain during partial reloading

$\varepsilon_{c\min}$ = minimum experienced compressive strain

$\varepsilon^*_{c\min}$ = minimum compressive strain for partial reloading

ε_{cul} = maximum compressive strain during unloading

ε^*_{cul} = maximum compressive strain for partial reloading

ε_{cp} = peak compressive strain corresponding to f'_{cc}

ε_{cu} = ultimate compressive strain

ε_{cpul} = maximum compressive strain during partial unloading

ε_{cprl} = maximum compressive strain during partial reloading

$\gamma^{(j)}_{xy}$ = shear strain in global coordinate system

$\Delta\varepsilon^{(j)}_{xy}$ = incremental strain vector in global coordinate system

$\Delta\varepsilon^{(j)}_{y}$ = incremental strain in y direction

$\Delta\gamma^{(j)}_{xy}$ = incremental shear strain in global coordinate system

Table 2.1 - Material parameters for the numerical models used in the validation examples.

Material parameters	**Coupling Beam**	**Dual Cantilever Beam**	**Cantilever Wall**	
			HPFRCC	**Concrete**
E_{hpfrcc}, **ksi (GPa)**	2666 (18.4)	3500 (24.1)	3000 (20.7)	3000(20.7)
ν	0.15	0.15	0.15	0.15
σ_{tc}, **ksi (MPa)**	0.40 (2.8)	0.35 (2.4)	0.3 (2.1)	0
ε_{tc}	0.00015	0.0001	0.0001	0
σ_{tp}, **ksi (MPa)**	0.50 (3.4)	0.45 (3.1)	0.4 (2.8)	0
ε_{tp}	0.002	0.002	0.005	0
ε_{tu}	0.17	0.12	0.15	0
σ_{cp}, **ksi (MPa)**	-5.5 (37.9)	-7.3 (50.3)	-10.4 (72.0)	-7(48.2)
ε_{cp}	-0.006	-0.0075	-0.005	-0.0035
σ_{cu}, **ksi (MPa)**	-2.0 (13.8)	-2.0 (13.8)	-2.0 (13.8)	-2(13.8)
ε_{cu}	-0.03	-0.03	-0.04	-0.025
μ	0.2	0.1	0.1	0.1
p_1	0.0001	0.0001	0.0001	0.0001
p_2	12	12	12	12
α_t	6	6	6	10
α_c	3	3	3	10
β_t	0.4	0.4	0.4	0.8
β_c	0.4	0.4	0.4	0.8

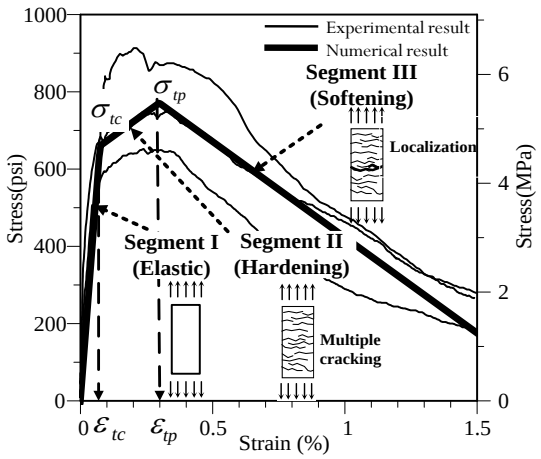

(a) tensile response

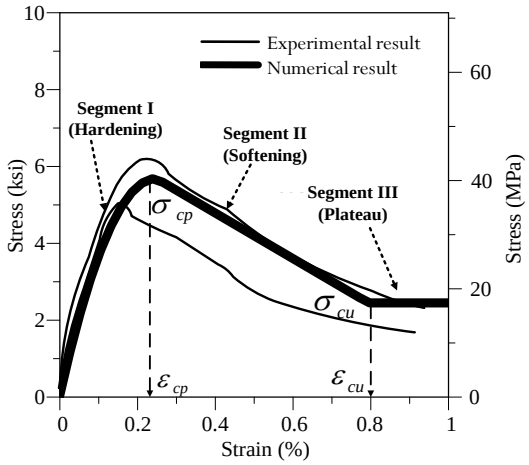

(b) compressive response

Fig. 2.1 - Typical monotonic stress-strain relationship of HPFRCC materials

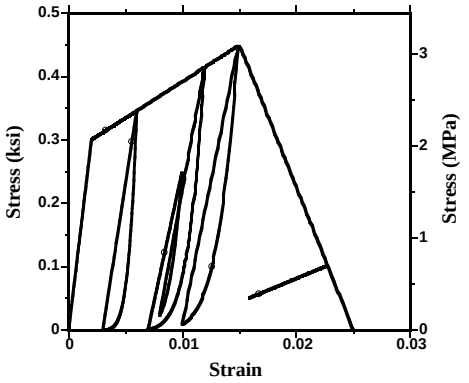

(a) reversed tensile response

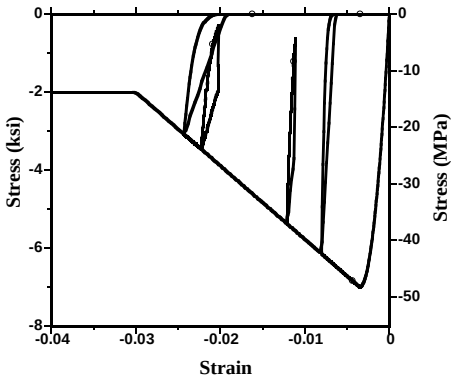

(b) reversed compressive response

Fig. 2.2 - Reversed stress-strain relationship of the developed model

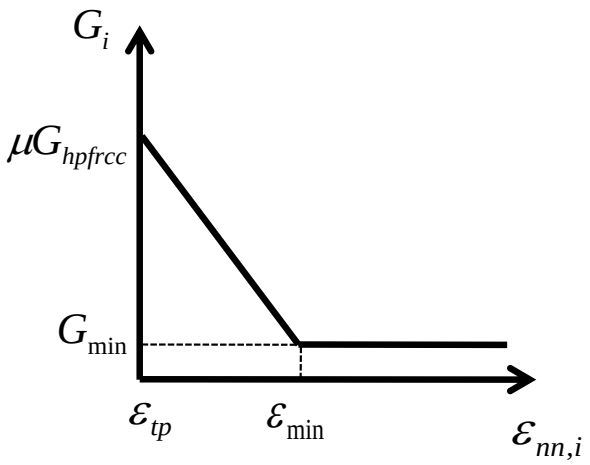

Fig. 2.3 - Relationship between normal strain and shear stiffness

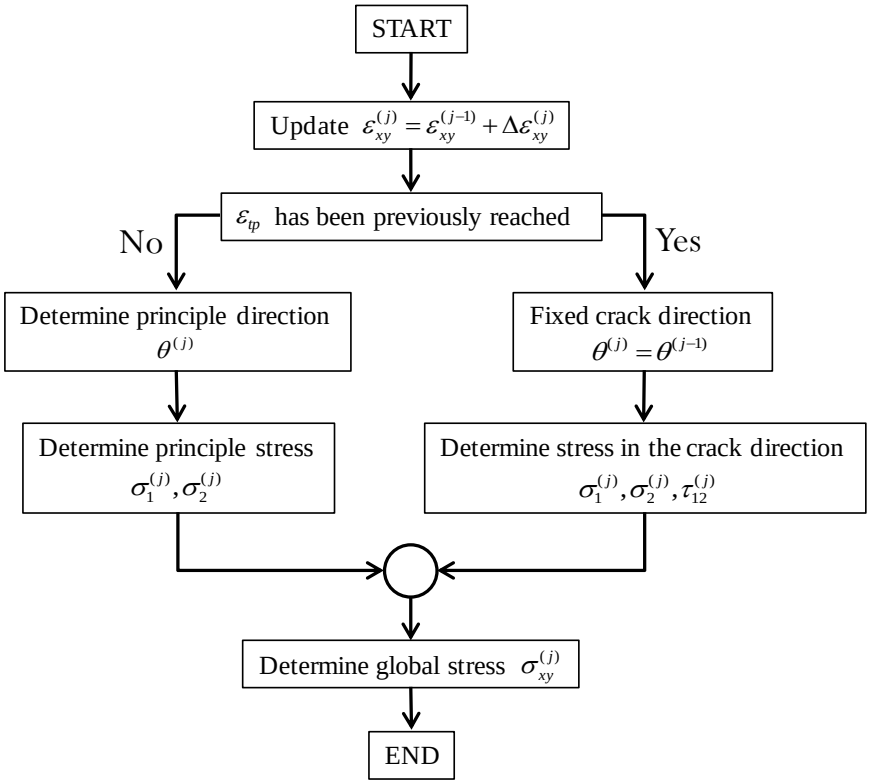

Fig. 2.4 - Procedure of implementing the algorithm for the HPFRCC material model

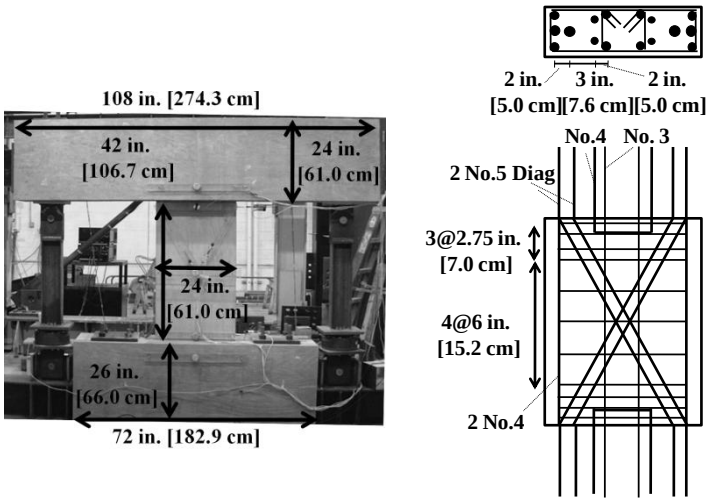

(a) experimental test setup (b) reinforcement details

Fig. 2.5 - Experimental test of a HPFRCC coupling beam

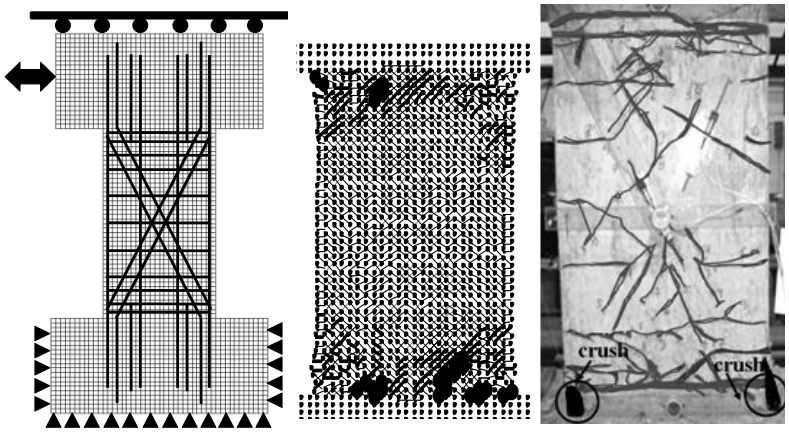

(a) coupling beam model (b) computed pattern (c) observed pattern

Fig. 2.6 - Computed versus observed damage patterns for coupling beam test

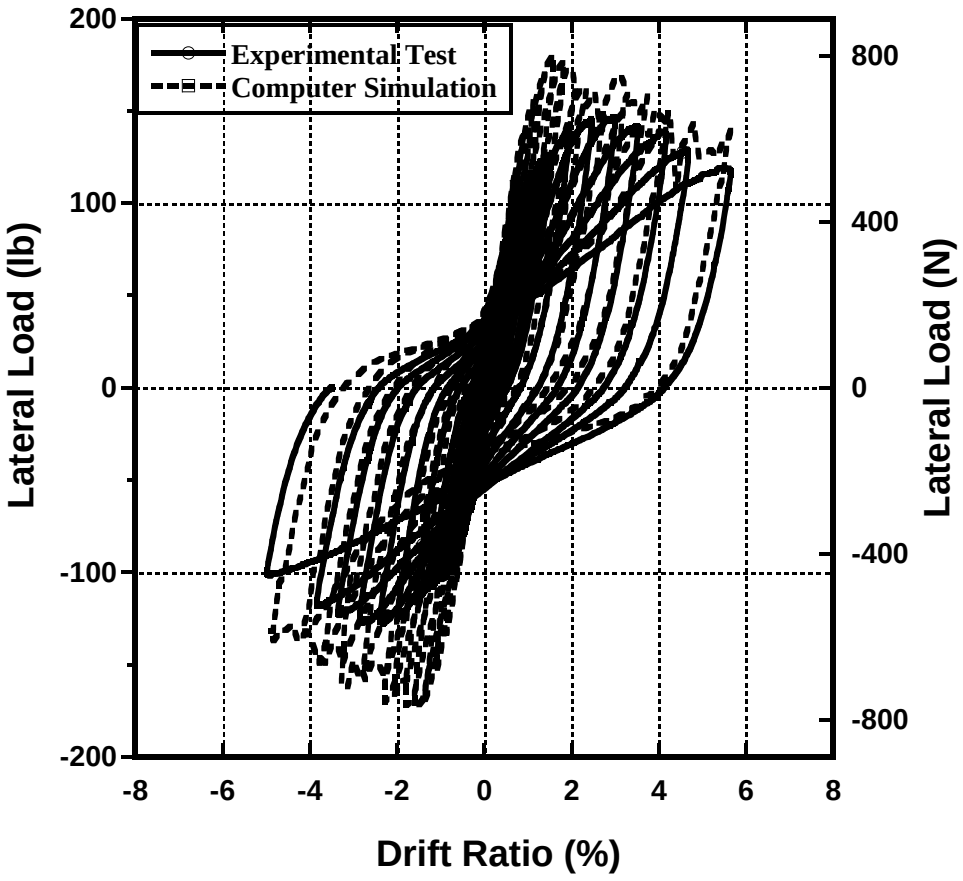

Fig. 2.7 - Comparison between computed and experimental hysteresis response for coupling beam test

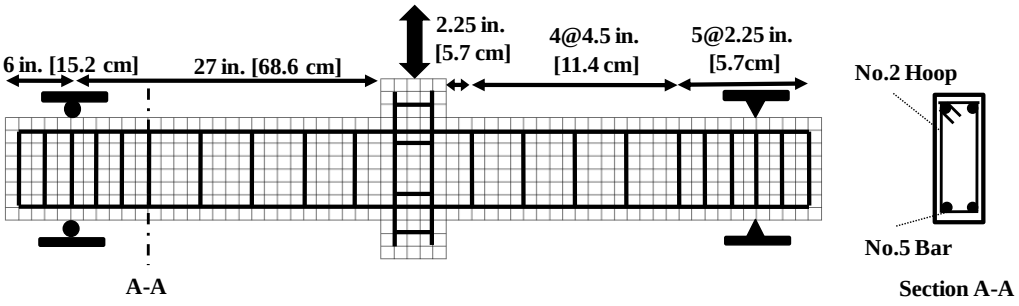

Fig. 2.8 - Experimental setup and reinforcement details of dual cantilever specimen

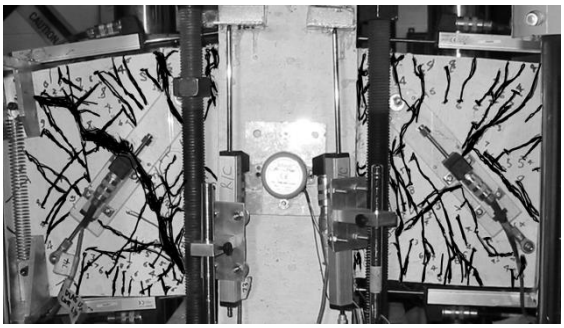

(a) experimental crack pattern

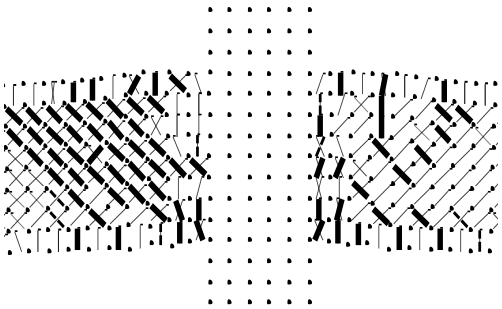

(b) computed crack distribution

Fig. 2.9 - Crack pattern of dual cantilever specimen

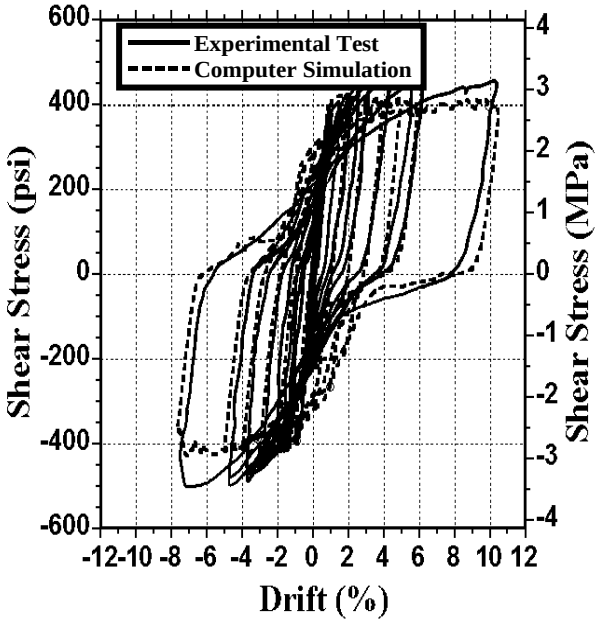

Fig. 2.10 - Shear stress versus drift relationship of dual cantilever specimen

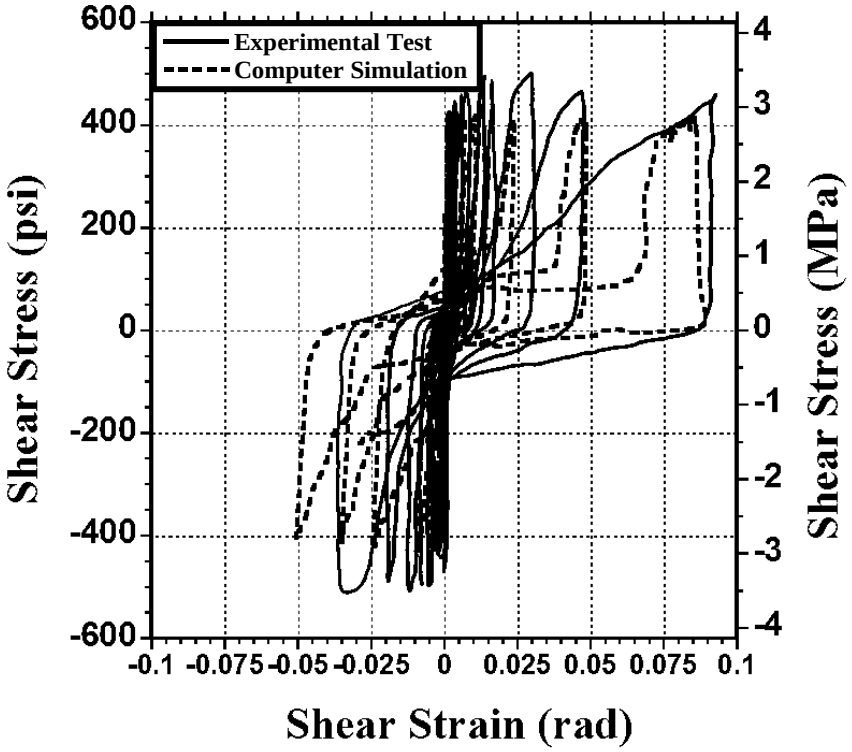

Fig. 2.11 - Shear stress versus shear strain relationship of dual cantilever specimen

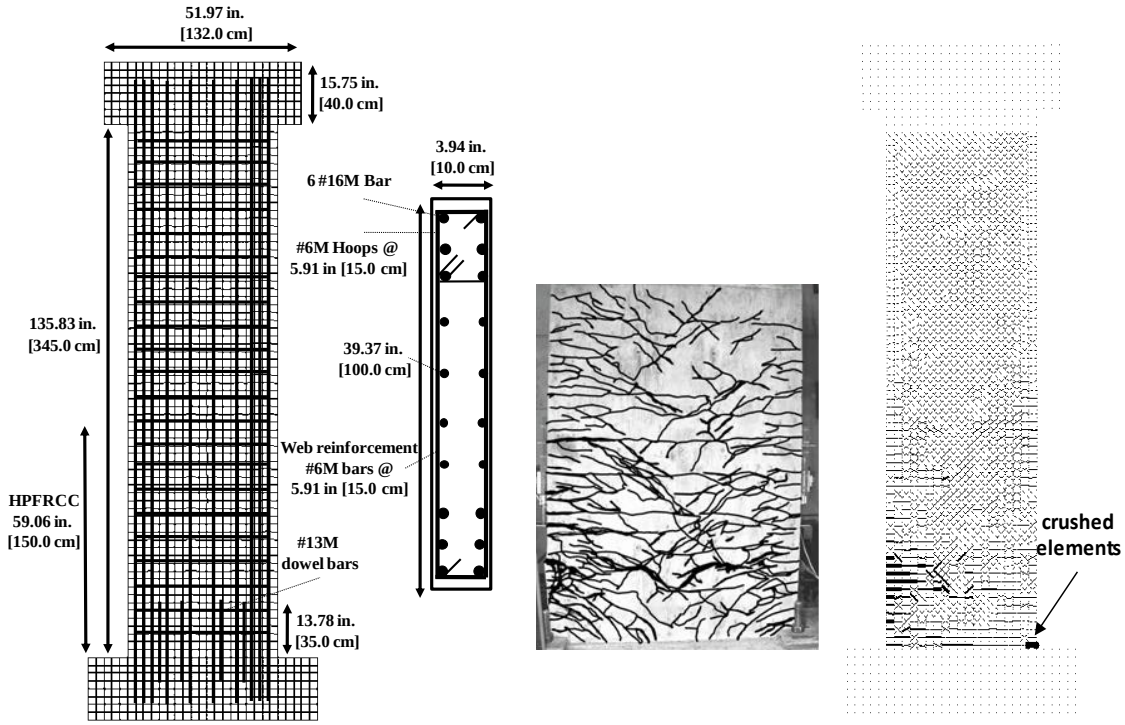

(a) numerical model and reinforcement details

(b) crack pattern in plastic hinge zone

(c) computed crack pattern

Fig. 2.12 - The cantilever wall validation study

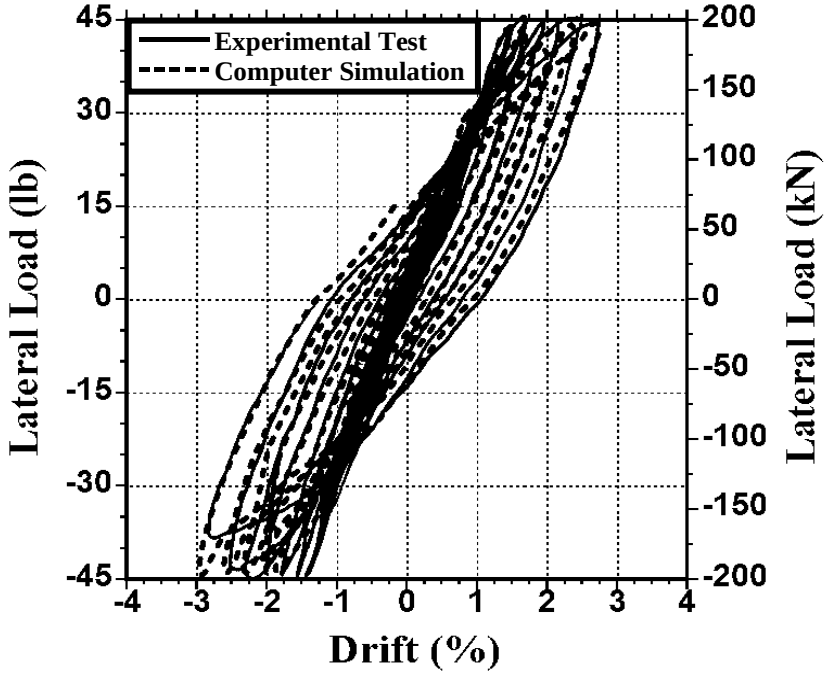

Fig. 2.13 - Lateral load versus drift relationship of cantilever wall specimen

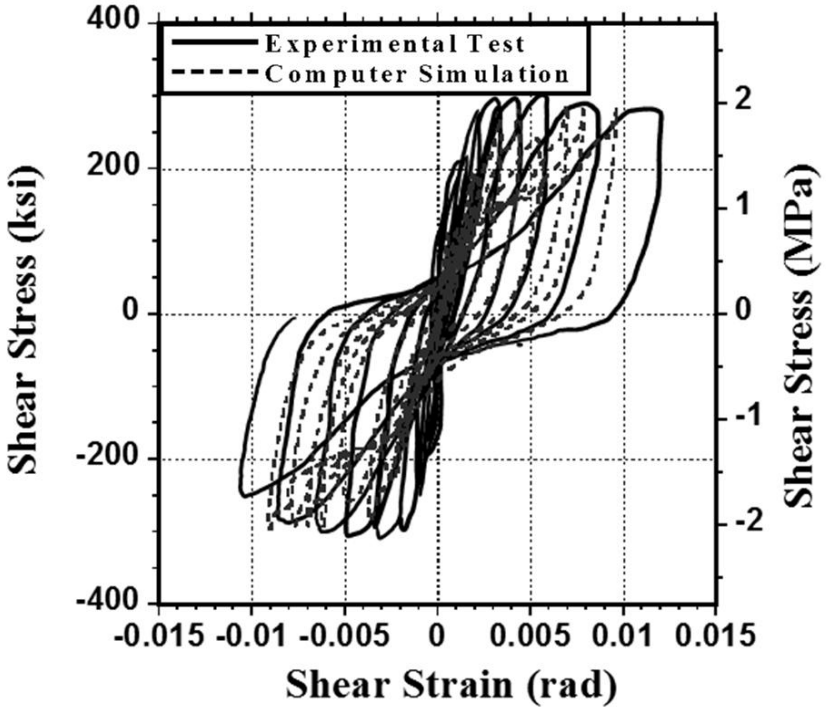

Fig. 2.14 - Shear stress versus shear strain relationship of cantilever wall specimen

2.7 REFERENCES

Balakrishnan, S., and Murray, D. W., "Concrete Constitutive Model for NLFE Analysis of Structures," Journal of Structural Engineering, ASCE, V. 114, No. 7, Jul. 1988, pp. 1449-1466.

Bazant, Z. P., "Comments of Orthogonal Models for Concrete and Geomaterials," Journal of the Engineering Mechanics, ASCE, V. 109, No. 3, Jun. 1983, pp. 849-865.

Bazant, Z. P. and Oh, B. H., "Crack Band Theory for Fracture of Concrete," Materials and Structures, RILEM, V. 16, No. 3, May 1983, pp. 155-177.

Bolander, J. E., and Wight, J. K., "Towards Realistic FE Model for Reinforced Concrete Shear Walls Dominant Buildings Subjected to Lateral Loadings," Report No. UMCE89-2, Department of Civil Engineering, the University of Michigan, Ann Arbor, Jan. 1989, pp. 192.

Canbolat, B. A., Parra-Montesinos G. J., and Wight J. K., "Experimental study on the seismic behavior of high-performance fiber reinforced cement composite coupling beams." ACI Structural Journal, V. 102, No. 1, *2005*, pp.159-166.

Cervenka, V., "Constitutive Model for Cracked Reinforced Concrete," ACI Journal, V. 82, No. 6, Nov.-Dec., 1985, pp.877-882.

Cervenka, J. and Papanikolaou, V. K., "Three Dimensional Combined Fracture-plastic Material Model for Concrete," International Journal of Plasticity, V. 24, No. 12, Dec. 2008, pp. 2192-2220.

Chompreda, P., "Deformation Capacity and Shear Strength of Fiber Reinforced Cement Composite Flexural Members Subjected to Displacement Reversals," Ph.D. Dissertation, Department of Civil and Environmental Engineering, the University of Michigan, Ann Arbor, 2005.

Chung, W. and Ahmad, S. H., "Analytical Model for Shear Critical Reinforced Concrete Members," ACI Structural Journal, V. 121, No. 6, Jun. 1995, pp.1023–1029.

El-Tawil, S. and Deierlein, G. G., "Strength and Ductility of Concrete Encased Composite Columns," Journal of Structural Engineering, ASCE, V. 125, No. 9,

Sep. 1999, pp. 1009–1019.

Han, T. S., Feenstra, P. H., and Billington, S. L.," Simulation of Highly Ductile Fiber-Reinforced Cement-Based Composite Components under Cyclic Loading," ACI Structural Journal, V. 100, No. 6, Nov.-Dec. 2003, pp. 749-757.

Hassan, M., "Inelastic Dynamic Behavior and Design of Hybrid Coupled Wall Systems," Ph.D. Dissertation, Department of Civil and Environmental Engineering, University of Central Florida Orlando, Florida, 2004.

Hu, H. T. and Schnobrich, W. C., "Nonlinear Analysis of Cracked Reinforced Concrete," ACI Structural Journal, V. 87, No. 2, 1990, pp. 199–207.

Khandelwal, K. and El-Tawil, S., "Collapse Behavior of Steel Special Moment Resisting Frame Connections," Journal of Structural Engineering, ASCE, V. 133, No. 5, May 2007, pp. 646-655.

Kesner KE**,** Billington SL. Investigation of infill panels made from engineered cementitious composites for seismic strengthening and retrofit. Journal of Structural Engineering (ASCE) 2005; 131(11):1712-1720.

Liao, W.-C., Chao, S.-H., Park, S.-Y., and Naaman, A. E., "Self-Consolidating High Performance Fiber Reinforced Concrete: SCHPFRC," High Performance Fiber Reinforced Cement Composites: HPFRCC-5, International Workshop, Mainz, Germany Jul. 2007.

Livermore Software Technology Corporation, "LS-DYNA® Keyword User's Manual," May 2007.

Mander, J. B., Priestley, M. J. N., and Park, R., "Theoretical Stress-Strain Model for Confined Concrete," Journal of Structural Engineering, ASCE, V. 114, No. 8, Aug. 1988, pp. 1804–1826.

Mansour, M., and Hsu, T. T. C., "Behavior of Reinforced Concrete Elements under Cyclic Shear II: Theoretical Model," Journal of Structural Engineering, ASCE, V. 131, No. 1, 2005, pp. 54-65.

Mo, Y. L., Zhong J., and Hsu, T. T. C., "Seismic Simulation of RC Wall-type

Structures," Engineering Structures, V. 30, No. 11, 2008, pp. 3167–3175.

Naaman AE, Reinhardt HW. Proposed classification of HPFRC composites based on their tensile response. Materials and Structures 2006; 39:547-555.

Park, R., and Paulay, T., "Reinforced Concrete Structures," John Wiley and Sons Publisher, New York, 1975, pp. 769.

Parra-Montesinos GJ. High-performance fiber reinforced cement composites: an alternative for seismic design of structures. ACI Structural Journal *2005;* 102(5):668-675.

Parra-Montesinos GJ, Canbolat BA, Jeyaraman G. Relaxation of confinement reinforcement requirements in structural walls through the use of fiber reinforced cement composites. 8th National Conference on Earthquake Engineering Apr. 2006, San Francisco, CA.

Parra-Montesinos, GJ, Chompreda P. Deformation capacity and shear strength of fiber reinforced cement composite flexural members subjected to displacement reversals. Journal of Structural Engineering *(*ASCE) 2007; 133(3):421-431.

Rashid, Y. R., "Analysis of Prestressed Concrete Vessels," Nuclear Engineering and Design, V. 7, No. 4, Apr. 1968, pp. 334-344.

Said, A., Elmorsi, M., and Nehdi, M., "Non-linear Model for Reinforced Concrete under Cyclic Loading," Magazine of Concrete Research, V. 57, No. 44, May 2005, pp. 211-224.

Sittipunt, C., and Wood, S. L., "Influence of Web Reinforcement on the Cyclic-Response of Structural Walls," ACI Structural Journal, V. 92, No. 6, 1995, pp-745-756.

Wight JK, Lequesne RD. Earthquake-resistant design of coupling beam elements incorporating high-performance fiber reinforced concrete. Proceedings of International Seminar on Seismic-Resistant Design of Reinforced Concrete Structures, Bogota, D.C., Columbia, May 15 2008; 97-108.

Vecchio, F. J., and Collins, M. P., "Response of Reinforced Concrete to Inplane Shear and Normal Stresses," Publication No. 82-03, Department of Civil Engineering, University of Toronto, Mar. 1982.

CHAPTER 3

SEISMIC BEHAVIOR OF A COUPLED-WALL SYSTEM WITH HPFRC MATERIALS IN CRITICAL REGIONS[1]

3.1 INTRODUCTION

Reinforced concrete coupled wall (RC-CW) systems are often used in mid- to high-rise structural systems in zones of high seismic risk to provide lateral resistance to earthquake loading. Coupled wall systems are comprised of two or more wall piers in series connected via reinforced concrete (RC) coupling beams. Under seismic action, the coupling beams must transfer adequate force between adjacent walls and, at the same time, are expected to contribute significantly to energy dissipation. These stringent requirements necessitate careful design and detailing of RC coupling beams to ensure that they have the necessary performance characteristics during a design seismic event.

Many studies of RC coupling beam performance have been conducted over the past four decades, e.g. Paulay (1971); Paulay and Binney (1974); Tassios et al. (1996); Galano and Vignoli (2000); Kwan and Zhao (2001); and Hindi and Hassan (2004). The common research theme in these studies was to investigate the effect of various reinforcement

[1] Chapter 3 is based on a paper which is in preparation.
C.C. Hung, S. El-Tawil. Seismic Performance of Midrise High Performance Fiber Reinforced Concrete Coupled Wall Systems. *Journal of Structural Engineering (in preparation).*

amounts and configurations on the cyclic response of RC coupling beams, with the aim of ensuring stable hysteretic response. The results of these studies have culminated in the current commonly used design provisions in the ACI (2008) code and other codes worldwide, which entail diagonally reinforced coupling beams with sufficient steel confinement. Beams detailed in such a manner have been shown to be capable of providing adequate strength, stiffness, and energy dissipation capacity. They are able to dissipate a large amount of energy prior to the onset of significant inelastic response of the coupled wall piers, which is the preferred energy dissipation mechanism for RC-CW systems (Harries and Mcneice 2006).

The stringent detailing requirements for coupling beams usually results in a dense reinforcement configuration, which complicates erection of RC coupled wall systems, lengthening construction time and increasing cost. Furthermore, as a result of the way a coupled wall system deforms, most of the inelastic behavior in wall piers takes place in the plastic hinge zone at the base of the piers. Since the deformation demands are expected to be high in the plastic hinge zones, such regions are usually heavily confined to assure good response under reversed cyclic behavior. In other words, RC-CW systems require extensive detailing to ensure that they can provide acceptable seismic performance.

The detailing requirements for RC-CW systems stem primarily from the brittle nature of concrete, especially when subjected to cyclic loading. As indicated in Chapter 1, an alternative building material that has the potential for alleviating many of the stringent

detailing requirements for RC-CW systems is high performance fiber reinforced concrete (HPFRC). The material's tensile strain hardening behavior after first cracking coupled with its self-confined compressive response implies that a reduction in the level of detailing can be achieved without compromising performance.

Experimental studies on individual coupling beams have indicated that using HPFRC to replace traditional concrete material can allow relaxation of reinforcing details while still providing satisfactory performance, i.e. strength and deformation capacity (Canbolat et al. 2005). Furthermore, Parra-Montesinos et al. (2005) showed that using HPFRC materials in slender walls can lead to good performance under cyclic displacement in spite of significantly reduced confinement detailing. To investigate the implications of these experimental observations at the system level, numerical studies are conducted to compare the performance of a traditional RC 18-story coupled wall systems with that of another similar system in which the coupling beams and plastic hinge regions are HPFRC instead of RC, hereafter denoted H-CW system. The study presented herein is conducted using computational simulation models that account for the major sources of nonlinear response in HPFRC walls including regular concrete and HPFRC cracking and crushing behavior as well as rebar yielding. The system performance under various hazard levels is investigated and the system response is evaluated through various parameters including inter-story drift, rotation and distortion of critical structural parts.

While numerical studies of RC-CW systems subjected to seismic loading abound in the literature, the majority of these were conducted using structural-scale models in which

member response is modeled using linear or non-linear beam-column elements. Readers are referred to El-Tawil et al. (2010) for a succinct summary of the results of these studies. This chapter goes beyond the many published studies on coupled wall systems that employed macro-models in that it represents system response using detailed finite element models. Moreover, the work differs from all existing studies on coupled wall systems in that it focuses on modeling and investigating the behavior of wall systems with HPFRC components.

3.2 SYSTEM DESIGN

The theme system considered in this chapter consists of a 94.0 ft [28.8 m] by 78.5 ft [24.0 m] (in plan) steel moment resisting frame surrounding a 47 ft [14.3 m] by 31.5 ft [9.6 m] (in plan) core wall system. The plan view of the prototype structure is given in Fig. 3.1. The total height of the structure is 219 ft [67.5 m]. The first floor's height is 15 ft [4.6 m] and typical floors are 12 ft [3.7 m] high. The thickness of the wall is 20" [500 mm] and the total structure's weight is 20,831 kips [9449 tons]. Two different prototype wall systems are designed for comparison purposes. The first is a traditional RC system. The second prototype has HPFRC coupling beams. In addition, HPFRC is used in the first four floors of the wall piers.

The prototype structure is assumed to be an office structure in Los Angeles, and is categorized as Seismic Use Group I. The spectral response accelerations for short periods and at 1 second, Ss and S1, are then determined, respectively. Assuming site class D, the map accelerations are adjusted to the design accelerations, S_{DS} and S_{D1}. The building is

thus classified as Seismic Design Category E. The structure is defined as a dual system due to the structure's frame-wall system, and the design coefficients and factors are chosen from (FEMA-450 2003) accordingly.

Seismic design loads are calculated in accordance with the equivalent lateral force analysis in (FEMA-450 2003). Due to the symmetric nature of the theme system, the numerical analysis is simplified by modeling only half of the structure. To account for cracking and loss of stiffness due to expected cyclic behavior of the concrete walls, the effective flexural and axial stiffness of wall piers are taken as $0.70EI_g$ and $1.00EA_g$ (ACI 2008) for the compression wall, and $0.35EI_g$ and $0.35EA_g$ for the tension wall, respectively (El-Tawil et al. 2010).

A target coupling ratio of 45% (computed when the system has formed a full plastic mechanism as discussed in El-Tawil et al. 2010) is chosen for both RC-CW and H-CW systems. The coupling ratio is the proportion of the moment generated by the coupling action to the system overturning moment (El-Tawil et al. 2010). To simplify the coupling beam design, the generally reasonable assumption that the theme system does not have significant higher mode effects is made. In addition, it is assumed that the plastic deformation mechanism of the wall system is that plastic hinges form at the base of the shear walls and at the ends of all coupling beams. Analysis results presented in Hassan and El-Tawil (2004) suggest that these assumptions are fair for the set of 18-story buildings that they considered. The total coupling beam forces are uniformly distributed to each beam, and all coupling beams are therefore designed to have the same cross

section. Following (Hassan and El-Tawil 2004; El-Tawil et al. 2010), the beam shear demand is

$$V_{beam} = (CR \times OTM)/(N \times S) \tag{3.1}$$

where *CR* is the coupling ratio, in this case 0.45; *OTM* is the overturning moment; *N* is the number of stories; *S* is the distance between wall centroids. An elastic frame model is then numerically constructed to determine wall forces and drifts. In the model, beam-column elements, which are located at the gross section centroid of each wall, are used to represent walls. Coupling beams are represented using rigid body elements with released restraints at both ends and applied coupling beam shear force, V_{beam}, and end moment, M_{beam} at the wall piers. The applied end moment is calculated using

$$M_{beam} = (L_{beam} \times V_{beam})/2 \tag{3.2}$$

where L_{beam} is the clear span length of the coupling beam.

The concrete and steel yield strengths are 7 ksi [48 MPa] and 60 ksi [414 MPa], respectively. The HPRCC material properties used herein are based on Naaman and Reinhardt (2006)'s work in which a 2% volume fraction of Torex fibers was used to make HPFRC. The HPFRC crack-localization strain is 1%, the tensile strength is 0.75 ksi [5.1MPa], and the compressive strength is 7 ksi [48MPa].

In contrast to the method in the ACI code (2008) wherein flexural capacity is provided solely by the diagonal cages, the moment capacity of the RC coupling beams is provided by both diagonal reinforcement cages and flexural reinforcement rebars. The shear is provided by diagonal and transverse reinforcement to fully exploit the capacity of the steel reinforcement. The diagonal reinforcement cage consists of 4 #7 bars and #4 hoops spaced at 5" [127 mm]. The resulting coupling beam has a thickness of 20" [508 mm], depth of 28" [711 mm], and aspect ratio of 2.1. Reinforcement details are shown in Fig. 3.2.

The reinforcement detailing proposed by Canbolat et al. (2005) is used for the HPFRC coupling beam. Instead of the diagonal cages shown in Fig. 3.2, the HPFRC coupling beam is reinforced via 2#10 diagonal steel bars as shown in Fig. 3.3. Based on their test results, Canbolat et al. (2005) also showed that HPFRC material can provide a shear strength 40% larger than the maximum shear stress allowed in the ACI 318 Code (2008) for very short coupling beams. To account for the enhanced shear resistance of HPFRC over RC, the shear reinforcement is reduced by about 30% for the HPFRC coupling beam as shown in Fig. 3.3. However, the dimension and amount of longitudinal reinforcement for the HPFRC beam are kept the same as those for the RC beam.

The details of the RC-CW piers are designed based on (ACI 318 2008) and are shown in Fig. 3.4 and Table 3.1; where the thickness of the wall, t_w, is 20" [508 mm], and L_{be} is the length of boundary zone. Since no design provisions exist for the H-CW system, available research results coupled with engineering judgment were employed to detail the

piers. Using moment versus curvature analysis to meet the design moment demand, the flexural reinforcement scheme outlined in Table 3.1 and shown in Fig. 3.4 is selected for the H-CW piers. It is notable that the amount of primary flexural reinforcement in the first 4 floors of the H-CW piers is about 20% less than that in the corresponding areas in the RC-CW piers, which reflects the superior strength and ductility of the HPFRC material. Initial trials using the reinforcement scheme in the RC-CW resulted in the plastic hinges being shifted to the 5^{th} floor when the H-CW system was subjected to strong seismic shaking, which resulted in unacceptable system performance. In recognition of the beneficial effects of HPFRC and in accord with Parra-Montesinos (2005), the confinement reinforcement in the first 4 floors of H-CW is reduced by 50% from that used in the corresponding zones in the RC-CW piers.

3.3 FINITE ELEMENT MODELING

The developed hybrid rotating/fixed crack model from Chapter 2, which is suitable for plane stress elements for simulating HPFRC and reinforced concrete materials, is used to model the prototype structures. Although the model is primarily based on uniaxial material response in the principal directions, the effect of confinement detailing is addressed in an indirect manner. Confinement effects in both RC and HPFRC components are assumed to follow the model by Mander et al. (1988) and are accounted for in the analysis by adjusting parameters in the unconfined model to reflect the additional strength and ductility due to confinement as was done in El-Tawil and Deierlein (1999). As presented in Chapter 2, the developed model was shown to be accurate and robust through extensive comparisons between experimental and

computational results of hysteresis behavior and crack patterns for several types of structural components, including a coupling beam, shear wall, and double cantilever beam (Hung and El-Tawil 2009). In general, the model was capable of reasonably predicting the strength capacity, loading/unloading/reloading slopes, pinching behavior, and shear deformation characteristics of the various HPFRC structural components considered. Fig. 3.5 shows the backbone curves for compression and tension response simulated by the model.

The theme structure models were run on LS-DYNA (Livermore Software Technology Corporation 2007), an explicit finite element software package. Steel reinforcement is modeled using nonlinear truss elements and steel material is modeled using kinematic hardening plasticity with elastic-plastic behavior. The steel rebars used herein have a Young's modulus of 29000 ksi [200 GPa], a yield strength of 60 ksi [414 MPa], and a hardening ratio of 1%. Perfect bond is assumed between the rebar and concrete material. Before seismic excitation is imposed, gravity loads are first applied to the prototype structures. In addition, a 5% damping ratio is introduced in the analysis.

Although the model described above has shown satisfactory performance in predicting the behavior of HPFRC and reinforced concrete structural components considered in the validation studies, it does have a number of limitations, as noted in Hung and El-Tawil (2009). In particular, the model cannot account for sliding shear, rebar slip, splitting, tension stiffening and tension softening in both concrete and HPFRC. In addition, it cannot address out of plane stability, e.g. local buckling of cracked wall parts, rebar buckling and the effects of low-cycle fatigue fracture on bar response. The first set of

limitations stem primarily from a lack of test results by which to calibrate the developed HPFRC model, while the stability issues noted in the second set stems from the planar nature of the model. Nevertheless, as long as these limitations are kept in mind, the model can still yield valuable insight into structural response, especially at the system level, as shown in the successful validation studies presented in Hung and El-Tawil (2009).

3.4 ANALYSIS RESULTS

Performance of both prototype systems is evaluated using nonlinear dynamic time history analysis. Two groups of simulated time history ground motion records, developed by the SAC (Acronym for *Structural Engineers Association of California* 'SEAOC', *Applied Technology Council* 'ATC' and *California University for Research* in Earthquake Engineering 'CUREe') steel project, representing different seismic hazard levels, are used herein. Both groups contain seven ground motion records in each with probability of exceedance of 10% in 50 years (10/50), and 2% in 50 years (2/50), respectively. To reduce the computational effort, only the strong motion duration of the ground motion record is adopted for seismic excitation. The strong motion duration is defined as the time segment in which 90 percent of the seismic energy is delivered (Hassan and El-Tawil 2004).

The systems are evaluated using various parameters (FEMA-356 2000), including story drift, wall deflection profile, wall rotation (Fig. 3.6), and coupling beam chord rotation (Fig. 3.7). The average value of each response parameter during the seven ground motion histories is used as a representative value of the system's performance (FEMA-356

2000). System performance is then evaluated by comparing the demand computed form the numerical models to the performance criteria (Table 3.2) specified in FEMA-356 (2000).

Details of the maximum component responses for each earthquake are plotted in Figs. 3.8 through 3.14. Performance parameters for 10/50 earthquakes are plotted in Figs. 3.8 through 3.10. The story drift of both systems under each prescribed motion is shown in Fig. 3.8 where the average curves indicate that the prototype HPFRC structure and RC structure have similar profiles of story drift despite the reduced steel reinforcement and simplified reinforcing detailing in the HPFRC structure. Furthermore, the average maximum drift that occurs in both systems is around 0.008, which is below the acceptance criterion specified in (FEMA- 356 2000), implying that both prototype systems can perform adequately during a 10/50 event.

Figs. 3.9 and 3.10 show the rotation demands of the beams and wall piers during the 10/50 events, respectively. Clearly, both systems have similar rotational demands in the beams and wall piers along the building height. Again, the response parameters indicate that the prototype H-CW system is able to achieve similar overall response as the RC-CW system at the 10/50 hazard level. In particular, the maximum plastic hinge rotation and coupling beam rotations are around 0.002 rad and 0.0073 rad, respectively, which are well below the acceptance criteria in (FEMA-356 2000).

System responses during the 2/50 earthquakes are plotted in Figs. 3.11 through 3.13. The

maximum story drifts of the systems for each prescribed excitation are displayed in Fig. 3.11. It can be seen that the average value of story drifts from both systems are below 2%, meeting the acceptance criterion in (FEMA-356 2000). Coupling beam rotations during the 2/50 events are plotted in Fig. 3.12. In general both systems have similar coupling beam rotation demands in spite of the reduced reinforcement amount and detailing in the HPFRC coupling beams. The maximum coupling beam rotation is around 0.016 rad for both systems, which is below the acceptance criterion (0.03 rad) in (FEMA-356 2000). Fig. 3.13 shows the wall deflection response of the two systems. Again, it can be seen that both systems have similar wall deflection profiles despite key differences in the reinforcing steel quantities and detailing.

Wall rotations during the 2/50 events are plotted in Fig. 3.14. It is obvious that plastic hinges take place at the wall base for both systems when the peak response is reached. Nevertheless, unlike the similar wall rotation response observed during the 10/50 events, the wall rotation at H-CW wall base (0.0048 rad) is substantially less than that at the RC-CW wall base (0.0074 rad), i.e. reduced by 35%, during the 2/50 events. To highlight the effect of HPFRC, the maximum wall rotations of both systems during the most demanding earthquake are plotted in Fig. 3.15, which focuses only on the bottom floors of the structures. The Fig. 3.15 shows the wall rotations corresponding to various values of story drift, i.e. 1%, 2.5%, and 3.3%. It can be seen that the effect of HPFRC becomes more prominent as the demand grows. For example, at 1% drift, both systems experience the same rotational demand at the first floor. However, the rotation of the first floor of H-CW drops with respect to the corresponding value for RC-CW as the drift increases.

Particularly, when the drift increases to 2.5%, the plastic hinge rotation of the H-CW is 25% less than that of the RC-CW. Further, when the maximum drift of 3.3% is reached, the H-CW's rotation is 35% less than the RC-CW's. The lower rotational demand in the first floor of H-CW is accompanied by increased rotational demands in the 2^{nd}, 3^{rd} and even 4^{th} floors compared to the RC-CW system. In other words, the HPFRC causes the size of the plastic hinge zone to increase significantly compared to the RC system, but with a lower peak rotational demand due to a more even distribution of curvature along the plastic hinge zone. This suggests that despite of the reduced reinforcement amount used, HPFRC walls possess a better energy dissipation capacity and will likely suffer less permanent damage after severe seismic events.

Fig. 3.12 suggests that the coupling beams between the 8^{th} and 18^{th} floor are likely subjected to more damage compared to other coupling beams. The crack localization patterns of the coupling beam at the 12^{th} floor at various stages (corresponding to various beam rotations) during the most demanding earthquake are plotted in Fig. 3.16. In the figure, the thickness of the lines indicating crack localizations is proportional to crack width, while black dots represent concrete crushing. It can be seen that the flexural and shear cracking damage in the RC coupling beams are more severe and widespread than that in HPFRC coupling beams. Moreover, at the end of the ground excitation, residual crack localizations in HPFRC coupling beams are much less than in their RC counterparts. This is taken to imply that HPFRC coupling beams could require significantly less repair than RC coupling beams after a strong seismic event.

The crack localization patterns of the first five floors levels, corresponding to the time when the maximum system response takes place, are plotted in Fig. 3.17. It can be seen that a combination of flexural and shear cracks occurs in both systems. However, it also indicates that the RC wall system is subjected to more severe flexural cracks at the wall base whereas a more uniformly distributed cracking is observed in the HPFRC system. Fig. 3.18 shows the residual crack localization patterns of both systems after the most demanding motion. It shows a more severe permanent flexural and shear cracking damage in RC-CW (Fig. 3.18b) versus H-CW (Fig. 3.18a).

3.5 SUMMARY

The effectiveness of using HPFRC material to replace conventional RC in the critical portions of an 18-story coupled wall system was discussed. Two coupled wall systems were considered: the first was a traditional RC design, while the second was a modified design in which HPFRC is used in the plastic hinge regions of the wall piers and in the coupling beams. The latter system was designed with less steel and relaxed detailing than the former in recognition of the beneficial effects of HPFRC; in particular, 30% reduction in the shear reinforcement of the coupling beams, 20% reduction in the flexural reinforcement in the flange and boundary zone of the wall piers, and 50% reduction in confinement reinforcement in the boundary zone. The responses of both systems subjected to seismic events with different hazard levels were compared. The hazard levels considered herein included a level of 10% probability and a level of 2% probability of exceedance in 50 years. Comparisons of seismic response were made using story drift, wall rotation, and rotation of the coupling beams. For the 10/50 earthquakes, the

performance parameters studied suggested that both systems delivered similar performance in spite of the reduced reinforcement quantity and relaxed detailing in the HPFRC system compared to the RC system. The advantage of using HPFRC for the coupled walls became more evident when 2/50 earthquakes were considered. First of all, the HPFRC system was capable of delivering collapse prevention performance despite the reduced reinforcement amount and simplified reinforcing detailing. Further, the unique pseudo strain-hardening behavior of HPFRC materials effectively reduced the maximum wall rotation at the wall base through an enhanced energy dissipation pattern. The advantage of using HPFRC for the coupled walls was also evident in the crack patterns from the coupling beams and wall piers of both systems which suggested that at the end of a seismic event, the HPFRC system remained significantly more intact than the RC system, likely requiring less repair.

Table 3.1 - Reinforcement details of HPFRC and RC walls

			Flange		Web		Boundary Zone	
System	**Floors**	**L_{be}**	**Horiz.**	**Vert.**	**Horiz.**	**Vert.**	**Horiz.**	**Vert.**
HPFRCC Walls	**17-18**	0	#4@12”	#4@12”	#4@12”	#5@8”	-	-
	15-16	24”	#4@12”	#4@12”	#4@12”	#5@8”	#4@12”	12#7
	13-14	32”	#4@8”	#5@12”	#4@8”	#5@8”	#4@8”	16#9
	11-12	32”	#4@8”	#6@12”	#4@8”	#5@8”	#4@8”	16#9
	9-10	40”	#5@8”	#6@8”	#5@8”	#6@8”	#4@8”	20#9
	7-8	40”	#5@8”	#7@8”	#5@8”	#6@8”	#5@8”	20#10
	5-6	48”	#5@8”	#8@8”	#5@8”	#7@8”	#5@8”	24#10
	3-4	48”	#6@8”	#7@8”	#6@8”	#7@8”	#5@8”	24#10
	1-2	48”	#6@8”	#7@8”	#6@8”	#7@8”	#5@8”	24#10
RC Walls	**17-18**	0	#4@12”	#4@12”	#4@12”	#5@8”	-	-
	15-16	24”	#4@12”	#4@12”	#4@12”	#5@8”	#4@12”	12#7
	13-14	32”	#4@8”	#5@12”	#4@8”	#5@8”	#4@8”	16#9
	11-12	32”	#4@8”	#6@12”	#4@8”	#5@8”	#4@8”	16#9
	9-10	40”	#5@8”	#6@8”	#5@8”	#6@8”	#4@8”	20#9
	7-8	40”	#5@8”	#7@8”	#5@8”	#6@8”	#5@8”	20#10
	5-6	48”	#5@8”	#8@8”	#5@8”	#7@8”	#5@8”	24#10
	3-4	48”	#6@8”	#8@8”	#6@8”	#7@8”	#5@4”	24#11
	1-2	48”	#6@8”	#8@8”	#6@8”	#7@8”	#5@4”	24#11

Table 3.2 - Acceptance criteria for the selected performance level (FEMA-356 2000)

	Acceptance criteria	
	Collapse Performance	**Life Safety**
Shear wall story drift (rad)	**0.02**	**0.01**
Shear wall plastic hinge rotation (rad)	**0.015**	**0.01**
Shear wall coupling beam chord rotation (rad)	**0.03**	**0.018**

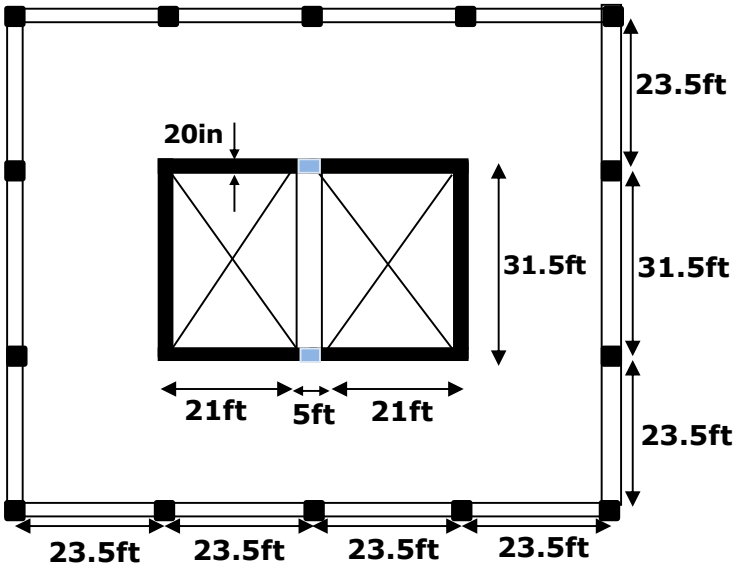

Fig. 3.1 - Plan view of prototype structural system

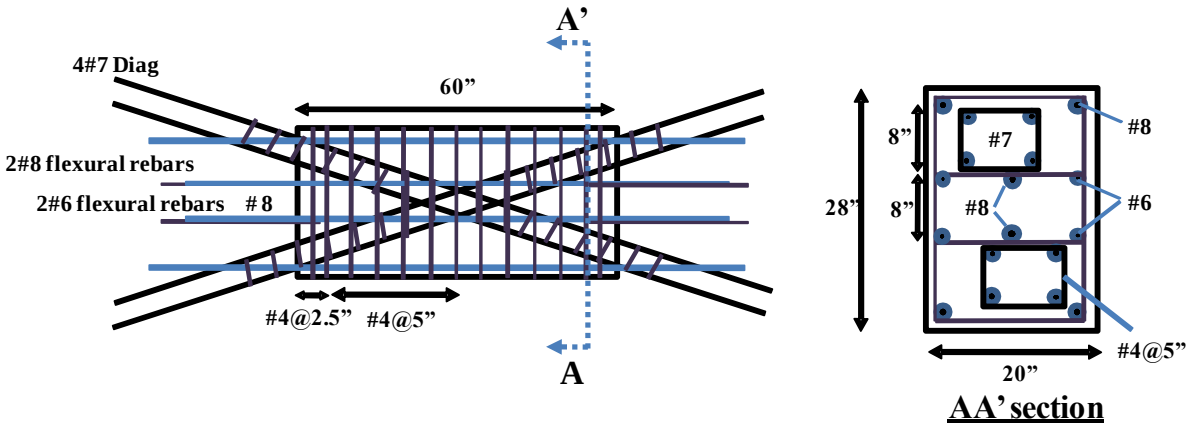

Fig. 3.2 - Reinforcement layout for RC coupling beam

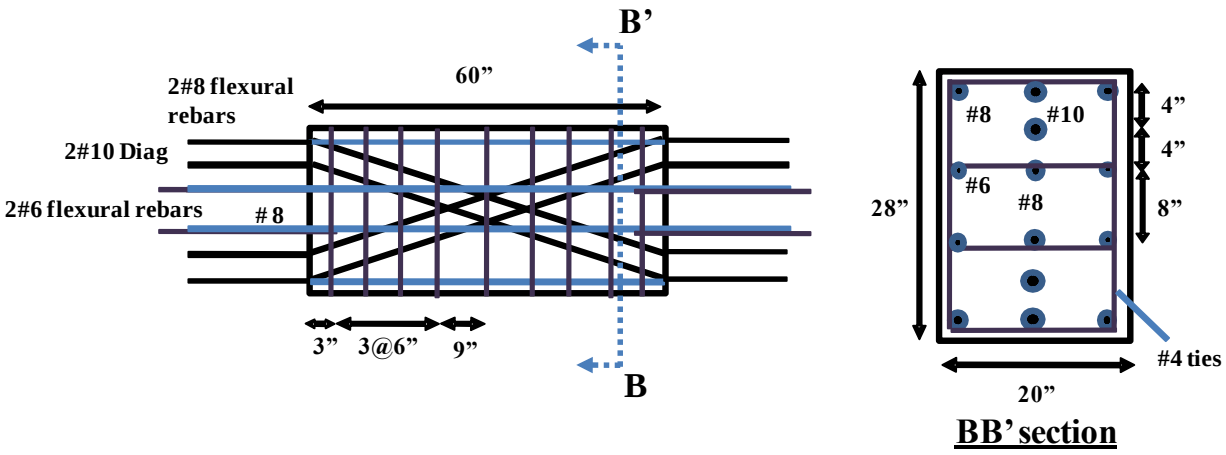

Fig. 3.3 - Reinforcement layout for HPFRC coupling beam

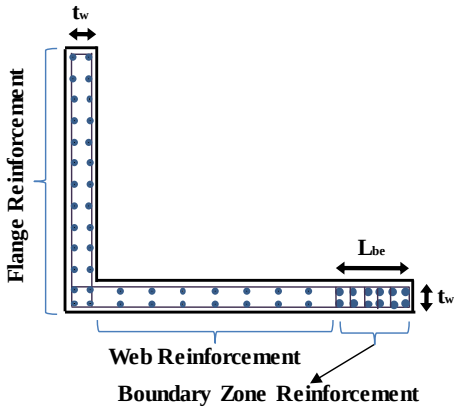

Fig. 3.4 - Shear wall cross section detail

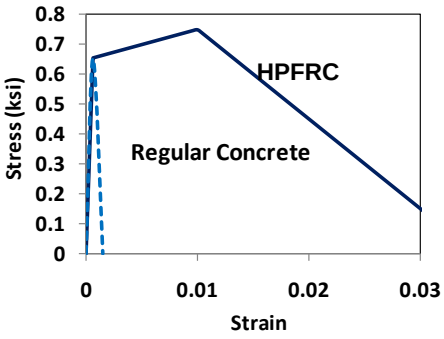

(a) tensile response

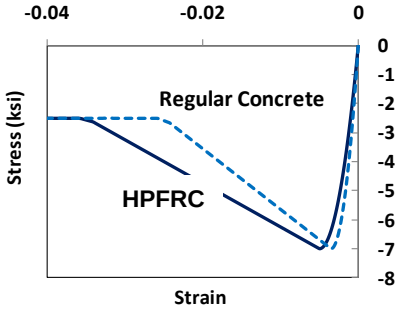

(b) compressive response

Fig. 3.5 - Typical monotonic stress-strain relationship of HPFRC and regular concrete materials

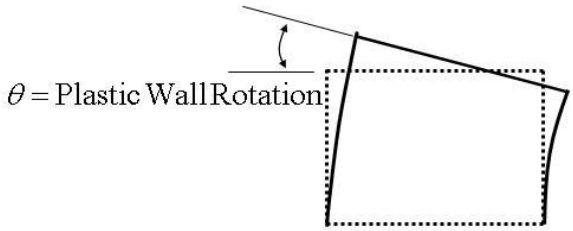

Fig. 3.6 - Definition of wall rotation

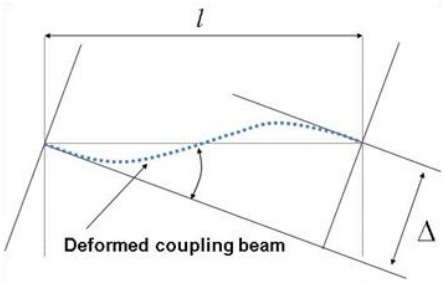

Fig. 3.7 - Definition of coupling beam chord rotation

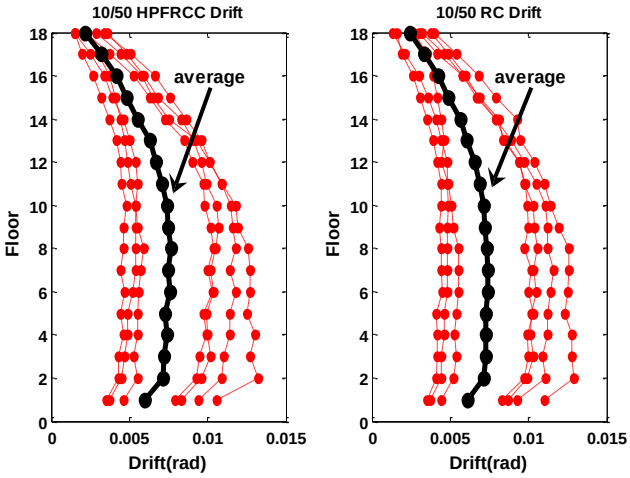

(a) HPFRC system (b) RC system

Fig. 3.8 - Wall rotation levels at peak drift

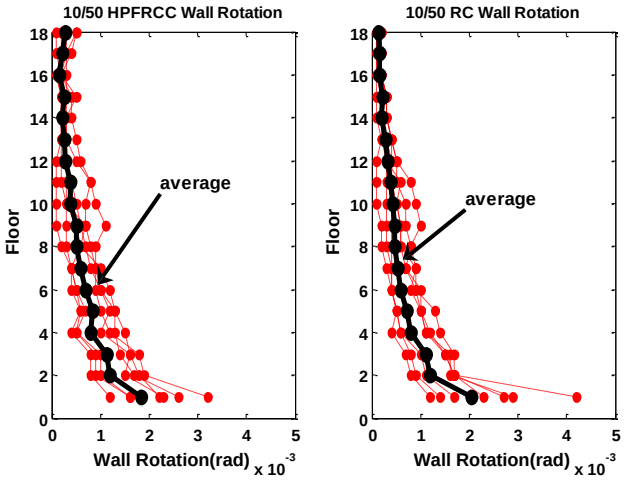

(a) HPFRC system (b) RC system

Fig. 3.9 - Wall rotation levels at peak drift

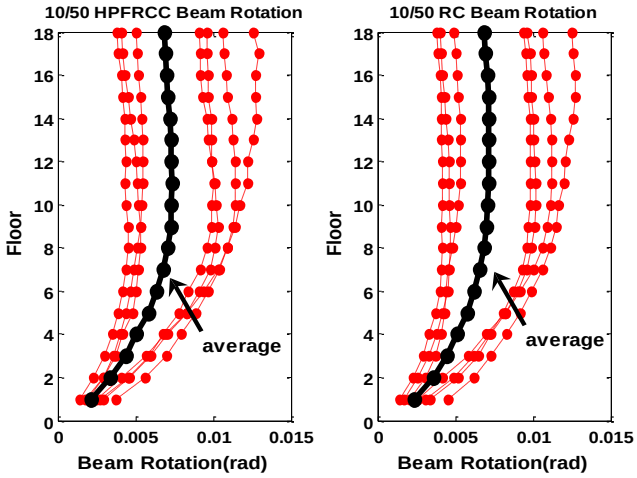

(a) HPFRC system (b) RC system

Fig. 3.10 - Beam rotation demands at peak drift

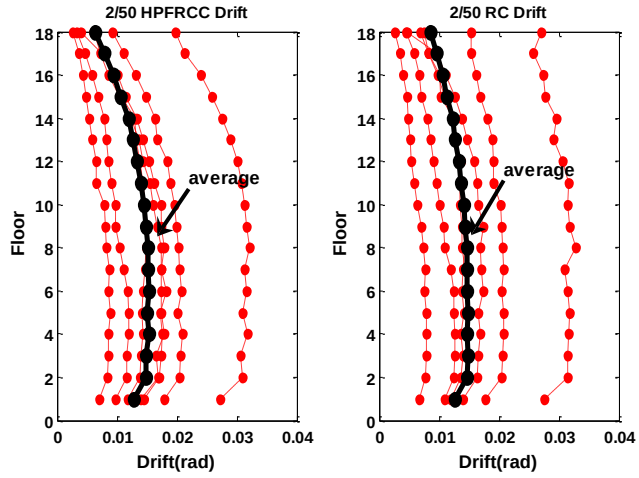

(a) HPFRC system (b) RC system

Fig. 3.11 - Interstory drift of the systems

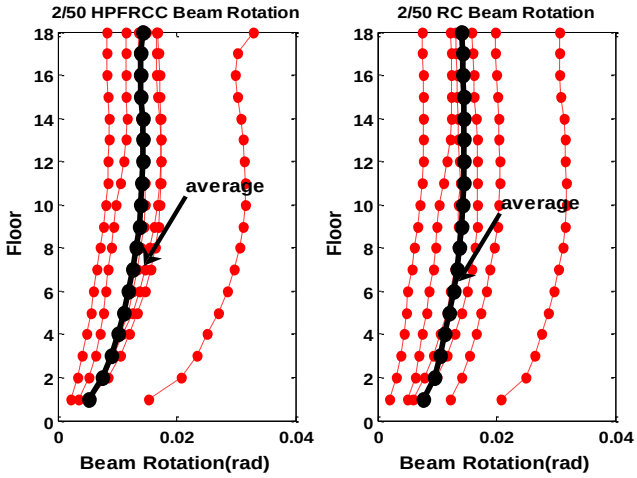

(a) HPFRC system (b) RC system

Fig. 3.12 - Beam rotation levels at peak drift

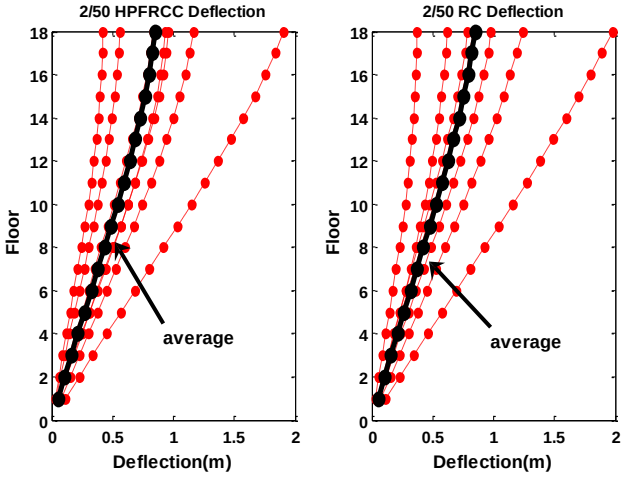

(a) HPFRC system (b) RC system

Fig. 3.13 - Deflection curves at peak drift

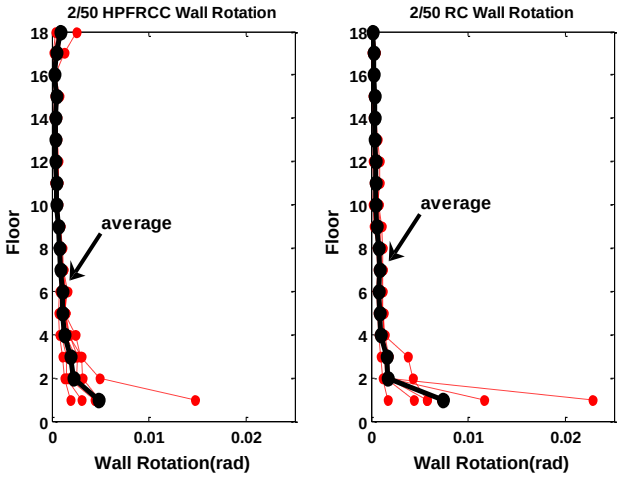

(a) HPFRC system (b) RC system

Fig. 3.14 - Wall rotation levels at peak drift

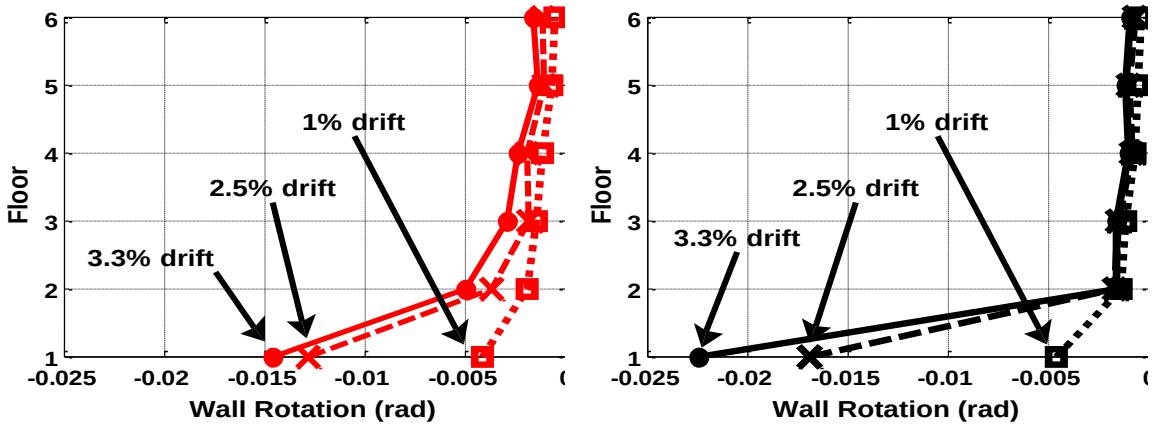

(a) HPFRC system (b) RC system

Fig. 3.15 - Wall rotation levels of the systems with various story drift

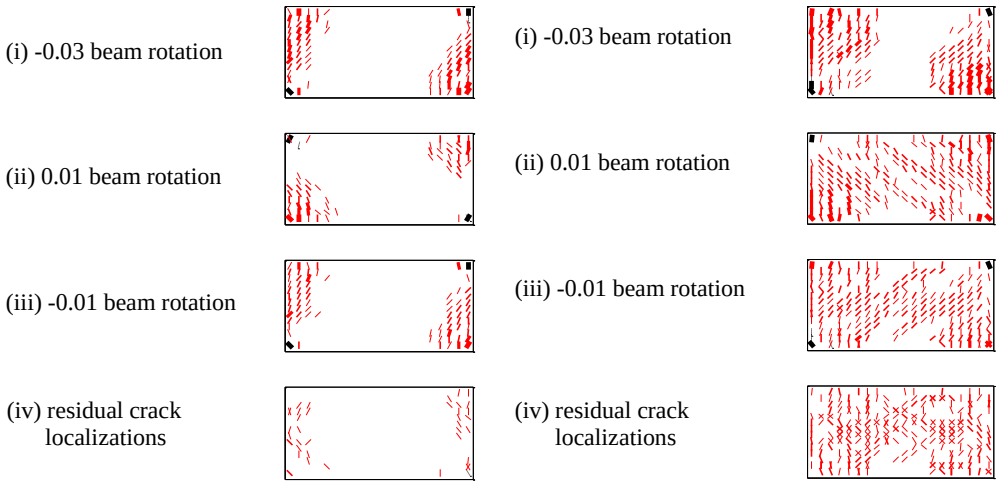

(a) HPFRC coupling beams (b) RC coupling beams

Fig. 3.16 - Crack patterns of RC and HPFRC coupling beams at the 12th floor at various stages of the simulation (unit: rad)

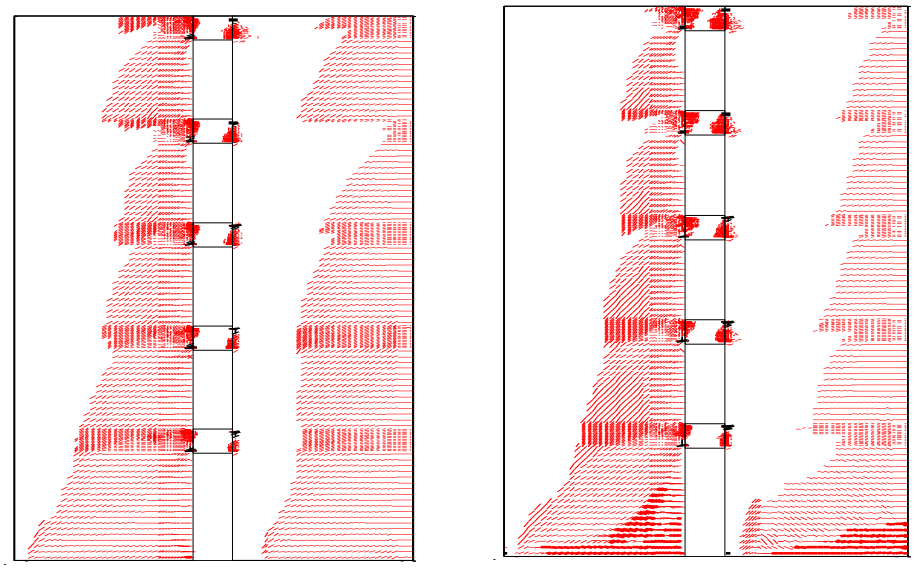

(a) HPFRC system (b) RC system

Fig. 3.17 - Crack patterns of RC and HPFRC walls at the maximum system response

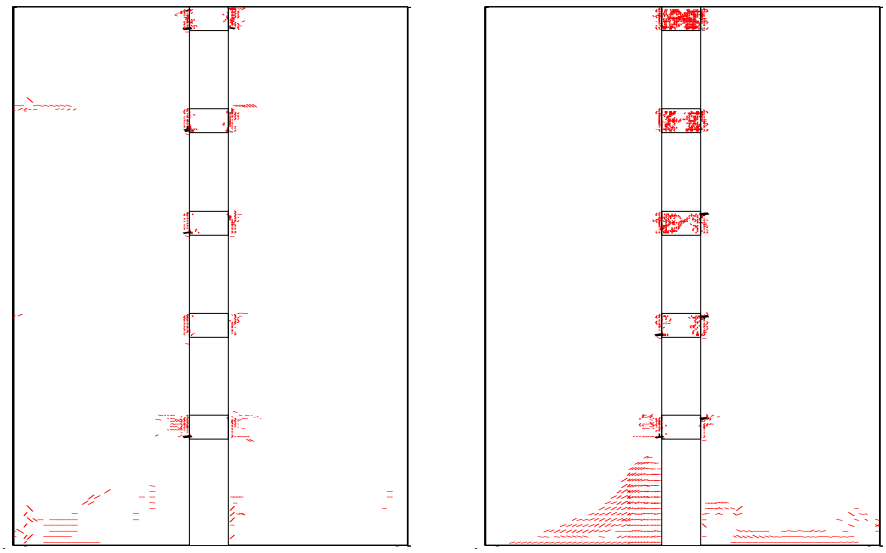

(a) HPFRC system (b) RC system

Fig. 3.18 - Crack patterns of RC and HPFRC walls after the earthquake

3.6 REFERENCES

ACI (American Concrete Institute) Committee 318. (2008). "ACI 318 *Building code requirements for structural concrete (318-08)."* ACI-318, Farmington Hills, Mich.

ASCE (American Society of Civil Engineers). (2002). "SEI/ASCE 7-02: *Minimum Design Loads for Buildings and Other Structures."* American Society of Civil Engineers, Reston, VA.

Canbolat, B. A., Parra-Montesinos, G. J., and Wight, J. K. (2005). "Experimental study on seismic behavior of high-performance fiber-reinforced cement composite coupling beams." *ACI Structural Journal*, 102(1), 159-166.

El-Tawil, S., and Deierlein, G. G. (1999). "Strength and Ductility of Concrete Encased Composite Columns." *Journal of Structural Engineering*, 125(9), 1009–1019.

El-Tawil, S., Kuenzli, C. M., and Hassan, M. (2002a). "Pushover of hybrid coupled walls. I: Design and modeling." Journal of Structural Engineering, 128(10), 1272-1281.

El-Tawil, S., Kuenzli, and C. M. (2002b). "Pushover of hybrid coupled walls. II: Analysis and behavior." Journal of Structural Engineering, 128(10), 1282-1289.

El-Tawil, S., Harries, K. A., Fortney, P. J., Shahrooz, B. M., and Kurama, Y. (2010), "Seismic design of hybrid coupled wall systems – state-of-the-art." Accepted for Publication, *Journal of Structural Engineering*.

FEMA-356. (2000). "*NEHRP Guidelines for the Seismic Rehabilitation of Buildings*." FEMA-356, Applied Technology Council, Redwood City, California.

FEMA-450. (2003). "NEHRP Recommended Provisions for Seismic Regulations for New Buildings and Other Structures." BSSC, Washington, D.C.

Galano L., and Vignoli A. (2000). "Seismic behavior of short coupling beams with different reinforcement layouts." ACI Structural Journal, 97(6), 876-885.

Guizani, L., and Chaallal, O. (1995). "Demande en ductilite des murs de refend couples." Proc., 7th Canadian Conference on Earthquake Engineering, Montreal, 461-468 (in French).

Harries K. A. (2001). "Ductility and deformability of coupling beams in reinforced concrete coupled walls." Earthquake Spectra 17(3): 457-478.

Harries, K. A., Shahrooz, B. M., Brienen, P., Fortney, P., and Rassati G. A. (2004a). "Performance-based design of coupled wall systems." Proceedings of the 5th International Conference on Composite Construction, South Africa, 686-697.

Harries, K. A., Moulton, J. D., and Clemson, R. L. (2004b). "Parametric study of coupled wall behavior-implications for the design of coupling beams." Journal of Structural Engineering, 130(3), 480-488.

Harries, K. A., and Mcneice D. S. (2006). "Performance-based design of high-rise coupled wall systems." The Structural Design of Tall and Special Buildings. 15(3), 289-306.

Hassan, M. (2004). "Inelastic dynamic behavior and design of hybrid coupled wall systems." *Ph.D. Thesis*, Department of Civil and Environmental Engineering, University of Central Florida Orlando, Florida.

Hassan, M., and El-Tawil, S. (2004). " Inelastic dynamic behavior of hybrid coupled walls." Journal of Structural Engineering, 130(2), 285-296.

Hindi, R. A., and Hassan, M. A. (2004). "Shear capacity of diagonally reinforced coupling beams." Engineering Structures, 26(10), 1437-1446.

Hung, C.-C. and El-Tawil, S. (2009). "Cyclic model for high performance fiber reinforced cementitious composite structures." Proceedings of the ATC-SEI conference, Improving the Seismic Performance of Existing Buildings and Other Structures, San Francisco, CA.

Kesner, K. E. and Billington, S. L. (2005). "Investigation of infill panels made from engineered cementitious composites for seismic strengthening and retrofit." Journal of Structural Engineering, 131(11), 1712-1720.

Kim, D. J., El-Tawil, S., and Naaman, A. E. (2009). "Rate-dependent tensile behavior of high performance fiber reinforced cementitious composites." *Materials and Structures*, 42(3), 399-414.

Kwan, A. K. H. and Zhao Z.-Z. (2001). "Cyclic behaviour of deep reinforced concrete coupling beams." Structures and Buildings, 152(3), 283-293.

Li, V. C. (2003). "On engineered cementitious composites (ECC) – a review of the material and its applications." *Journal of Advanced Concrete Technology*, 1(3), 215-230.

Mander, J. B., Priestley, M. J. N., and Park, R. (1988). "Theoretical stress-strain model for confined concrete," *Journal of Structural Engineering*, 114(8), 1804–1826.

Naaman, A. E., and Reinhardt, H. W. (2006). "Proposed classification of HPFRC composites based on their tensile response." *Materials and Structures,* 39(5), 547-555.

Otter, D. E., and Naaman, A. E. (1988). "Properties of steel fiber reinforced concrete

under cyclic loading." ACI Materials Journal, 85(4), 254-261.

Parra-Montesinos, G. J. (2005). "High-performance fiber reinforced cement composites: an alternative for seismic design of structures." ACI Structural Journal, 102(5), 668-675.

Parra-Montesinos, G. J., Canbolat, B. A., and Jeyaraman, G. (2006). "Relaxation of confinement reinforcement requirements in structural walls through the use of fiber reinforced cement composites." 8th National Conference on Earthquake Engineering, San Francisco, CA.

Parra-Montesinos, G. J., and Chompreda, P. (2007). "Deformation capacity and shear strength of fiber reinforced cement composite flexural members subjected to displacement reversals." Journal of Structural Engineering, 133(3), 421-431.

Paulay, T. (1971). "Coupling beams of reinforced concrete shear walls." Journal of Structural Engineering, 97(3), 843-862.

Paulay, T., and Binney, J. R. (1974). "Diagonally reinforced coupling beams of shear walls." Shear in Reinforced Concrete, SP-42. Farmington Hills, MI: American Concrete Institute; 579-598.

Tassios T. P., Moretti, M., and Bezas, A. (1996). "On the behavior and ductility of reinforced concrete coupling beams of shear walls." ACI structural Journal, 93(6), 711-720.

Wight, J. K. and Lequesne, R. D. (2008), "Earthquake-Resistant Design of Coupling Beam Elements Incorporating High-Performance Fiber Reinforced Concrete," Proceedings of International Seminar on Seismic-Resistant Design of Reinforced Concrete Structures, Bogota, D.C., Columbia, May 15, pp. 97-108.

CHAPTER 4

A METHOD FOR ESTIMATING SPECIMEN TANGENT STIFFNESS FOR HYBRID SIMULATION[1]

4.1 INTRODUCTION

Researchers have long recognized the importance and potential benefits of utilizing the tangent stiffness matrix of a test specimen in hybrid simulations employing implicit and mixed integration schemes. However, computation of the tangent stiffness matrix during testing has proved to be challenging, particularly for test specimens with more than one degree-of-freedom. This chapter presents a new methodology that is more straightforward and simpler than existing techniques for computing the tangent stiffness matrix of a multi-degree-of-freedom test specimen. The proposed method is combined with the operator-splitting method and the capabilities, advantages and limitations of the new formulation are demonstrated through several examples. The accuracy, stability, and error propagation characteristics of the modified operator-splitting method are also studied theoretically as well as numerically.

4.2 GENERAL BACKGROUND

[1] The contents of this Chapter are based on a published journal article. Its official citation is
C.C. Hung, S. El-Tawil. A Method for Estimating Specimen Tangent Stiffness for Hybrid Simulation. *Earthquake Engineering and Structural Dynamics*. V38, p115-p134, 2009.

The term *hybrid simulation* commonly refers to a set of methods that combine computational simulation with physical model testing to compute structural dynamic response. In its most general form, hybrid simulation could entail the combination of two or more purely computational models or multiple computational and physical models. In this method, a structure is numerically represented as a discrete mass system and its time-history response to seismic excitation is computed by solving the differential equation of motion of the system. The difference between hybrid simulation and traditional numerical methods is that some of the terms of the restoring force vector in the differential equation of motion are either directly obtained by measurement from a physical test or computed from an associated computational model running in parallel with the main numerical time integration scheme. When the entire restoring force vector is obtained from physical testing, hybrid simulation is commonly referred to as pseudo-dynamic testing. The pseudo-dynamic test technique was first proposed by Takanashi et al. (1978). Since then, many pseudo-dynamic and hybrid testing algorithms have been proposed (Shing and Mahin 1984; Takanashi and Nakashima 1987; Thewalt and Mahin 1987; Combescure and Pegon 1997; Mahin and Shing 1985; Shing et al. 1991, 1994; Nakashima et al. 1992; Thewalt and Mahin 1994; Darby et al. 1999, 2001; Molina et al. 1999; Nakashima and Masaoka 1999; Zhang et al. 2005; Wu et al. 2005; Pan et al. 2006). These algorithms can be categorized as explicit, implicit or mixed algorithms.

The application of explicit algorithms for hybrid testing is limited by the intrinsic stability problem, which restricts the maximum time step that can be imposed. In essence, as the number of degrees of freedom in a system increases, the size of the time step is

bounded and controlled by the system's highest natural frequency. Exceeding the maximum allowable time step will lead to numerical instability and will eventually disrupt the simulation. As the limiting time step becomes smaller, the duration of a hybrid test employing an explicit scheme lengthens. While this results in additional costs and the inconvenience of a long test, a more serious concern is that the time step could become too small to permit a viable test. In such situations, the small time step results in displacement (or force) increments that are too small to reliably apply to a specimen.

Implicit methods, on the other hand, are unconditionally stable and are not hindered by the stability limitation. They are therefore attractive because they permit larger time steps to be taken. However, unless iterations are undertaken to ensure an acceptable level of accuracy, the use of large time steps can lead to an accumulation of errors, especially when nonlinear specimen response occurs. The need for iterations can be alleviated if an accurate tangent stiffness of the test structure is used in the simulations. Nevertheless, computing the tangent stiffness matrix for a multi-degree-of-freedom specimen has traditionally been considered practically difficult, and as a result, most existing implicit algorithms avoid using the tangent stiffness altogether. Instead, iterative corrections of the restoring force on the test specimen are sometimes used (Thewalt and Mahin 1994). However, conducting iterations on a physical specimen is difficult to achieve in practice, especially for inelastic structures, and can lead to path-dependent effects. This difficulty has given rise to mixed explicit-implicit schemes where the objective is to compute an explicit target displacement to avoid iterations on the specimen during testing (e.g. the OS method proposed by Nakashima and Kato (1987)).

As discussed in this chapter, a few researchers have recognized the importance and potential benefits of utilizing the tangent stiffness matrix of the test specimen in implicit and mixed integration schemes and have taken steps to compute or update the tangent stiffness matrix during testing. They used the tangent stiffness for a variety of purposes including correction of the measured restoring force, suppressing displacement control errors, estimating energy errors in the pseudo-dynamic test and compensation for delay in real-time hybrid testing. This chapter presents a new methodology that is more straightforward and simpler than existing techniques for computing the tangent stiffness matrix of a multi-degree-of-freedom test specimen. The proposed method is combined with the operator-splitting method and the capabilities, advantages and limitations of the new formulation are demonstrated through several examples. The accuracy, stability, and error propagation characteristics of the modified operator-splitting method are also studied theoretically as well as numerically.

4.3 INTEGRATION TECHNIQUES FOR HYBRID TESTING

Shing and Mahin (1983, 1984) examined a number of explicit integration techniques and recommended the use of a modified version of the Newmark algorithm which includes frequency-proportional numerical damping. Based on a variation of Newmark's method by Hilbert et al. (1997), Thewalt and Mahin (1987, 1994) suggested an unconditionally stable implicit algorithm for pseudo-dynamic testing. In their method, estimation of structural stiffness is not required to get the restoring force at each time step. The restoring force is measured and corrected continuously within each time step by using the

analog feedback of the instantaneous restoring force associated with the input displacement. This algorithm has substantial advantages for testing structures with many DOFs, where only a few modes contribute to the response. Since larger time steps are permitted by using this algorithm, the number of steps for a test is reduced, thus reducing the testing duration. Nevertheless, the actuator control accuracy remains unknown during testing, and thus the influence of displacement control errors cannot be investigated. Moreover, additional hardware is needed to continuously correct the analog feedback.

To eliminate the drawbacks of the Thewalt and Mahin (1987, 1994) algorithm, Shing et al. (1991) developed an implicit algorithm also based on the implicit algorithm by Hilbert et al. (1977). In their algorithm, they used a parameter to control the size of the displacement at each sub-step before a corrector displacement is applied to the physical specimen. This scheme produces every sub-step in a continuous loading/unloading form such that it prevents loading and unloading iterations on the physical specimen. Shing et al. (1990) used this algorithm successfully to evaluate reinforced masonry shear wall components.

Pan et al. (2006) developed a P2P internet online hybrid test system. In this new system, the equations of motion are not formulated for the entire model, but for each separate substructure instead. During the testing, two rounds of quasi-Newton iteration are used to ensure compatibility and equilibrium between each substructure. However, this scheme was not applied to structures which exhibit significant non-linearity. Also, when the

system includes more physical substructures, it could become more susceptible to experimental errors.

Nakashima et al. (1990) proposed the operator-splitting method (OSM) for pseudo-dynamic testing. In this method, which is a mixed explicit-implicit scheme, an explicit target displacement is computed to avoid iterations on the specimen during testing. This is achieved by approximating the tangent stiffness of the tested structure by its initial stiffness in the restoring force calculations. The method is unconditionally stable when the initial stiffness of the tested structure is greater than the tangent stiffness during the entire test.

Combescure and Pegon (1997) proposed a modification of OSM, which they termed the α operator-splitting method (α-OSM). In this algorithm, the α parameter is introduced into the equations of motion to produce numerical dissipation that eliminates the spurious oscillation induced by control errors in the high frequency modes. When α is set to zero, α-OSM reverts into the regular OSM. The drawback of the method is that when a structure loses a large portion of its initial stiffness during testing, the results could become inaccurate (1997). In α-OSM, the equation of motion of a structural system is expressed as:

$$Ma_{n+1} + (1+\alpha)Cv_{n+1} - \alpha Cv_n + (1+\alpha)r_{n+1} - \alpha r_n = (1+\alpha) f_{n+1} - \alpha f_n \tag{4.1}$$

where M is the mass matrix of the structure; C is the damping coefficient matix; r is the restoring force vector; a is the vector of nodal accelerations; v is the vector of nodal velocities; f is the vector of external excitation forces; subscript n denotes the current time step. The displacement and velocity at the next time step are acquired from a Newmark integration scheme. The obtained displacement and velocity are split into predicted (Eq. 4.2) and corrected (Eq. 4.3) responses.

$$\begin{aligned} \tilde{d}_{n+1} &= d_n + \Delta t v_n + \frac{\Delta t^2}{2}(1-2\beta)a_n \\ \tilde{v}_{n+1} &= v_n + \Delta t(1-\gamma)a_n \end{aligned} \tag{4.2}$$

$$\begin{aligned} d_{n+1} &= \tilde{d}_{n+1} + \Delta t^2 \beta a_{n+1} \\ v_{n+1} &= \tilde{v}_{n+1} + \Delta t \gamma a_{n+1} \end{aligned} \tag{4.3}$$

As previously discussed, the primary assumption of this method is that the restoring force at time step *n+1* can be approximated as

$$r_{n+1}(d_{n+1}) \approx \tilde{r}_{n+1}(\tilde{d}_{n+1}) + K^I\left(d_{n+1} - \tilde{d}_{n+1}\right) \tag{4.4}$$

Substituting Eqs. 4.2 - 4.4 into Eq. 4.1, the acceleration at time step n+1 can be computed as

$$
\begin{aligned}
a_{n+1} &= \hat{M}^{-1}\hat{f}_{n+1} \\
\hat{M} &= M + \gamma\Delta t(1+\alpha)C + \beta\Delta t^2(1+\alpha)K^I \\
\hat{f}_{n+1} &= (1+\alpha)f_{n+1} - \alpha f_n + \alpha\tilde{r}_n - (1+\alpha)\tilde{r}_{n+1} + \alpha C\tilde{v}_n - (1+\alpha)C\tilde{v}_{n+1} + \alpha\left(\gamma\Delta tC + \beta\Delta t^2 K^I\right)a_n
\end{aligned} \quad (4.5)
$$

When the physical test structure becomes inelastic, the primary assumption of OSM and α-OSM that the tangent stiffness of the specimen can be replaced with its initial stiffness (i.e., Eq. 4.4) becomes inaccurate, and can adversely affect the accuracy of the test method.

A few researchers have taken steps to compute and incorporate the tangent stiffness matrix during testing. Efforts appear to be limited because of the practical difficulty of directly estimating the tangent stiffness as the test progresses. One of the earliest attempts to employ the tangent stiffness during testing was by Nakashima and Kato (1987). They estimated the tangent stiffness in an effort to correct the measured restoring force and suppress displacement control errors. In their work, they collected the necessary information from sub-steps within a time step to estimate the tangent stiffness. Nevertheless, they only used the estimated tangent stiffness to modify the restoring force instead of merging the estimated tangent stiffness with the integration algorithm as is done in this chapter.

Thewalt and Roman (1994) developed an approach based on the BFGS formula (Nocedal and Wright 1999) to estimate the tangent stiffness during testing. They used the estimated tangent stiffness to estimate energy errors in the pseudo-dynamic test. Carrion and Spencer (2006) estimated the tangent stiffness based on the Broyden formula (Broyden

1965). They used the estimated tangent stiffness for compensation of delay in real-time hybrid testing.

In this chapter, a new strategy for estimating the tangent stiffness is proposed. The scheme is general in that it can be applied to a variety of implicit and mixed integration methods. However, in this work, the new methodology is combined with the traditional OSM to show the resulting advantages of implementing it within a hybrid simulation framework. These advantages are demonstrated using a series of hybrid simulation exercises, including test structures that exhibit significant inelastic behavior and that have multiple degrees of freedom.

4.4 PROPOSED OPERATOR-SPLITTING METHOD WITH UPDATED TANGENT STIFFNESS (OSM-US)

The incremental force and displacement at time step n+1 can be associated through the tangent stiffness at time step n+1 as

$$\begin{Bmatrix} \Delta\tilde{r}_{n+1}^{(1)} \\ \Delta\tilde{r}_{n+1}^{(2)} \\ \vdots \\ \vdots \\ \Delta\tilde{r}_{n+1}^{(dof)} \end{Bmatrix}_{dof\times 1} = \begin{bmatrix} K_{n+1}^{1,1} & K_{n+1}^{1,2} & \cdots & \cdots & K_{n+1}^{1,dof} \\ K_{n+1}^{2,1} & K_{n+1}^{2,2} & & & K_{n+1}^{2,dof} \\ \vdots & \vdots & & & \vdots \\ \vdots & \vdots & & & \vdots \\ K_{n+1}^{dof,1} & K_{n+1}^{dof,2} & \cdots & \cdots & K_{n+1}^{dof,dof} \end{bmatrix}_{dof\times dof} \begin{Bmatrix} \Delta\tilde{d}_{n+1}^{(1)} \\ \Delta\tilde{d}_{n+1}^{(2)} \\ \vdots \\ \vdots \\ \Delta\tilde{d}_{n+1}^{(dof)} \end{Bmatrix}_{dof\times 1} \tag{4.6}$$

where $\Delta\tilde{r}_{n+1}^{(q)}$ is the incremental restoring force at the q^{th} degree-of-freedom (*dof*) of the model at time step *n+1*. $K_{n+1}^{x,y}$ is the component value at (*x*,*y*) position of the tangent

stiffness matrix at time step *n+1*. $\Delta\tilde{d}_{n+1}^{(q)}$ is the incremental predicted displacement at the q^{th} *dof* of the model at time step *n+1*.

By assuming that the tangent stiffness does not change substantially during the current and previous *m-1* steps, i.e. for a total of *m* steps from time step *n+2-m* to *n+1*, the relation between the incremental force and the incremental displacement during the time interval *n+2-m* to *n+1* can be expressed as

$$\begin{Bmatrix} \Delta\tilde{r}_{n+2-m}^{(1)} & \Delta\tilde{r}_{n+3-m}^{(1)} & \cdots & \cdots & \Delta\tilde{r}_{n+1}^{(1)} \\ \Delta\tilde{r}_{n+2-m}^{(2)} & \Delta\tilde{r}_{n+3-m}^{(2)} & \cdots & \cdots & \Delta\tilde{r}_{n+1}^{(2)} \\ \vdots & \vdots & & & \vdots \\ \vdots & \vdots & & & \vdots \\ \Delta\tilde{r}_{n+2-m}^{(dof)} & \Delta\tilde{r}_{n+3-m}^{(dof)} & \cdots & \cdots & \Delta\tilde{r}_{n+1}^{(dof)} \end{Bmatrix}_{dof\times m} = \begin{bmatrix} K_{n+1}^{1,1} & K_{n+1}^{1,2} & \cdots & \cdots & K_{n+1}^{1,dof} \\ K_{n+1}^{2,1} & K_{n+1}^{2,2} & & & K_{n+1}^{2,dof} \\ \vdots & \vdots & & & \vdots \\ \vdots & \vdots & & & \vdots \\ K_{n+1}^{dof,1} & K_{n+1}^{dof,2} & \cdots & \cdots & K_{n+1}^{dof,dof} \end{bmatrix}_{dof\times dof} \begin{Bmatrix} \Delta\tilde{d}_{n+2-m}^{(1)} & \Delta\tilde{d}_{n+3-m}^{(1)} & \cdots & \cdots & \Delta\tilde{d}_{n+1}^{(1)} \\ \Delta\tilde{d}_{n+2-m}^{(2)} & \Delta\tilde{d}_{n+3-m}^{(2)} & \cdots & \cdots & \Delta\tilde{d}_{n+1}^{(2)} \\ \vdots & \vdots & & & \vdots \\ \vdots & \vdots & & & \vdots \\ \Delta\tilde{d}_{n+2-m}^{(dof)} & \Delta\tilde{d}_{n+3-m}^{(dof)} & \cdots & \cdots & \Delta\tilde{d}_{n+1}^{(dof)} \end{Bmatrix}_{dof\times m} \quad (4.7)$$

Transposing Eq. 4.7,

$$\begin{Bmatrix} \Delta\tilde{r}_{n+2-m}^{(1)} & \Delta\tilde{r}_{n+2-m}^{(2)} & \cdots & \cdots & \Delta\tilde{r}_{n+2-m}^{(dof)} \\ \Delta\tilde{r}_{n+3-m}^{(1)} & \Delta\tilde{r}_{n+3-m}^{(2)} & \cdots & \cdots & \Delta\tilde{r}_{n+3-m}^{(dof)} \\ \vdots & \vdots & & & \vdots \\ \vdots & \vdots & & & \vdots \\ \Delta\tilde{r}_{n+1}^{(1)} & \Delta\tilde{r}_{n+1}^{(2)} & \cdots & \cdots & \Delta\tilde{r}_{n+1}^{(dof)} \end{Bmatrix} = \begin{bmatrix} \Delta\tilde{d}_{n+2-m}^{(1)} & \Delta\tilde{d}_{n+2-m}^{(2)} & \cdots & \cdots & \Delta\tilde{d}_{n+2-m}^{(dof)} \\ \Delta\tilde{d}_{n+3-m}^{(1)} & \Delta\tilde{d}_{n+3-m}^{(2)} & \cdots & \cdots & \Delta\tilde{d}_{n+3-m}^{(dof)} \\ \vdots & \vdots & & & \vdots \\ \vdots & \vdots & & & \vdots \\ \Delta\tilde{d}_{n+1}^{(1)} & \Delta\tilde{d}_{n+1}^{(2)} & \cdots & \cdots & \Delta\tilde{d}_{n+1}^{(dof)} \end{bmatrix} \begin{Bmatrix} K_{n+1}^{1,1} & K_{n+1}^{2,1} & \cdots & \cdots & K_{n+1}^{dof,1} \\ K_{n+1}^{1,2} & K_{n+1}^{2,2} & & & K_{n+1}^{dof,2} \\ \vdots & \vdots & & & \vdots \\ \vdots & \vdots & & & \vdots \\ K_{n+1}^{1,dof} & K_{n+1}^{2,dof} & \cdots & \cdots & K_{n+1}^{dof,dof} \end{Bmatrix} \quad (4.8)$$

For Eq. 4.8 to yield a solution, the number of considered time steps, *m*, must be equal to or larger than the number of *dof* in the test structure, i.e. $m \geq dof$. Eq. 4.8 can be partitioned into *dof* equations as shown in Eq. 4.9.

$$\left\{\begin{Bmatrix}\Delta\tilde{r}^{(1)}_{n+2-m}\\ \Delta\tilde{r}^{(1)}_{n+3-m}\\ \vdots\\ \vdots\\ \Delta\tilde{r}^{(1)}_{n+1}\end{Bmatrix}\begin{Bmatrix}\Delta\tilde{r}^{(2)}_{n+2-m}\\ \Delta\tilde{r}^{(2)}_{n+3-m}\\ \vdots\\ \vdots\\ \Delta\tilde{r}^{(2)}_{n+1}\end{Bmatrix}\ \cdots\ \cdots\ \begin{Bmatrix}\Delta\tilde{r}^{(dof)}_{n+2-m}\\ \Delta\tilde{r}^{(dof)}_{n+3-m}\\ \vdots\\ \vdots\\ \Delta\tilde{r}^{(dof)}_{n+1}\end{Bmatrix}\right\}=\begin{bmatrix}\Delta\tilde{d}^{(1)}_{n+2-m} & \Delta\tilde{d}^{(2)}_{n+2-m} & \cdots & \cdots & \Delta\tilde{d}^{(dof)}_{n+2-m}\\ \Delta\tilde{d}^{(1)}_{n+3-m} & \Delta\tilde{d}^{(2)}_{n+3-m} & \cdots & \cdots & \Delta\tilde{d}^{(dof)}_{n+3-m}\\ \vdots & \vdots & & & \vdots\\ \vdots & \vdots & & & \vdots\\ \Delta\tilde{d}^{(1)}_{n+1} & \Delta\tilde{d}^{(2)}_{n+1} & \cdots & \cdots & \Delta\tilde{d}^{(dof)}_{n+1}\end{bmatrix}\left\{\begin{Bmatrix}K^{1,1}_{n+1}\\ K^{1,2}_{n+1}\\ \vdots\\ \vdots\\ K^{1,dof}_{n+1}\end{Bmatrix}\begin{Bmatrix}K^{2,1}_{n+1}\\ K^{2,2}_{n+1}\\ \vdots\\ \vdots\\ K^{2,dof}_{n+1}\end{Bmatrix}\ \cdots\ \cdots\ \begin{Bmatrix}K^{dof,1}_{n+1}\\ K^{dof,2}_{n+1}\\ \vdots\\ \vdots\\ K^{dof,dof}_{n+1}\end{Bmatrix}\right\} \quad (4.9)$$

When $m = dof$ in Eq. 4.9, a unique solution can be found for the tangent stiffness coefficients. However, when $m > dof$ in Eq. 4.9, the system becomes over determined, and the least squares method, for example, as implemented in (MATLAB 2007), can be used to solve for the tangent stiffness matrix.

The initial stiffness in the regular OSM and α-OSM (as shown in Eq. 4.4) can now be replaced by the estimated tangent stiffness computed from Eq. 4.9. The restoring force at time step $n+1$ is now approximated as:

$$r_{n+1}(d_{n+1}) \approx \tilde{r}_{n+1}(\tilde{d}_{n+1}) + K^{T}_{n+1}\left(d_{n+1} - \tilde{d}_{n+1}\right) \quad (4.10)$$

where K^{T}_{n+1} is the tangent stiffness at time step $n+1$. As shown in Fig. 4.1, the restoring force, $r_{n+1}(d_{n+1})$, is an approximation of the sum of the predicted restoring force, $\tilde{r}_{n+1}(\tilde{d}_{n+1})$, which is the feedback from the substructures subjected to the predicted displacement, and a modification term, $K^{T}_{n+1}\left(d_{n+1} - \tilde{d}_{n+1}\right)$, which is the difference between the predicted and actual displacement multiplied by the tangent stiffness. Equivalent force equilibrium using the tangent stiffness can now be expressed as:

$$\hat{M}_{n+1} a_{n+1} = \hat{f}_{n+1}$$
$$\hat{M}_{n+1} = M + \frac{\Delta t C_{n+1}}{2} + \frac{\Delta t^2 K_{n+1}^T}{4} \tag{4.11}$$
$$\hat{f}_{n+1} = f_{n+1} - \tilde{r}_{n+1} - C_{n+1} \tilde{v}_{n+1}$$

The procedure for hybrid simulation using OSM-US is illustrated in Fig. 4.2. The predicted displacement and velocity are first computed based on the response from the previous time step. After the predicted displacements are imposed upon the test specimen, the resulting reaction forces, $\tilde{r}_{n+1}$, and the actual imposed displacements, $\tilde{d}_{n+1}^{m}$, are measured. Then, the incremental values of the restoring forces and the measured displacements from the current and previous *m-1* steps are used to calculate the tangent stiffness matrix. The damping coefficient, equivalent force and equivalent mass are then updated using the tangent stiffness. After that, the acceleration, the corrected displacement and velocity of the current time step are computed from Eq. 4.3 and Eq. 4.11, and are used for the next time step.

Two rules are imposed on the algorithm to ensure reasonable results. The first resets the reloading/unloading tangent stiffness to the initial stiffness right after the point where the displacement direction changes. After reloading/unloading at this point, the original scheme continues collecting the previous records and estimating the stiffness. This rule limits the proposed method to structures dominated by first mode response, where unloading of one member is associated with unloading of the entire structure. The second rule is more practical in nature. It filters out the steps where the imposed displacements are smaller than a user-specified threshold, specified as a minimum incremental

displacement. This is to ensure that only steps that are large enough to contribute reliably to the stiffness calculations are utilized in the computations. Although user experience clearly plays a role in identifying this parameter, a number that is 2-3 times the displacement resolution of the actuator is recommended.

4.5 NUMERICAL SIMULATION OF HYBRID TESTING USING OSM-US

As discussed above and in (Combescure and Pegon 1997; Nakashima et al. 1990), the use of the traditional OSM for pseudo-dynamic testing could generate unreliable results, especially for structures whose stiffness degrades significantly during testing. The new OSM-US methodology proposed herein alleviates this problem. To highlight the advantages of OSM-US, four numerical models that are designed to exhibit significant inelastic behavior during hybrid simulation are used. The simulations are conducted without damping and with 3% Rayleigh damping. As shown in Fig. 4.3a, Model 1 represents a 1-story, 1 degree-of-freedom, structure. Model 2 (Fig. 4.3b) represents a 2-story structure with 2 lateral DOFs. Model 3 (Fig. 4.3c) represents a 6-story structure with 6 lateral DOFs. In Model 4, a 2-story structure is split into 2 substructures (Fig. 4.3d). The bottom substructure, which would usually be physically tested in a hybrid simulation, is numerically simulated here, while the top column is treated as a numerical substructure.

The cross-section of the column used in all examples is shown in Fig. 4.4. OpenSees (OpenSees version 1.7 2006) is used to model the inelastic behavior of the members. Concrete02 and Steel01 material models in OpenSees are used to represent concrete and

steel, respectively. Parameter definitions and properties of the material models are shown in Fig. 4.5 and Table 4.1. The 1940 El Centro earthquake history record with PGA=0.36g is used as the external excitation throughout this study.

Lateral displacement control for Model 1 (Fig. 4.3a) is achieved using the pseudo-dynamic method with both OSM and OSM-US. The results are compared together along with the reference results from OpenSees in Fig. 4.6. A comparison of the displacement responses in Fig. 4.6a shows that OSM deviates a little from the reference solution, especially at the peaks, while OSM-US consistently matches the results well. The computed hysteresis responses are shown in Fig. 4.6b, which shows that the simulated solution from OSM-US matches the reference solution better than that from OSM, especially when the model experiences significant inelastic behavior.

The behavior of Model 2 (Fig. 4.3b) also demonstrates the capabilities of OSM-US. Simulation of the undamped model is conducted with an incremental time step 0.005sec and m = 3. The resulting displacement responses from OpenSees, OSM, and OSM-US are compared in Fig. 4.7, which indicates that both integration methods appear to match the reference results from OpenSees quite well. However, as shown in Fig. 4.7b, the cumulative energy error, E_c, computed for the top-node response, shows that the error from OSM-US is less than half of the result computed from OSM. The cumulative energy error is defined as

$$E_c: \sum_{j=1}^{j=n} \left| \left(r_j\right)_{OSM-US/OSM} \left[\left(d_j\right)_{OSM-US/OSM} - \left(d_j\right)_{opensees} \right] \right| \tag{4.12}$$

$\left(d_j\right)_{MOSM/OSM}$ is the displacement of node of interest computed from OSM-US or OSM; $\left(d_j\right)_{opensees}$ is the displacement of the node of interest from OpenSees; $\left(r_j\right)_{MOSM/OSM}$ is the restoring force at the same node from OSM-US or OSM, and n is the current time step.

The same model (Model 2), but with 3% damping, more clearly demonstrates the advantages of OSM-US over OSM. It is obvious from Fig. 4.8 that the resulting displacement from OSM deviates from the reference OpenSees solution, whereas the OSM-US results remain very good. The success of OSM-US in this case is due to its ability to utilize the correct tangent stiffness matrix in the Rayleigh damping computations.

Model 3 (Fig. 4.3c) is simulated with a time step of 0.005sec and m = 8. Fig. 4.9a shows the response of the undamped model. Again, although the differences between OSM and OSM-US are not obvious in this figure, E_c computed at the top node from OSM-US is significantly less than that for OSM, as observed in Model 2. Also, as observed in Model 2, differences in displacement response become more pronounced when damping is accounted for (Fig. 4.9b). In this case OSM-US is much closer to the reference solution than OSM.

The influence of m on the simulation results is shown in Fig. 4.10. Fig. 4.10a shows E_c computed at the top node. It is observed that the cumulative energy becomes larger as m increases. Recall that the minimum value for m is the number of degrees of freedom. At m=80, the cumulated energy error from OSM-US is close to that from OSM. Fig. 4.10b

indicates that the disagreement between the displacement response from OSM-US and the reference solution becomes larger as *m* continues to increase.

To better understand the influence of *m* and why accuracy degrades as *m* increases beyond a certain limit, consider that the 1st and 2nd mode periods for Example 3 are 4.9 seconds and 0.8 seconds, respectively. When *m*=40, the imposed displacements and reaction forces from the past 40 time steps, corresponding to a duration of 0.2 seconds in this case, are used to estimate the current tangent stiffness. In other words, immediately after the point of unloading/reloading, the proposed scheme uses the initial stiffness for integration for 0.2 seconds, a period during which significant inelasticity occurs. Fig. 4.11 demonstrates this idea and shows that for a structure vibrating solely in 2nd mode, the 0.2 seconds is too large a fraction of the 2nd mode period to allow realistic updating of the stiffness properties. Clearly the results will continue to deteriorate as *m* increases.

The trends observed in Models 1 through 3 are also observed in Model 4, which is solved using *m*=8 and a smaller time step of 0.002sec due to the high axial stiffness of the column.

4.6 ERROR PROPAGATINON CHARACTERISTICS OF OSM-US

Actuator control errors occur during a hybrid test with a physical component. In order to gauge the effect of displacement control errors on the proposed OSM-US, numerical simulation of a hybrid experiment with induced displacement control errors is conducted. Model 2, Fig. 4.3b, is selected for this purpose. To simulate the effect of control errors, a random displacement control error signal with an average of 0 and a variance of 3E-7

inch is introduced. The resulting maximum control error is 1.75E-3 inch, which is within the range of accuracy of commercially available actuators. The simulation result is shown in Fig. 4.12 and compared to the results from OpenSees (without induced errors). It can be observed from Fig. 4.12 that the effect of the induced displacement control errors on the resulting response from OSM-US is negligible for this particular case. Nevertheless, if the error propagation induced by actuator control errors is considered to be too deleterious, the T-Modification strategy suggested by Nakashima and Kato (1987) can be applied to mitigate displacement control errors. The T-Modification approach is only possible in this case because the tangent stiffness matrix is available through the OSM-US algorithm.

Compatibility between substructures in hybrid simulation is assured through displacement control of the DOFs at the boundaries between experimental and numerical substructures. However, equilibrium, i.e. the presence of unbalanced forces, at the boundaries between both substructures is not necessarily assured unless iterations are performed. Since OSM-US, which employs a specimen's tangent stiffness, traces the nonlinear response better than OSM, which utilizes the initial stiffness, it is expected that unbalanced forces will be reduced at the interface.

To investigate the growth of unbalanced forces in both OSM and OSM-US, the hybrid simulation involving Model 4 is used. Unbalanced moments at the interface are measured through a normalized quantity, $\left|\frac{M_t + M_b}{M_{\max}}\right|$, where M_t is the moment at the boundary node

from top element; M_b is the moment at the boundary node from the bottom element; $M_{\max}$ is the maximum moment in both elements during the simulation. The result is extracted and plotted for a portion of response as shown in Fig. 4.13. It can be seen from the linear regression of the unbalanced force that the OSM-US has significantly reduced unbalanced forces compared to OSM. It is noted that the larger unbalanced force segments in the OSM-US correspond to the portion where the initial tangent stiffness is used for integration. This result suggests that OSM-US can improve the quality of the solution with fewer iterations if iterations are deemed necessary.

4.7 STABILITY AND ACCURACY CHARACTERISTICS OF OSM-US

When OSM-US is applied to hybrid simulation, the equations of motion for an elastic, single degree of freedom system can be written as

$$Ma_{n+1} + \left[C^{EST}(v_{n+1} - \tilde{v}_{n+1}) + C^{R}(\tilde{v}_{n+1})\right] + \left[K^{EST}(d_{n+1} - \tilde{d}_{n+1}) + K^{R}(\tilde{d}_{n+1})\right] = F_{n+1} \qquad (4.13)$$

where C^{EST} and K^{EST} are the estimated damping coefficient and tangent stiffness, and C^{R} and K^{R} are the real damping coefficient and tangent stiffness, respectively. Eq. 4.13 can be further rearranged in a recursive form as shown in Eq. 4.14.

$$X_{n+1} = AX_n \qquad (4.14)$$

Where $X_n = \begin{Bmatrix} \tilde{d}_n \\ \tilde{v}_n \Delta t \\ a_n \Delta t^2 \end{Bmatrix}$; $A = \begin{bmatrix} 1 & 1 & 1 \\ 0 & 1 & 1 \\ P & Q & Q \end{bmatrix}$, is the amplification matrix,

$P = \dfrac{-\Omega^2}{1+\beta\xi\Omega+\frac{1}{4}\alpha\Omega^2}$, $Q = \dfrac{-2\Omega\xi-\Omega^2}{1+\beta\xi\Omega+\frac{1}{4}\alpha\Omega^2}$, $\xi = \dfrac{C^R}{2M\omega}$, and $\Omega = \omega\Delta t = \sqrt{\dfrac{K^R}{M}}\Delta t$. α is defined as the estimation error of the tangent stiffness and is expressed as $\alpha = \dfrac{K^{EST}}{K^R}$; β is defined as the estimation error of the damping and is expressed as $\beta = \dfrac{C^{EST}}{C^R}$.

The stability and accuracy of OSM-US can be investigated through the characteristics of the matrix A (Hilber et al. 1997). The spectral radius, $\rho(A)$, is the maximum absolute eigenvalue of A. The algorithm is stable when $\rho(A) \le 1$. With $\alpha = \beta = 1$, the spectral radius versus Ω with varying ξ can be plotted as shown in Fig. 4.14. It can be seen that the stability of OSM-US increases (i.e., spectral radius reduces) as ξ increases.

The effect of the accuracy of the computed tangent stiffness on the stability can also be investigated. In this case, ξ is fixed at 2%, and β =1. The result is plotted in Fig. 4.15a. It can be seen from the figure that the stability drops as the accuracy of the estimated tangent stiffness decreases. By fixing $\alpha = 1$ and ξ = 2%, the relationship between the spectral radius versus Ω with varying β is plotted in Fig. 4.15b. It shows that stability increases with a lower β, but the influence of β on stability is not as obvious as α.

The numerical accuracy of OSM-US is related to the ratio of period distortion and numerical damping (Wu et al. 2005; Shing and Mahin 1985). The non-zero eigenvalues of A can be expressed as

$$\lambda_{1,2} = \exp\left[\left(-\hat{\xi} \pm i\right)\overline{\Omega}\right] = L_1 \pm iL_2 \tag{4.15}$$

where $\hat{\xi} = -\frac{\ln(L_1^2 + L_2^2)}{2\overline{\Omega}}; \overline{\Omega} = \tan^{-1}\left(\frac{L_2}{L_1}\right)$. Also, the displacement solution for a viscously underdamped free-vibration response can be written as (Wu et al. 2005)

$$D_n = \exp(-\xi'\overline{\omega}_n n\Delta t)\left[c_1 \cos(\overline{\omega}_d n\Delta t) + c_2 \sin(\overline{\omega}_d n\Delta t)\right] \tag{4.16}$$

where $\xi' = \frac{\hat{\xi}}{\sqrt{1+\hat{\xi}^2}}$, $\overline{\omega}_d = \frac{\overline{\Omega}}{\Delta t}$, and $\overline{\omega}_n = \frac{\overline{\omega}_d}{\sqrt{1-\xi^2}}$. The numerical damping is defined as

$$\overline{\xi} = \xi' - \xi \tag{4.17}$$

In the case of $\alpha = 1$, the variation of numerical damping ratio against Ω with varying ξ is shown in Fig. 4.16a. It can be seen that the numerical damping ratio is negative and its absolute value increases with higher Ω and ξ. The correlation of the numerical damping ratio versus Ω with varying α is plotted in Fig. 4.16b for ξ = 2%. It is clear that the numerical damping ratio is also negative for the assumed parameters. Furthermore, the absolute value of the numerical damping ratio increases as the accuracy of the estimated

tangent stiffness decreases. A study of the variation of the numerical damping ratio versus Ω with varying β showed that the absolute value of the numerical damping ratio increases as β becomes larger, but that the difference between the results for varying β is minor.

Period distortion can be expressed as

$$\frac{\Delta T_d}{T_d} = \frac{T_d - \overline{T}_d}{T_d} = 1 - \frac{\omega_d}{\overline{\omega}_d} = 1 - \frac{\Omega}{\overline{\Omega}}\sqrt{1-\xi^2} \tag{4.18}$$

Period distortion against Ω with varying α is plotted in Fig. 4.17a for $\beta = 1$ and $\xi = 0.02$. It can be seen that the period extends for the prescribed parameters. However, distortion can be alleviated by increasing the accuracy of the estimated tangent stiffness. Using $\alpha = 1$, and $\xi = 0.02$, period distortion against Ω with varying β is plotted in Fig. 4.17b. It is shown that period distortion increases with increasing β. Nevertheless, the effect of β on the period distortion is not significant. Finally, it can be observed from Eq. 4.18 that the effect of varying ξ on period distortion is not obvious since the damping ratios for most civil structures are less than 5%.

4.8 SUMMARY

A strategy for estimating the tangent stiffness of a structural system during hybrid simulation was proposed in this chapter. The new method is based upon the premise that the specimen's tangent stiffness does not change substantially during the few steps

preceding the current time integration step. By exploiting this assumption, it was possible to solve a set of equations (possibly over-determined) to identify the full stiffness matrix for a multi-degree-of-freedom test specimen. Although the proposed technique is general and can be applied to a variety of the implicit algorithms for time-stepping integration, it was combined in this work with the operator-splitting method resulting in a new operator-splitting formulation designated OSM-US.

The capabilities, advantages and limitations of OSM-US were discussed and demonstrated through several examples of single and multi-degree-of-freedom specimens. The research results showed that the proposed algorithm provides results that are better than those produced via the regular operator-splitting method alone, especially for damped structures undergoing highly inelastic behavior during testing. The enhancement was observed in improved displacement calculations, reduced cumulative energy errors, and lower unbalanced forces between substructures in the examples studied. The accuracy, stability, and error propagation characteristics of the modified operator-splitting method were also studied theoretically as well as numerically. Specifically, the study quantified the effect of tangent stiffness estimation error on the stability and accuracy of a single degree-of-freedom model.

Table 4.1 - Material parameters of the concrete and steel models

Concrete properties	***fpc(ksi)***	***epsc0***	***fpcu(ksi)***	***epsU***	***q***	***ft(ksi)***	***Ets(ksi)***
Unconfined concrete	-6	-0.002	-0.4	-0.01	0.1	0.6	300
Confined concrete	-7.2	-0.0045	-2.4	-0.03	0.1	0.72	360
Steel bar properties	***fy(ksi)***	***E0(ksi)***	***B***				
	60	29000	0.01				

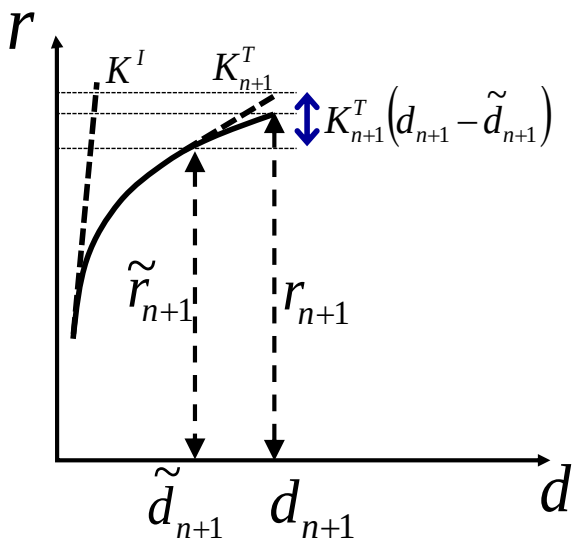

Fig. 4.1 - The approximated restoring force at time step n+1

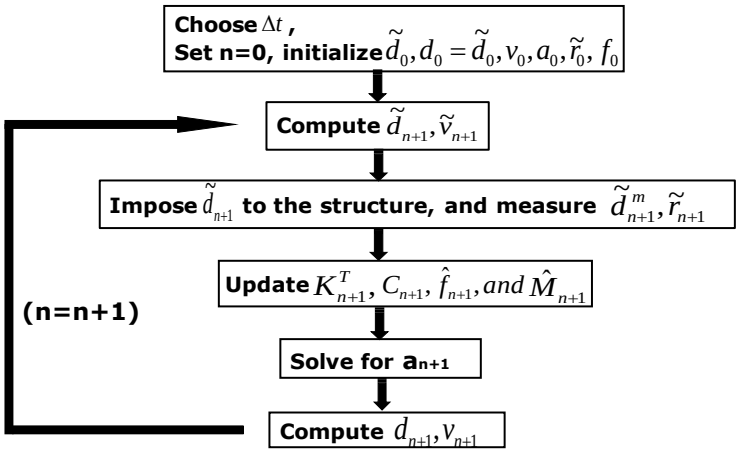

Fig. 4.2 - Flowchart of OSM-US operations

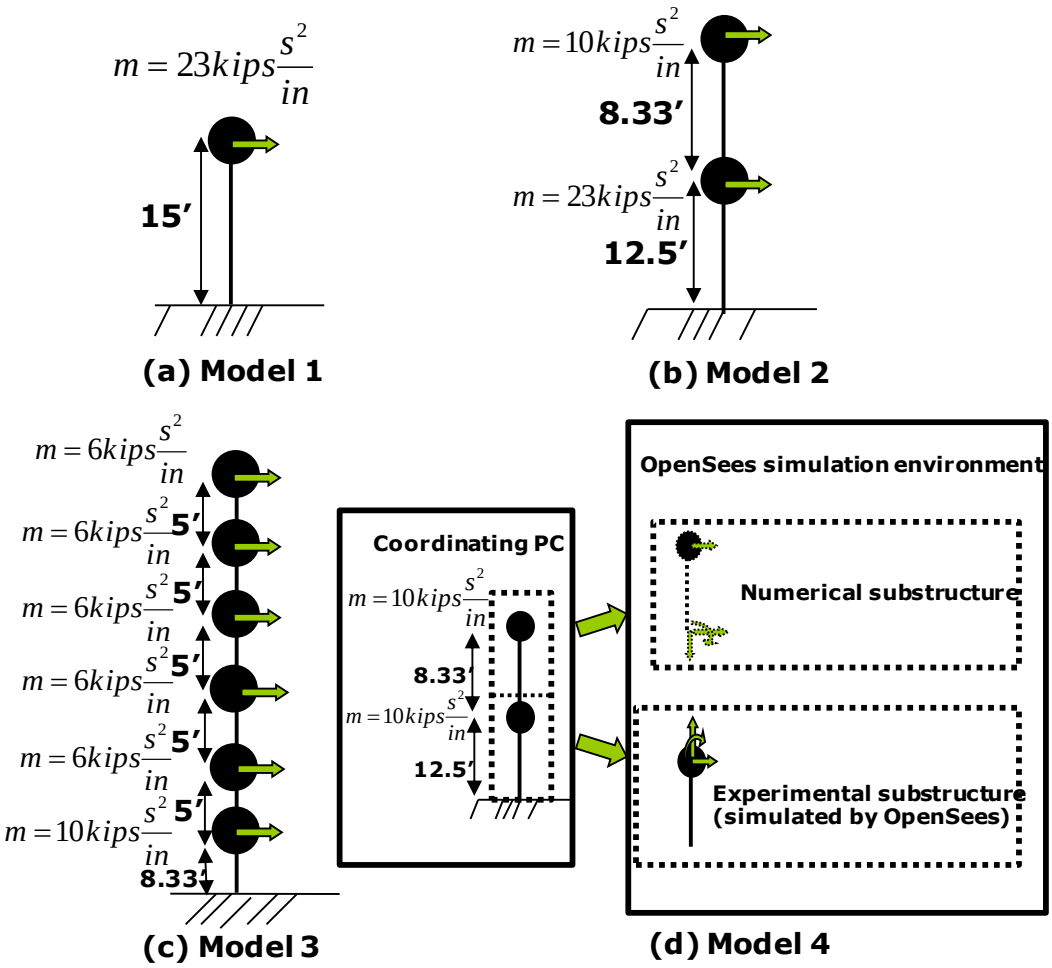

Fig. 4.3 - Demonstration examples of the proposed OSM-US

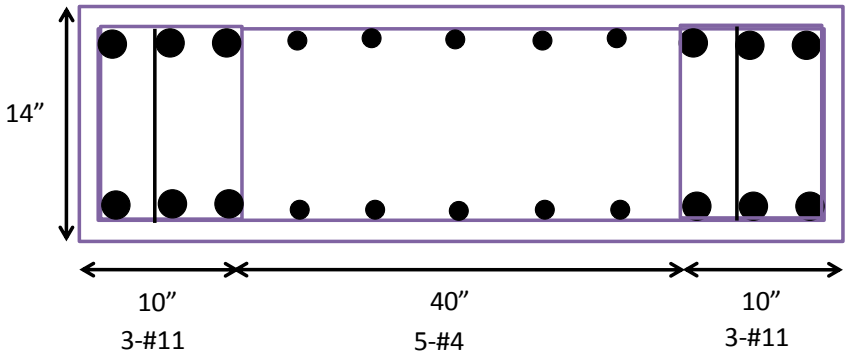

Fig. 4.4 - Cross-section of the column used in the examples

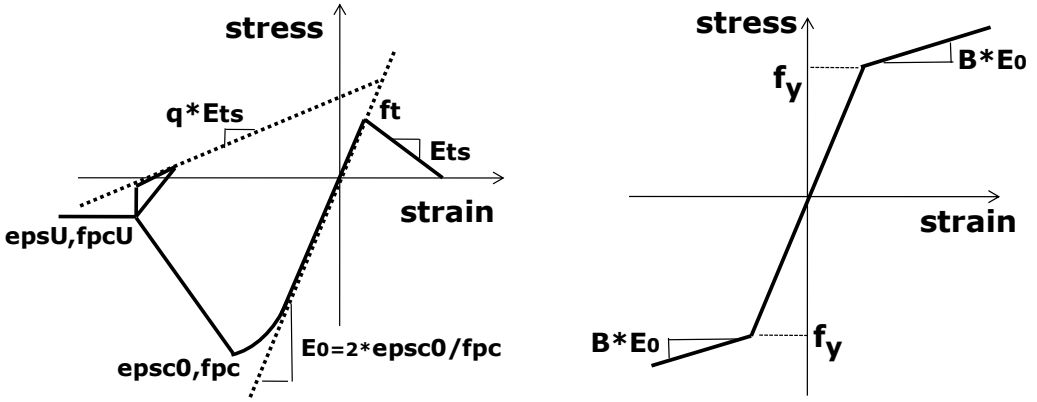

(a) Concrete02 model and its parameters (b) Steel01 model and its parameters

Fig. 4.5 - Concrete and steel bar material models in OpenSees

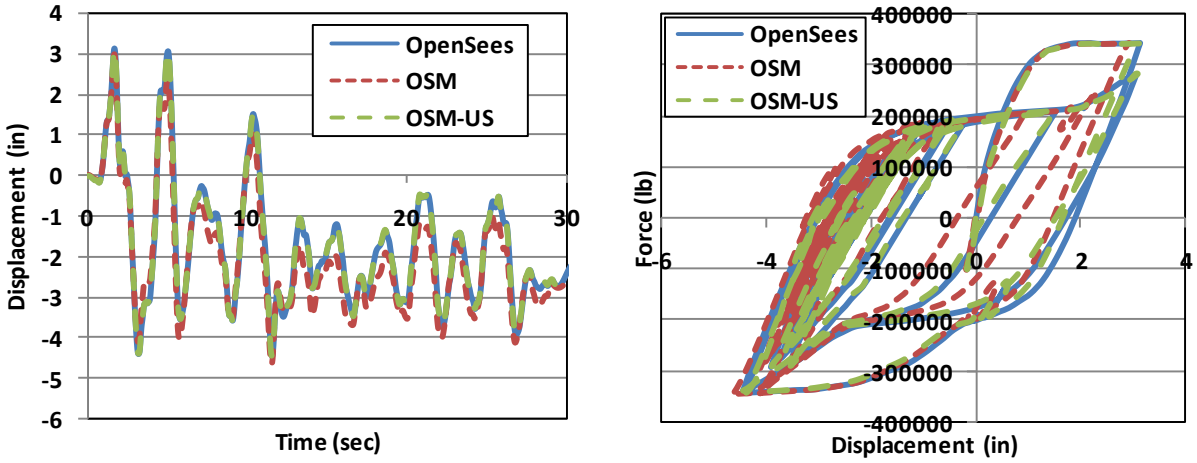

(a) Displacement of top node (b) Hysteresis response

Fig. 4.6 - Simulated responses for Model 1

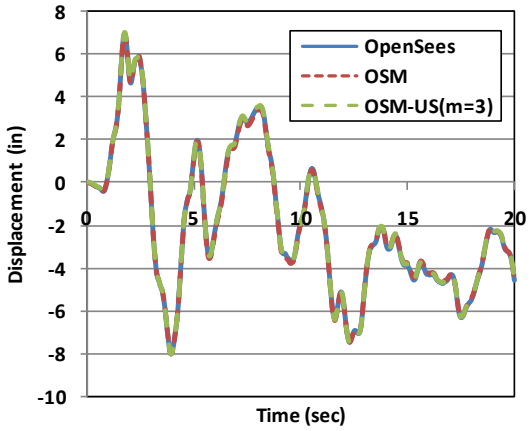

(a) displacement response of top node

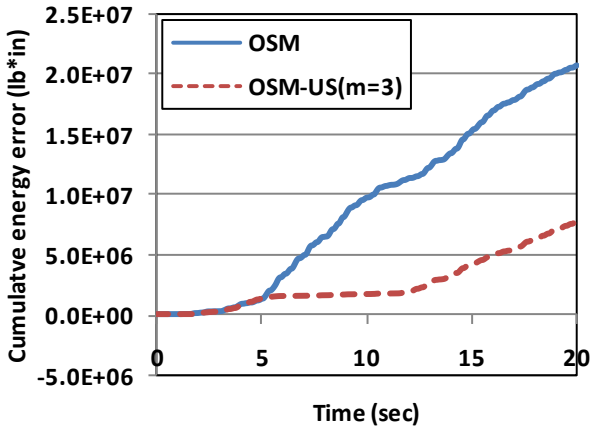

(b) cumulative energy index

Fig. 4.7 - Simulated top-node responses of undamped Model 2

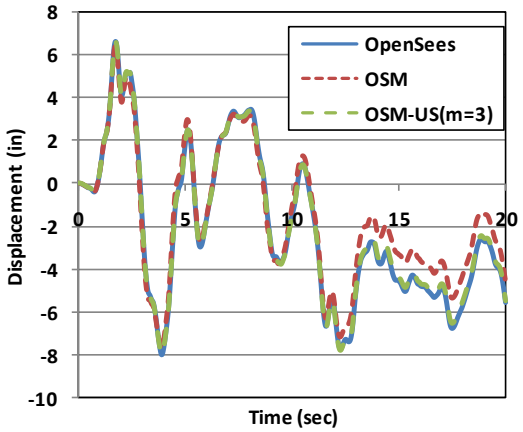

Fig. 4.8 - Computed top-node response of Model 2 (damped)

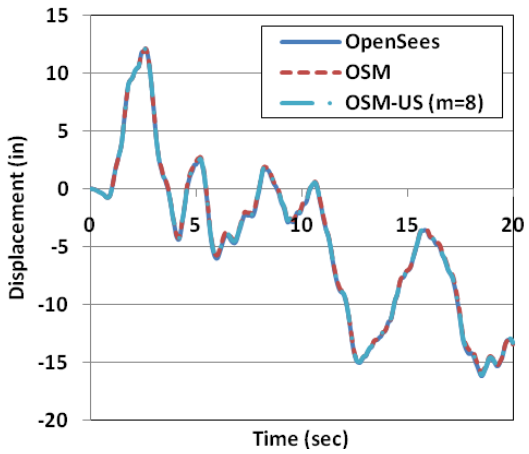

(a) Undamped response

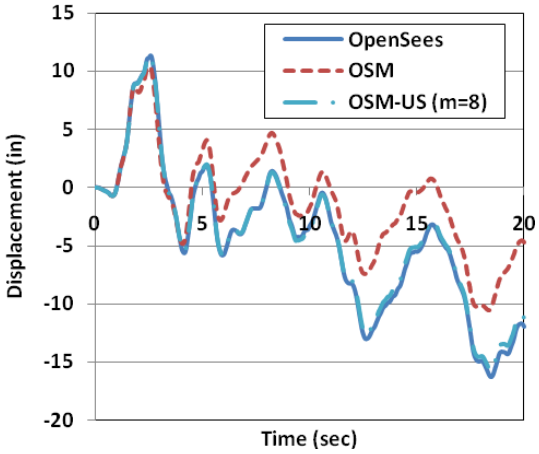

(b) Damped response

Fig. 4.9 - Simulated top-node responses of Model 3

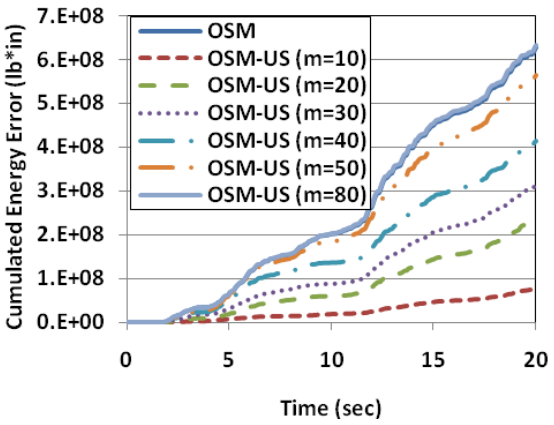

(a) Cumulative energy error

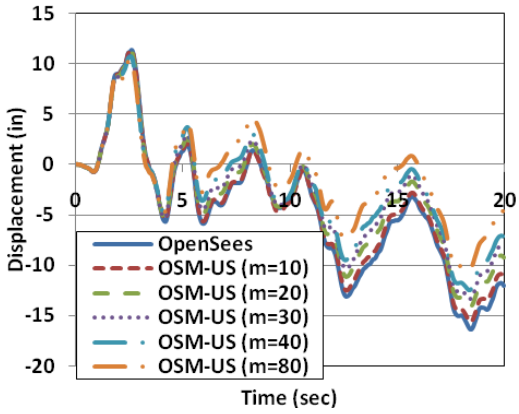

(b) Displacement of the top node

Fig. 4.10 - Effect of *m* parameter on response of Model 3

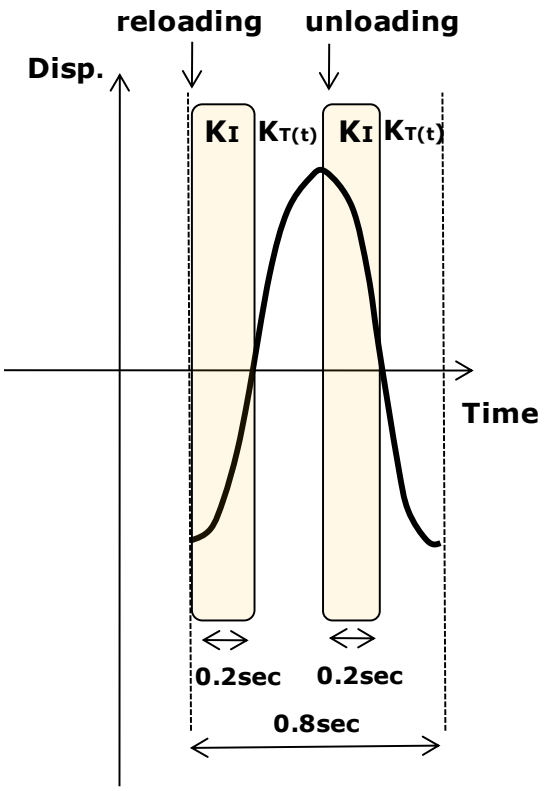

Fig. 4.11 - The approximate distribution of the stiffness for the 2nd mode response

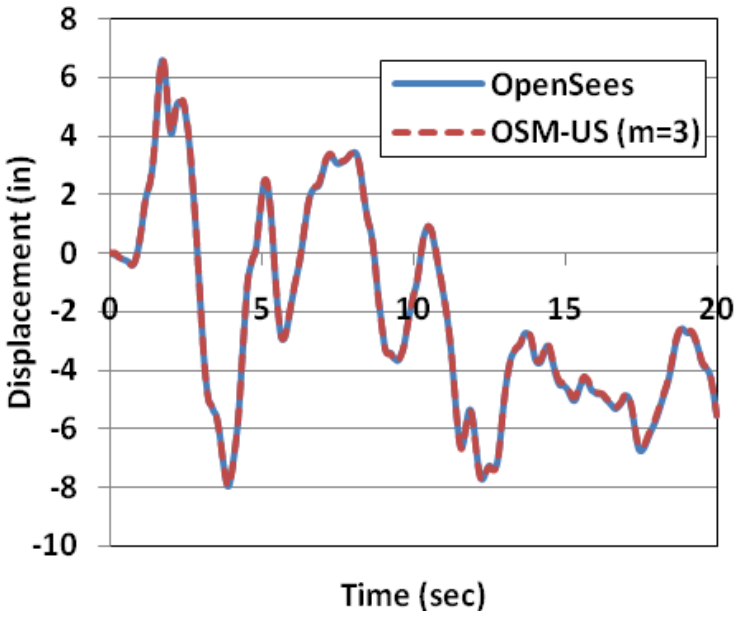

Fig. 4.12 - Effect of induced displacement control errors on the response of top-node in Model 2

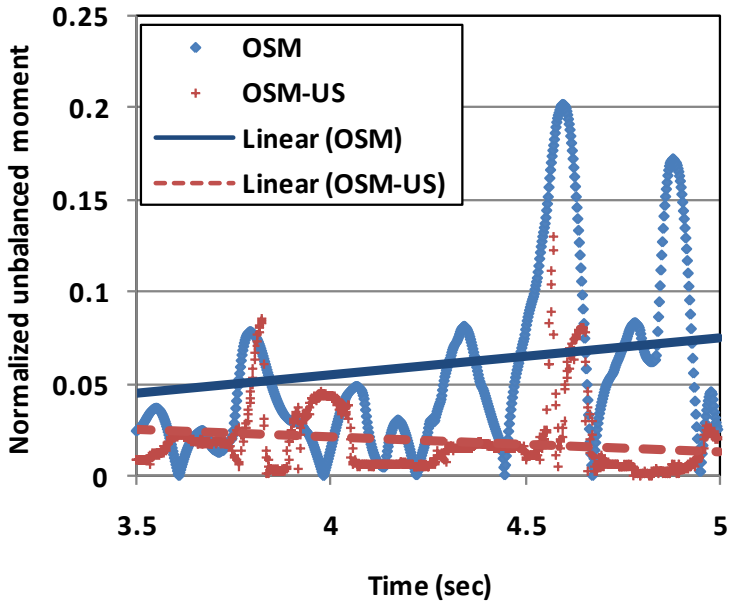

Fig. 4.13 - Normalized unbalanced moment between substructures in Model 4

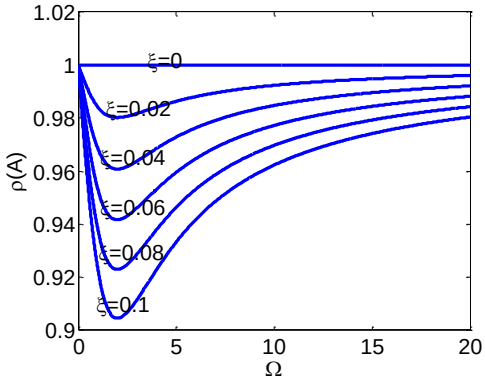

Fig. 4.14 - Trends in the spectral radius with varying Ω and ξ ($(\alpha = \beta = 1)$)

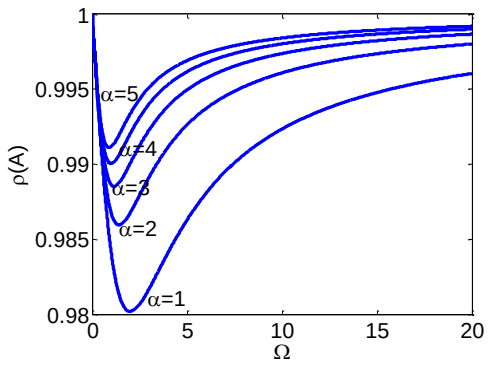

(a) Ω with varying α ($\beta=1, \xi=0.02$)

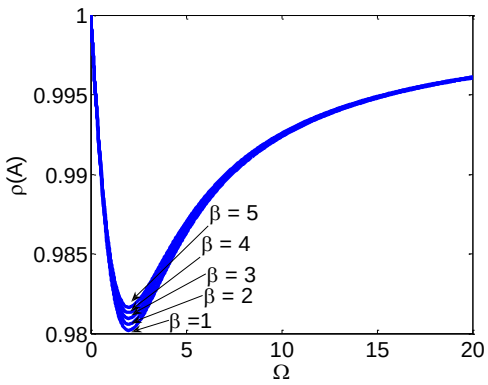

(b) Ω with varying β ($\alpha=1, \xi=0.02$)

Fig. 4.15 - Trends in the spectral radius with varying Ω and ξ ($\alpha=\beta=1$)

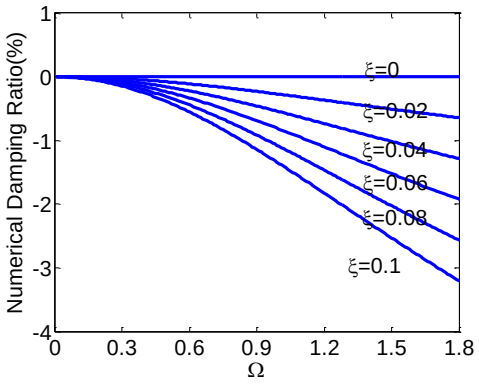

(a) Ω with varying ξ

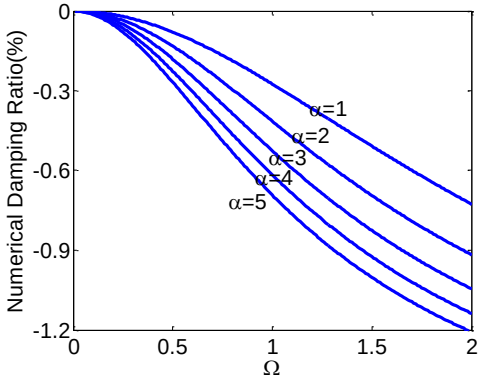

(b) Ω with varying α

Fig. 4.16 - Trends in the numerical damping ratio

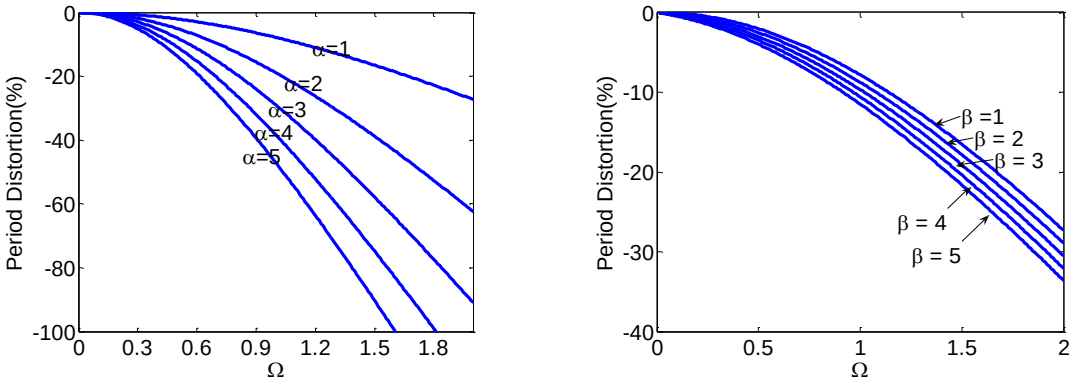

(a) Ω with varying α ($\beta = 1, \xi = 0.02$) (b) Ω with varying β ($\alpha = 1, \xi = 0.02$)

Fig. 4.17 - Trends in period distortion versus Ω

4.9 REFERENCES

Broyden CG. A class of methods for solving nonlinear simultaneous equations. Mathematics of Computation 1965; 19:577-593.

Carrion JE, Spencer BF. Real-time hybrid testing using model-based delay compensation. Proceedings of the 4th International Conference on Earthquake Engineering, Taipei, Taiwan, 2006.

Combescure D, Pegon P. α-operator splitting time integration technique for pseudodynamic testing. Error propagation analysis, Soil Dynamics and Earthquake Engineering 1997, v 16, n 7-8, 427-443.

Darby AP, Blakeborough A, Williams MS. Real-time substructure tests using hydraulic actuator. Journal of Engineering Mechanics (ASCE) 1999; 125(10):1133-1139.

Darby AP, Blakeborough A, Williams MS. Improved control algorithm for real-time substructure testing. Earthquake Engineering and Structural Dynamics 2001; 30:431-448.

Hilber HM, Hughes TJR, Taylor RL. Improved numerical dissipation for time integration algorithm in structural dynamics. Earthquake Engineering and Structural Dynamics 1977; 5, 283-292.

Mahin SA, Shing PB. Pseudodynamic method for seismic testing. Journal of Structural Engineering (ASCE) 1985; 111(7):1482-1503.

MATLAB R2006a Help Manual, 2007.

Molina FJ, Verzeletti G, Magonette G, Buchet P, Geradin M. Bi-directional pseudodynamic test of a full-size three-storey building. Earthquake Engineering and Structural Dynamics 1999; 28:1541-1566.

Nakashima M, Kato H. Experimental error growth behavior and error growth control in on-line computer test control method. Building Research Institute, Ministry of Construction 1987.

Nakashima M, Kaminosono T, Ishida M, Ando K. Integration techniques for substructure pseudo dynamic test. 4th U.S. National Conference on Earthquake Engineering, Palm Springs, California, 1990; 515-524.

Nakashima M, Kato H, Takaoka E. Development of real-time pseudo dynamic testing. Earthquake Engineering and Structural Dynamics 1992; 21:79-92.

Nakashima M, Masaoka N. Real-time on-line test for MDOF systems. Earthquake Engineering and Structural Dynamics 1999; 28(4):393-420.

Nocedal J and Wright SJ. Numerical Optimization. Springer-Verlag. ISBN 0-387-98793-2, 1999.

OpenSees version 1.7 User Manual, Pacific Earthquake Engineering Research Center, University of California, Berkeley, 2006, http://opensees.berkeley.edu.

Pan P, Tomofuji H, Wang T, Nakashima M, Ohsaki M, Mosalam K. Development of peer-to-peer (P2P) internet online hybrid test system. Earthquake Engineering and Structural Dynamics 2006; 35:867-890.

Shing PB, Mahin SA. Experimental error propagation in pseudodynamic testing. Report No. UCB/EERC-83/12, Earthquake Engineering Research Center, University of California, Berkeley, 1983.

Shing PB, Mahin SA. Pseudodynamic test method for seismic performance evaluation: Theory and implementation. Report No. UCB/EERC-84/12. Earthquake Engineering Research Center, University of California, Berkeley, 1984.

Shing PB, Mahin SA. Computational aspects of a seismic performance test method using on-line computer control. Earthquake Engineering and Structural Dynamics 1985; 13:507-526.

Shing PB, Vannan MT, Carter E. Evaluation of reinforced masonry shear wall components by pseudodynamic testing. Proceedings of the 4th U.S. National Conference on Earthquake Engineering, Palm Springs, California, 1990; 829-838.

Shing PB, Vannan MT, Cater E. Implicit time integration for pseudodynamic tests. Earthquake Engineering and Structural Dynamics 1991; 20:551-576.

Shing PB, Bursi OS, Vannan MT. Pseudodynamic tests of a concentrically braced frame using substructuring techniques. Journal of Constructional Steel Research 1994; 29:121-148.

Takanashi K, Nakashima M. Japanese activities on on-line testing. Journal of Structural Engineering (ASCE) 1987; 113(7):1014-1032.

Thewalt CR, Mahin SA. Hybrid solution techniques for generalized pseudodynamic testing. Report No. UCB/EERC-87/09, Earthquake Engineering Research Center, University of California, Berkeley, 1987.

Thewalt CR, Mahin SA. An unconditionally stable hybrid pseudodynamic algorithm. Earthquake Engineering and Structural Dynamics 1994; 24:723-731.

Thewalt CR, Roman M. Performance parameters for pseudodynamic tests. Journal of Structural Engineering (ASCE) 1994; 120(9):2768-2781.

Wu B, Bao H, Ou J, Tian S. Stability and accuracy analysis of central difference method for real-time substructure testing. Earthquake Engineering and Structural Dynamics 2005; 34:705-718.

Zhang Y, Sause R, Ricles JM, Naito CJ. Modified predictor-corrector numerical scheme for real-time pseudo dynamic tests using state-space formulation. Earthquake Engineering and Structural Dynamics 2005; 34:271-288.

CHAPTER 5

FULL OPERATOR ALGORITHM FOR HYBRID SIMULATION[1]

5.1 INTRODUCTION

As mentioned in Chapter 4, the Operator-Splitting method (OSM) (Nakashima et al. 1990; Nakashima and Kato 1987) is a commonly used technique for hybrid simulation. One of the weaknesses of this method is that its corrector step employs the approximation that incremental forces are linearly related to the tested structure's initial stiffness matrix. This chapter presents a new predictor-corrector technique in which the assumptions about the tested structure's response are shifted to the predictor step, which results in an enhancement in overall simulation accuracy, especially for nonlinear structures. Unlike OSM, which splits the displacement and velocity operators into explicit and implicit terms, the new method uses predicted accelerations to compute fully-explicit displacement and velocity values in the predictor step. Another advantage of the proposed technique, termed the Full Operator Method (FOM) is that its formulation makes it suitable for both quasi-static and real-time hybrid simulation. The effectiveness

[1] The contents of this Chapter are based on a published journal article and a submitted journal paper. Their official citations are
C.C. Hung, S. El-Tawil. Full Operator Algorithm for Hybrid Simulation. *Earthquake Engineering and Structural Dynamics* V38, p1545-1561, 2009.
C.C. Hung, S. El-Tawil. Stability Characteristics of the Full Operator Method for Hybrid Simulation. *Engineering Structures*. (submitted January 2010)

of FOM is demonstrated by investigating error propagation in a set of single and multi degree-of-freedom models. A formal investigation of the stability of FOM shows that FOM is conditionally stable and has a stability criterion similar to that of the central difference method. A new version of FOM with enhanced stability characteristics is then proposed and the numerical characteristics, including stability and accuracy, of the modified FOM (mFOM) are investigated analytically.

5.2 OPERATOR-SPLITTING METHOD (OSM)

An attractive feature of OSM is that it is effectively transformed into an explicit scheme when the tangent stiffness matrix of the structure, which is usually considered difficult to estimate during testing, is replaced by the initial stiffness matrix. Consider the equation of motion of a discrete structural system:

$$Ma_{n+1} + Cv_{n+1} + r_{n+1} = f_{n+1} \tag{5.1}$$

where M is the mass matrix of the structure; C is the damping coefficient matrix; r is the restoring force vector; f is the vector of external excitation forces. The displacement and velocity at the next time step, n+1, obtained using Newmark's integration scheme can be expressed as

$$\begin{aligned} d_{n+1} &= \left\{ d_n + \Delta t v_n + \frac{\Delta t^2}{2}(1-2\beta)a_n \right\} + \Delta t^2 \beta a_{n+1} \\ v_{n+1} &= \left\{ v_n + \Delta t(1-\gamma)a_n \right\} + \Delta t \gamma a_{n+1} \end{aligned} \tag{5.2}$$

where d is the vector of nodal displacements; v is the vector of nodal velocities; a is the vector of nodal accelerations; parameters γ and β define the variation of acceleration over a time step; Δt is the incremental time step; subscript n denotes the current time step.

In OSM, the displacement and velocity equations from the traditional Newmark integration scheme are split into predictor, which are explicit terms, and corrector responses. The predictor responses are:

$$\begin{aligned} \tilde{d}_{n+1} &= d_n + \Delta t v_n + \frac{\Delta t^2}{2}(1-2\beta)a_n \\ \tilde{v}_{n+1} &= v_n + \Delta t(1-\gamma)a_n \end{aligned} \tag{5.3}$$

The corrector responses are:

$$\begin{aligned} d_{n+1} &= \tilde{d}_{n+1} + \Delta t^2 \beta a_{n+1} \\ v_{n+1} &= \tilde{v}_{n+1} + \Delta t \gamma a_{n+1} \end{aligned} \tag{5.4}$$

The procedure for implementing OSM starts off by calculating the predictor responses using the response values from time step n. The predictor responses are then imposed on the tested structure, and the resulting restoring force $\tilde{r}_{n+1}$ is measured. The measured restoring force and the initial stiffness of the system are used to calculate the acceleration at time step n+1. After that, the corrector responses are obtained using the acceleration. The entire system behavior can be acquired by repeating the above procedure.

OSM is unconditionally stable when the initial stiffness of the tested structure is greater than the tangent stiffness during the entire test (Combescure and Pegon 1997). On the other hand, OSM becomes conditionally stable when it is applied to a system which shows stiffening behavior. The key limitation of the method is that when the tested system becomes inelastic, the primary assumption of OSM that the tangent stiffness of the system can be replaced by its initial stiffness breaks down. Under such conditions, the accuracy of the simulated response will be reduced (Combescure and Pegon 1997; Hung and El-Tawil 2009).

As outlined in Chapter 4, the use of a tangent stiffness matrix, as opposed to an initial stiffness matrix, is beneficial for highly nonlinear problems, enabling an accurate solution scheme without iterations. However, estimation of an accurate tangent stiffness matrix during testing is challenging. As a result, a method, which adopts not only a strategy for estimating a reasonably accurate stiffness matrix, but also an active self-correction to suppress errors resulting from inaccuracies in the estimated stiffness matrix, is desired. This chapter presents a new method, termed the Full Operator Method (FOM), for hybrid simulation that does that.

5.3 PROPOSED ALGORITHM FOR HYBRID TESTING

The equation of motion for the predictor step can be expressed as

$$M\hat{a}_{n+1} + C\hat{v}_{n+1} + \hat{r}_{n+1} = f_{n+1} \tag{5.5}$$

where $\hat{a}_{n+1}$ is the predictor acceleration vector; $\hat{v}_{n+1}$ is the predictor velocity vector; $\hat{r}_{n+1}$ is the predictor restoring force vector at time step n+1. Once the predictor acceleration vector is computed as discussed later on, the predictor velocity and displacement vectors can be obtained as

$$\begin{aligned}\hat{d}_{n+1} &= \left\{ d_n + \Delta t v_n + \frac{\Delta t^2}{2}(1-2\beta)a_n \right\} + \Delta t^2 \beta \hat{a}_{n+1} \\ \hat{v}_{n+1} &= \{ v_n + \Delta t(1-\gamma)a_n \} + \Delta t \gamma \hat{a}_{n+1}\end{aligned} \tag{5.6}$$

The predictor restoring force at time step n+1 can be approximated using the tangent stiffness as

$$\hat{r}_{n+1} \approx r_n + \hat{K}_{n+1}^T \left(\hat{d}_{n+1} - d_n \right) \tag{5.7}$$

where $\hat{K}_{n+1}^T$ is the estimated tangent stiffness at time step n+1, discussed later on in the chapter. Substituting Eqs. 5.6 and 5.7 into Eq. 5.5, the predictor acceleration at time step n+1 can be expressed as

$$\begin{aligned}\hat{a}_{n+1} &= \hat{M}_{n+1}^{-1} \hat{f}_{n+1} \\ \hat{M}_{n+1} &= M + \hat{C}_{n+1}\Delta t \gamma + \hat{K}_{n+1}^T \Delta t^2 \beta \\ \hat{f}_{n+1} &= f_{n+1} - \hat{C}_{n+1} v_n - \hat{C}_{n+1}\Delta t(1-\gamma)a_n - r_n - \hat{K}_{n+1}^T \left[\Delta t v_n + \frac{\Delta t^2}{2}(1-2\beta)a_n \right]\end{aligned} \tag{5.8}$$

where $\hat{M}_{n+1}$ is the predictor equivalent mass matrix; $\hat{C}_{n+1}$ is the predictor damping coefficient matrix, which is constant if it is mass-proportional or can be computed from $\hat{K}_{n+1}^{T}$ if stiffness proportional damping is assumed; $\hat{f}_{n+1}$ is the predictor equivalent force vector. Eq. 5.8 implies that $\hat{a}_{n+1}$ is a direct function of the estimated tangent stiffness $\hat{K}_{n+1}^{T}$. In a manner similar to Eq. 5.7, the restoring force relationship at time step n+1 is approximated as

$$r_{n+1} \approx \hat{r}_{n+1} + \hat{K}_{n+1}^{T}\left(d_{n+1} - \hat{d}_{n+1}\right) \tag{5.9}$$

From Eqs. 5.6 and 5.9, the difference between the corrector and predictor restoring forces can be expressed as

$$r_{n+1} - \hat{r}_{n+1} = \Delta t^{2} \beta \hat{K}_{n+1}^{T}\left(a_{n+1} - \hat{a}_{n+1}\right) \tag{5.10}$$

Eq. 5.10 contains 2nd order terms of the incremental time step. These terms are also a function of the difference between acceleration vectors, each of which contains small acceleration values. Therefore it is reasonable to assume that the difference between both vectors is negligibly small compared to either restoring force vector. In other words

$$r_{n+1} \approx \hat{r}_{n+1} \tag{5.11}$$

The numerical studies presented later on in the chapter confirm that Eq. 5.11 is an accurate assumption. An advantage of making the assumption in Eq. 5.11 is that it shields the solution from the uncertainty introduced by using the tangent stiffness in the corrector step.

The corrector acceleration is calculated by substituting Eqs. 5.2 and 5.11 into 5.1. The resulting solution can be expressed as

$$\begin{aligned} a_{n+1} &= M'^{-1}_{n+1} f'_{n+1} \\ M'_{n+1} &= M + C_{n+1}\Delta t\gamma \\ f'_{n+1} &= f_{n+1} - C_{n+1}v_n - C_{n+1}\Delta t(1-\gamma)a_n - r_{n+1} \end{aligned} \tag{5.12}$$

where M'_{n+1} is the corrector equivalent mass matrix; f'_{n+1} is the corrector equivalent force vector. C_{n+1} is the corrector damping coefficient matrix assumed to be equal to the predictor value, i.e. $C_{n+1} = \hat{C}_{n+1}$. Unlike the predictor acceleration, the corrector acceleration is not associated with the estimated tangent stiffness but is computed from the measured restoring force from the tested structure.

The procedure of the proposed method is illustrated in Fig. 5.1. First, the predictor displacement and velocity from Eq. 5.6 are calculated using the predictor acceleration from Eq. 5.8. The computed predictor displacement $\hat{d}_{n+1}$ and velocity $\hat{v}_{n+1}$ are imposed on the tested structure. The resulting restoring forces from the tested structure are then used in Eq. 5.12 to calculate the corrector acceleration, which is then substituted into Eq.

5.2 to generate the corrector displacement d_{n+1} and velocity v_{n+1}. Meanwhile, the new estimated tangent stiffness $\hat{K}^T$ for the next time step is computed using the measured increment in the predictor displacement $\Delta\hat{d}_n^m = \hat{d}_{n+1}^m - \hat{d}_n^m$ and restoring force vector $\Delta r_n = r_{n+1} - r_n$, as well as the current tangent stiffness; where $\hat{d}_{n+1}^m$ is defined as the measured predictor displacement $\hat{d}_{n+1}$. Since both predictor displacement and velocity are generated from the algorithm, an advantage of FOM is that it can be applied to real-time hybrid simulation.

The proposed FOM for hybrid simulation is viewed as an improvement over the regular OSM for two reasons. In the predictor step, the regular OSM, as shown in Eq. 5.3, neglects the implicit term a_{n+1} in the Newmark integration scheme. FOM increases the accuracy of the predictor by including this term and by relying on the estimated tangent stiffness as shown in Fig. 5.1. Second, the corrector acceleration in OSM is based on the estimated initial stiffness of the system, which adversely affects accuracy when the tested structure exhibits significant inelastic behavior. In contrast, FOM employs the measured restoring force from the tested structure, without resorting to approximations such as those used in OSM. These two points suggest that FOM is a better candidate for general hybrid simulation, as is demonstrated quantitatively later on in the chapter. Since computation of the tangent stiffness during testing is important to the success of the proposed methodology, various techniques for computing it are introduced next.

5.4 METHODS FOR ESTIMATING THE TANGENT STIFFNESS

Five different algorithms, including BFGS, DFP, Broyden, Broyden Family, and SR1, are used to estimate the tangent stiffness. The first method, the Broyden-Fletcher-Goldfarb-Shanno (BFGS) method, which is considered the most effective (Nocedal and Wright 1999) of all quasi-Newton updating formulae, is a method to solve for unconstrained nonlinear optimization problems. The BFGS formula for updating tangent stiffness is shown below (Nocedal and Wright 1999).

$$\hat{K}_{n+1}^{T} = \hat{K}_{n}^{T} + \frac{\Delta r_{n-1} \Delta r_{n-1}^{T}}{\Delta r_{n-1}^{T} \Delta \hat{d}_{n-1}^{m}} - \frac{\hat{K}_{n}^{T} \Delta \hat{d}_{n-1}^{m} \left(\hat{K}_{n}^{T} \Delta \hat{d}_{n-1}^{m} \right)^{T}}{\left(\Delta \hat{d}_{n-1}^{m} \right)^{T} \hat{K}_{n}^{T} \Delta \hat{d}_{n-1}^{m}} \tag{5.13}$$

where all the terms were previously defined. The Davidon-Fletcher-Powell formula (DFP) method is a quasi-Newton method that generalizes the secant method for multidimensional problems. The DFP formula for updating tangent stiffness is defined in Eq. 5.14. Although DFP has been largely abandoned by many current researchers in favor of the BFGS method, the DFP method is still nevertheless used in this study as one of the candidate methods for updating the tangent stiffness.

$$\hat{K}_{n+1}^{T} = \left(I - \frac{\Delta r_{n-1} \left(\Delta \hat{d}_{n-1}^{m} \right)^{T}}{\Delta r_{n-1}^{T} \Delta \hat{d}_{n-1}^{m}} \right) \hat{K}_{n}^{T} \left(I - \frac{\Delta \hat{d}_{n-1}^{m} \Delta r_{n-1}^{T}}{\Delta r_{n-1}^{T} \Delta \hat{d}_{n-1}^{m}} \right) + \frac{\Delta r_{n-1} \Delta r_{n-1}^{T}}{\Delta r_{n-1}^{T} \Delta \hat{d}_{n-1}^{m}} \tag{5.14}$$

Broyden's method, which was first documented by C. G. Broyden (Broyden 1965), is a quasi-Newton method for the numerical solution of nonlinear equations with multiple variables. When used for updating the tangent stiffness it can be expressed as

$$\hat{K}_{n+1}^{T} = \hat{K}_{n}^{T} + \frac{\left(\Delta r_{n-1} - \hat{K}_{n}^{T}\Delta\hat{d}_{n-1}^{m}\right)\left(\Delta\hat{d}_{n-1}^{m}\right)^{T}}{\left(\Delta\hat{d}_{n-1}^{m}\right)^{T}\Delta\hat{d}_{n-1}^{m}} \tag{5.15}$$

Broyden's family is a linear combination of BFGS and DFP with a parameter controlling the weighting of BFGS and DFP contributing to the final solution. In this method, the positive definiteness of the Hessian approximations is also enforced (Nocedal and Wright 1999). The Broyden's family algorithm used for estimating tangent stiffness is shown below, where the parameter ψ is between 0 and 1. ψ is chosen as 0.5.

$$\hat{K}_{n+1}^{T} = (1-\psi)\hat{K}_{n+1}^{T,BFGS} + \psi\hat{K}_{n+1}^{T,DFP}, \psi \in [0,1] \tag{5.16}$$

The formula for updating tangent stiffness using the SR1 method is given in Eq. 5.17. Unlike rank-two update methods (e.g. BFGS and DFP), the SR1 method does not

guarantee that the updated tangent stiffness will maintain positive-definiteness. There is evidence that SR1 often generates a better approximation than the BFGS method (Nocedal and Wright 1999).

$$\hat{K}_{n+1}^{T} = \hat{K}_{n}^{T} + \frac{\left(\Delta r_{n-1} - \hat{K}_{n}^{T}\Delta\hat{d}_{n-1}^{m}\right)\left(\Delta r_{n-1} - \hat{K}_{n}^{T}\Delta\hat{d}_{n-1}^{m}\right)^{T}}{\left(\Delta r_{n-1} - \hat{K}_{n}^{T}\Delta\hat{d}_{n-1}^{m}\right)^{T}\Delta\hat{d}_{n-1}^{m}} \tag{5.17}$$

In the following section, the effectiveness of the corrector step for suppressing inaccurate structural behavior resulting from an approximate or miscalculated tangent stiffness, i.e. as computed from one of the methods listed above, is numerically investigated.

5.5 PERFORMANCE OF THE FULL OPERATOR METHOD (FOM)

In order to investigate the performance of FOM, an undamped single DOF model with linear behavior is considered. In this numerical investigation, the external excitation is assumed to be zero. The system response is simulated using the proposed algorithm with an initial disturbance of a unit displacement. The estimated tangent stiffness is assumed to be $K_{est} = \lambda K_{real}$; where K_{est} and K_{real} are the estimated and real tangent stiffnesses of the model, respectively; λ is the stiffness ratio of the estimated tangent stiffness to the real tangent stiffness. The real tangent stiffness, K_{real}, of the model is assumed to be 1 lb/in.

The simulation procedure is illustrated in Fig. 5.2. The predictor displacement is first computed using the assumed estimated stiffness and is then imposed on the tested model. The resulting reaction force is calculated by multiplying the predictor displacement with the real stiffness. After that, the corrector displacement is generated using Eqs. 5.2 and 5.12. The model response to the initial disturbance is then acquired by repeating the above procedure. Since there is no external excitation except the initial disturbance, the system oscillating with a constant unit amplitude is the analytic response. In this investigation, the system is characterized by using a parameter Ω, defined as $\Omega = w_n \Delta t$, that accounts for the effect of step size and natural frequency on the solution; where w_n is the natural frequency of the system; Δt is the step size. Two different models with $\Omega =$ 0.02, and 0.1 are investigated. For each case, two different stiffness ratios, λ =0.1 and 10, are considered. The simulated responses using the proposed method with and without the corrector step are compared with the reference solution from the traditional Newmark method with the correct tangent stiffness. The parameters γ and β in the integration algorithm are chosen to be $\frac{1}{2}$ and $\frac{1}{4}$, respectively.

The computed solutions from the system with $\Omega =$ 0.02 are plotted in Fig. 5.3. It is observed from Fig. 5.3a that, when λ =0.1, the proposed method produces accurate results compared to the reference solution whether the scheme incorporates the corrector step or not. In Fig. 5.3b, where λ =10, it is seen that employing the corrector step generates a better result than when the corrector is not used. On the other hand, as Ω is increased to 0.1, the scheme without the corrector step loses its ability to track the

reference solution as shown in Fig. 5.4. However, in contrast, the scheme with the corrector is still able to generate a result coinciding with the reference solution.

Comparing Fig. 5.3 with Fig. 5.4, it is inferred that not using the corrector step produces results that are increasingly in error as Ω goes up. On the other hand, once the corrector step is employed, the displacement error is greatly diminished. Another observation is that for those results from the scheme without the corrector step, the oscillation amplitude becomes larger as time proceeds when the estimated tangent stiffness is less than the real tangent stiffness, whereas the amplitude diminishes with time when the stiffness ratio is larger than 1.

The cumulative energy error, E_c, computed for the response for the various systems is plotted in Figs. 5.5 and 5.6. It is clear from both Figs. 5.5 and 5.6 that E_c increases as Ω increases regardless of whether the corrector step is used or not. However, it can also be seen that deploying the corrector step significantly diminishes E_c suggesting that FOM can effectively maintain simulation accuracy even when the tangent stiffness is incorrectly estimated.

5.6 APPLICATION OF FOM TO NONLINEAR PROBLEMS

Two numerical examples are used to demonstrate the capabilities of the proposed method when applied to nonlinear structures. The 1940 El Centro earthquake history record, scaled such that PGA=1*g*, is used as seismic excitation for both examples. UI-SimCor (Kwon et al. 2008) is used as the platform for data transmission between the main

computer and the substructures, which are numerically modeled using OpenSees (OpenSees 2006). The simulated responses using the proposed algorithm are compared with reference solutions from numerical simulations of the entire systems in OpenSees. The parameters γ and β are chosen as $\frac{1}{2}$ and $\frac{1}{4}$, respectively. In order to show the effect of different schemes for estimating tangent stiffness on the model response, the tangent stiffness matrix is updated using the previously mentioned schemes, i.e. BFGS, DFP, Broyden, Broyden Family, and SR1.

Two rules recommended by Hung and El-Tawil (2009) are imposed on the algorithm to ensure reasonable results. The first resets the reloading/unloading tangent stiffness to the initial stiffness right after the point where the displacement direction changes. Although this rule limits the proposed validation study to structures dominated by first mode response, where unloading of one member is associated with unloading of the entire structure, it does not necessarily limit the applicability of FOM to structures dominated by first mode effects. The second rule is more practical in nature. It filters out the steps where the imposed displacements are smaller than a user-specified threshold, specified as a minimum incremental displacement. This is to ensure that only steps that are large enough to contribute reliably to the stiffness calculations are utilized in the computations. Although user experience clearly plays a role in identifying this parameter, a number that is 2-3 times the displacement resolution of the actuator is recommended.

The first example is a reinforced concrete shear wall model as shown in Fig. 5.7. The shear wall model is simulated as a 1 DOF structure with a mass of $2kips\frac{s^2}{in}$, and height of 15'. Cross section details are shown in Fig. 4.4. Concrete02 and Steel01 material models in OpenSees are used in the simulation and the associated parameter definitions are shown in Fig. 4.5 and Table 4.1. An incremental time step of $0.02\,\text{sec}$ is used for this example. To study the operation of FOM in detail and understand how its various components contribute to a successful solution, the following 4 schemes are simulated: 1) FOM with initial stiffness and without the corrector step; 2) FOM with initial stiffness and with the corrector step; 3) FOM with updated tangent stiffness and without the corrector step, and 4) FOM with updated tangent stiffness and corrector step, i.e. the full capability of FOM.

The simulation result from the 1st scheme is shown in Fig. 5.8a. It is clear that the resulting simulated behavior diverges from the reference solution when the corrector step and the updated tangent stiffness are not used. On the other hand, the solution improves greatly when the other 3 schemes are employed as can be seen in Fig. 5.8b. Although the figure only shows results from the BFGS updating method, equally good results are obtained when the other 4 updating methods are used. These are not shown so not to clutter up the figure.

The influence of the various parts of FOM can be seen in Fig. 5.9, which plots E_c (on a log scale) computed from the 4 different schemes. Clearly, and as was obvious in Fig. 5.8a, using only the initial stiffness without the corrector step produces simulation errors

that are much larger than those produced by the other 3 schemes. Using only the tangent stiffness matrix (without a corrector step) reduces E_c by approximately an order of magnitude, while incorporating the corrector step in both cases dramatically reduces E_c. Using a tangent stiffness with a corrector step, which is the case when FOM is fully implemented, is the best situation. Fig. 5.9 also demonstrates the advantage of FOM over OSM. In particular, OSM accumulates errors that are two orders of magnitude greater than the full implementation of FOM for this particular problem (Fig. 5.9a). The superiority of FOM over OSM can also be seen in Fig. 5.9b, which shows that FOM traces the reference solution very well, while OSM deviates from it, especially at the peak points.

The second example is a 6-story shear model with the cross section details shown in Fig. 4.4. The values of the concentrated mass blocks and heights for each floor are displayed in Fig. 5.10. For hybrid simulation purposes, the building is broken up into 2 parts, the first floor serves as the 1st substructure and the remaining portion as the 2nd substructure. The entire building is also simulated in OpenSees to provide a reference solution. An incremental time step of $0.005\,\mathrm{sec}$ is chosen for this example.

The same 4 schemes employed in the single-DOF cantilever example above are used in this example as well to show the effect of the various parts and assumptions of FOM. In addition, since all the tangent stiffness updating methods gave close results, only the results from the BFGS method are presented. Fig. 5.11a shows the result from the 1st scheme in which the initial stiffness is used but not the corrector step. Clearly, the

solution diverges from the reference solution. The simulation results from the other 3 schemes are plotted in Fig. 5.11b, which shows that the simulated seismic responses from these 3 schemes match the reference solution better than the one in Fig. 5.11a. However, zooming in on the plot (not shown) shows that there are differences, which can be seen by computing the cumulative energy error, E_c. The value of E_c associated with the first-floor displacement is calculated and plotted in Fig. 5.12. As noted in the single-DOF cantilever example, the use of the tangent stiffness alone or initial stiffness with corrector both improve the simulation accuracy compared to just using the initial stiffness; in particular, E_c is more than an order of magnitude less in the case when the initial stiffness with corrector is used. As alluded to previously in Fig. 5.9, Fig. 5.12 shows that full implementation of FOM (with tangent stiffness and corrector) results in significantly less errors than application of the traditional OSM.

5.7 HANDLING DISPLACEMENT CONTROL ERRORS IN FOM

Displacement control errors in hydraulic actuators can greatly affect simulation accuracy during hybrid testing. The I-modification technique (Nakashima and Kato 1987) was proposed as a means to suppress the adverse effects of displacement control errors when the OSM method is used. However, it has been shown in (Combescure and Pegon 1997) that when the OSM with I-modification is used to simulate structural behavior with significant inelastic behavior, the resulting simulated displacements may suffer in accuracy.

The effect of displacement control errors on the performance of the proposed algorithm is studied using the 6-story shear model. A constant overshoot displacement control error of 0.001 in is assumed in the simulations. Results from FOM are compared to those from OSM with I-modification in Fig. 5.13 to show the benefits of using the new method. It can be seen from the figure that OSM with I-modification deviates from the reference solution from OpenSees. On the other hand, the proposed method is still able to achieve good performance. This is attributed to the fact that the corrector in the proposed method relies entirely on measured information from the tested structures, i.e. the restoring force, instead of using an estimated initial stiffness or tangent stiffness of the structure in the case of OSM.

5.8 STABILITY CHARACTERISTIC OF FOM

To investigate the stability of FOM, an elastic, undamped single degree of freedom system is considered. The equations of motion of FOM for the predictor and corrector steps, respectively, at time step n+1 can be written as:

$$M\hat{a}_{n+1} + \left[K^{EST}(\hat{d}_{n+1} - d_n) + r_n\right] = f_{n+1} \tag{5.18}$$

$$Ma_{n+1} + r_{n+1} = f_{n+1} \tag{5.19}$$

where $\hat{d}_{n+1} = \left\{ d_n + \Delta t v_n + \frac{\Delta t^2}{2}(1-2\beta)a_n \right\} + \Delta t^2 \beta \hat{a}_{n+1}$; $r_{n+1} = \hat{r}_{n+1} = K^R(\hat{d}_{n+1})$, which is a key assumption in FOM, as previously discussed; K^{EST} and K^R are the estimated and

real tangent stiffnesses, respectively. Rearranging Eqs. 5.4, 5.18 and 5.19 with $\gamma = \frac{1}{2}$ and $\beta = \frac{1}{4}$, the free vibration solution for FOM can be written in a recursive form as

$$X_{n+1} = AX_n \tag{5.20}$$

where $X_n = \begin{Bmatrix} d_n \\ v_n \Delta t \\ a_n \Delta t^2 \\ \hat{d}_n \end{Bmatrix}$;

$A = \begin{bmatrix} 1-\frac{\Omega^2}{4} & 1-\frac{1}{4}\left(\Omega^2 - \frac{\alpha\Omega^4}{\left(4+\alpha\Omega^2\right)}\right) & \frac{1}{4}-\frac{1}{16}\left(\Omega^2 - \frac{\alpha\Omega^4}{\left(4+\alpha\Omega^2\right)}\right) & \frac{1}{4}\frac{\Omega^4}{\left(4+\alpha\Omega^2\right)} \\ -\frac{\Omega^2}{2} & 1-\frac{1}{2}\left(\Omega^2 - \frac{\alpha\Omega^4}{\left(4+\alpha\Omega^2\right)}\right) & \frac{1}{2}-\frac{1}{8}\left(\Omega^2 - \frac{\alpha\Omega^4}{\left(4+\alpha\Omega^2\right)}\right) & \frac{1}{2}\frac{\Omega^4}{\left(4+\alpha\Omega^2\right)} \\ -\Omega^2 & -\Omega^2 + \frac{\alpha\Omega^4}{\left(4+\alpha\Omega^2\right)} & -\frac{\Omega^2}{4}+\frac{1}{4}\frac{\alpha\Omega^4}{\left(4+\alpha\Omega^2\right)} & \frac{\Omega^4}{\left(4+\alpha\Omega^2\right)} \\ 1 & 1-\frac{\alpha\Omega^2}{\left(4+\alpha\Omega^2\right)} & \frac{1}{4}-\frac{1}{4}\frac{\alpha\Omega^2}{\left(4+\alpha\Omega^2\right)} & \frac{-\Omega^2}{\left(4+\alpha\Omega^2\right)} \end{bmatrix}$, is the amplification matrix; $\Omega = \omega\Delta t = \sqrt{\frac{K^R}{M}}\Delta t$, is the sampling frequency. α is defined as the estimation error of the tangent stiffness and is expressed as $\alpha = \frac{K^{EST}}{K^R}$.

The stability of FOM can be investigated using the spectral radius of the amplification matrix A (Hilber et al. 1977; Hung and El-Tawil 2009a). The spectral radius, $\rho(A)$, is the maximum absolute eigenvalue of the amplification matrix. An algorithm is stable when its spectral radius is less than or equal to 1. The spectral radius of FOM's amplification matrix versus Ω with varying α is plotted in Fig. 5.14. It can be seen that

FOM is a conditionally stable algorithm. The stability criterion for FOM becomes more stringent as the accuracy of the estimated tangent stiffness decreases. In particular, when $\alpha = 1$, FOM is stable if $\Omega \leq 2$, which is the same stability criterion of the central difference method (Chopra 2006).

5.9 ENHANCING THE NUMERICAL CHARACTERISTICS OF FOM

5.9.1 Modified FOM (mFOM)

The response of structures with higher mode response is challenging to simulate using conditionally stable algorithms. The short period associated with the highest mode controls the simulation by imposing strict limits on the size of the time step. Small incremental time steps not only increase the total simulation time but also magnify the adverse effect of actuator control errors on simulation accuracy.

In order to enhance the stability characteristics of FOM for structures showing higher mode response, a new version of FOM is proposed, termed modified-FOM, or mFOM. As discussed previously (Hung and El-Tawil 2009b), the restoring force relationship at time step n+1 can be approximated as

$$r_{n+1} - \hat{r}_{n+1} \approx \hat{K}_{n+1}^{T}\left(d_{n+1} - \hat{d}_{n+1}\right) \tag{5.21}$$

The corrector restoring force in FOM is assumed equal to the predictor restoring force, i.e. $r_{n+1} \approx \hat{r}_{n+1}$. This assumption was justified (Hung and El-Tawil 2009b) based on the argument that the incremental force in Eq. 5.21 is associated with a 2nd order term minor enough to ignore. This assumption is, however, the main reason that FOM is

conditionally stable, and when the expression in Eq. 5.21 is used instead of the approximation that $r_{n+1} \approx \hat{r}_{n+1}$, a new version of FOM with enhanced stability characteristics is obtained.

Substituting Eq. 5.21 into the equation of motion at the corrector step at time step n+1:

$$Ma_{n+1} + C_{n+1}v_{n+1} + \left[\hat{r}_{n+1} + \hat{K}_{n+1}^{T}\left(d_{n+1} - \hat{d}_{n+1}\right)\right] = f_{n+1} \tag{5.22}$$

Rearranging Eq. 5.22, the corrector acceleration for mFOM can be calculated as:

$$\begin{aligned} a_{n+1} &= {M'_{n+1}}^{-1} f'_{n+1} \\ M'_{n+1} &= M + C_{n+1}\Delta t\gamma + \hat{K}_{n+1}^{T}\Delta t^2\beta \\ f'_{n+1} &= f_{n+1} - C_{n+1}v_n - C_{n+1}\Delta t(1-\gamma)a_n - \hat{r}_{n+1} + \hat{K}_{n+1}^{T}\Delta t^2\beta\hat{a}_{n+1} \end{aligned} \tag{5.23}$$

where M'_{n+1} is the corrector equivalent mass matrix of mFOM; f'_{n+1} is the corrector equivalent force vector of mFOM. While it appears small, this modification has a large impact on the stability characteristics of mFOM as outlined next.

5.9.2 Stability characteristic of mFOM

The stability and accuracy characteristics of mFOM are investigated in this section with particular emphasis on the effect of the estimated tangent stiffness and damping coefficient. In the predictor step of mFOM, the equation of motion for an elastic, damped single degree of freedom system under free vibration can be written as

$$M\hat{a}_{n+1} + \left[C^{EST}(\hat{v}_{n+1} - v_n) + \left(f_d\right)_n\right] + \left[K^{EST}(\hat{d}_{n+1} - d_n) + r_n\right] = 0 \tag{5.24}$$

where

$\left(f_d\right)_n = C^R(\hat{v}_n) + C^{EST}(v_n - \hat{v}_n)$;

$r_n = K^R(\hat{d}_n) + K^{EST}(d_n - \hat{d}_n)$;

C^{EST} and C^R are the estimated and real damping coefficients, respectively.

The equation of motion for the corrector at the same time step can be expressed as

$$Ma_{n+1} + \left[C^{EST}(v_{n+1} - \hat{v}_{n+1}) + C^R(\hat{v}_{n+1})\right] + \left[K^{EST}(d_{n+1} - \hat{d}_{n+1}) + K^R(\hat{d}_{n+1})\right] = 0 \tag{5.25}$$

The response solution can be obtained in a recursive form using Eq. 5.24 and Eq. 5.25 and applying $\gamma = \frac{1}{2}$ and $\beta = \frac{1}{4}$, i.e.:

$$X'_{n+1} = A'X'_n \tag{5.26}$$

where $X'_n = \begin{Bmatrix} d_n \\ v_n\Delta t \\ a_n\Delta t^2 \\ \hat{d}_n \end{Bmatrix}$;

$$A' = \begin{bmatrix} 1-\frac{\Omega^2}{P}\left(1+\frac{Q}{P}\right)-\left(\frac{Q}{P}\right)^2 & 1-\frac{-2\xi\Omega-\Omega^2}{P}+\frac{-2\xi\Omega-\alpha\Omega^2}{P}\left(\frac{Q}{P}\right) & \frac{1}{4}\left[1+\frac{-4\xi\Omega-\Omega^2}{P}+\frac{SQ}{P^2}+\left(\frac{Q}{P}\right)^2\right] & \left(\frac{Q}{P}\right)^2 \\ -2\left[\frac{\Omega^2}{P}\left(1+\frac{Q}{P}\right)+\left(\frac{Q}{P}\right)^2\right] & 1-\frac{-4\xi\Omega-2\Omega^2}{P}+\frac{-4\xi\Omega-2\alpha\Omega^2}{P}\left(\frac{Q}{P}\right) & \frac{1}{2}\left[1+\frac{-4\xi\Omega-\Omega^2}{P}+\frac{SQ}{P^2}+\left(\frac{Q}{P}\right)^2\right] & 2\left(\frac{Q}{P}\right)^2 \\ -4\left[\frac{\Omega^2}{P}\left(1+\frac{Q}{P}\right)+\left(\frac{Q}{P}\right)^2\right] & \frac{-8\xi\Omega-4\Omega^2}{P}+\frac{-8\xi\Omega-4\alpha\Omega^2}{P}\left(\frac{Q}{P}\right) & \frac{-4\xi\Omega-\Omega^2}{P}+\frac{SQ}{P^2}+\left(\frac{Q}{P}\right)^2 & 4\left(\frac{Q}{P}\right)^2 \\ 1-\frac{Q+\Omega^2}{P} & 1+\frac{-2\xi\Omega-\alpha\Omega^2}{P} & 1+\frac{S+Q}{P} & \frac{Q}{P} \end{bmatrix};$$

$; P = 4+4\beta\xi\Omega+\alpha\Omega^2;\ Q = 4\xi\Omega(\beta-1)+\Omega^2(\alpha-1);\ S = 4\xi\Omega(1-2\beta)+\Omega^2(1-2\alpha);$

$\xi = \frac{C^R}{2M\omega};\ \Omega = \omega\Delta t = \sqrt{\frac{K^R}{M}}\Delta t$. β is defined as the estimation error of the damping coefficient and is expressed as $\beta = \frac{C^{EST}}{C^R}$.

When $\xi = 0.05$ and β =1, the spectral radius versus Ω with varying α is plotted in Fig. 5.15. As shown in Fig. 5.15a, mFOM is unconditionally stable when $\alpha \geq 1$. When $\alpha < 1$, mFOM becomes conditionally stable as can be seen from Fig. 5.15b. Compared to the original FOM, which was conditionally stabile, the stability of mFOM is guaranteed when the estimated tangent stiffness is larger than or equal to the true stiffness of the structure. This implies that when the tangent stiffness of the structure is difficult to estimate, the initial tangent stiffness can be used with mFOM to achieve unconditional stability. This is true as long as the structure's stiffness degrades with testing, which is a common situation in most civil structures. The effect on the simulation accuracy of replacing the tangent stiffness with the initial stiffness is discussed in the next section using a numerical example.

The numerical accuracy of mFOM can be investigated using the ratio of period distortion and numerical damping (Wu et al. 2005; Shing and Mahin 1985; Hung and El-Tawil 2009a). Among the 4 eigenvalues of the amplification matrix A', 2 are complex numbers, 1 is a real number, and 1 equals zero. The displacement response for a viscously underdamped free-vibration response can be expressed using eigenvalues as (Wu et al. 2005; Hung and El-Tawil 2009a)

$$d_n = \exp(-\xi'\overline{\omega}_n n\Delta t)\left[c_1 \cos(\overline{\omega}_d n\Delta t) + c_2 \sin(\overline{\omega}_d n\Delta t)\right] + c_3\lambda_3^n \tag{5.27}$$

where the complex eigenvalues $\lambda_{1,2} = \exp\left[\left(-\hat{\xi} \pm i\right)\overline{\Omega}\right] = L_1 \pm iL_2$; λ_3 is a real value; $\hat{\xi} = -\dfrac{\ln(L_1^2 + L_2^2)}{2\overline{\Omega}}$; $\overline{\Omega} = \tan^{-1}\left(\dfrac{L_2}{L_1}\right)$; $\xi' = \dfrac{\hat{\xi}}{\sqrt{1+\hat{\xi}^2}}$; $\overline{\omega}_d = \dfrac{\overline{\Omega}}{\Delta t}$; $\overline{\omega}_n = \dfrac{\overline{\omega}_d}{\sqrt{1-\xi^2}}$. The numerical damping is defined as

$$\overline{\xi} = \xi' - \xi \tag{5.28}$$

The variation of numerical damping ratio against Ω with varying α when $\xi = 0.05$ and $\beta = 1$is plotted in Fig. 5.16. As shown in Fig. 5.16a, when $\alpha \geq 1$, the absolute value of the maximum numerical damping ratio increases with increasing α. As Ω increases, the numerical damping ratio converges to a constant around -0.1. The numerical damping ratio versus Ω when$\alpha < 1$is depicted in Fig. 5.16b. The figure shows the absolute value of the maximum numerical damping ratio increases as the estimated tangent stiffness becomes less accurate. The value of numerical damping ratio also converges to a constant

for each α. However, the absolute value to which the damping ratio converges is larger compared to the case where $\alpha > 1$.

The effect of the accuracy of the estimated damping coefficient on the numerical damping ratio is plotted in Fig. 5.17 for $\xi = 0.05$ and $\alpha = 1$. The figure shows that the absolute value of the numerical damping ratio increases with increasing β; however, the influence of β is less than that of α on the numerical damping ratio.

In addition to the numerical damping ratio, period distortion is used as an indication of mFOM's accuracy. Period distortion is defined as (Wu et al. 2005; Shing and Mahin 1985; Hung and El-Tawil 2009a)

$$\frac{\Delta T_d}{T_d} = \frac{\overline{T}_d - T_d}{T_d} = \frac{\omega_d}{\overline{\omega}_d} - 1 = \frac{\Omega}{\overline{\Omega}}\sqrt{1-\xi^2} - 1 \tag{5.29}$$

The relationship between period distortion and Ω for $\alpha \geq 1$ is plotted in Fig. 5.18a for the case where $\beta = 1$ and $\xi = 0.05$. The result indicates that for $\alpha > 1$ the period decreases as the accuracy of estimated tangent stiffness decreases whereas the period elongates for $\alpha \leq 1$ as shown in Fig. 5.18b. The influence of β on the period is plotted in Fig. 5.19, which implies that the period elongates as β increases.

5.9.3 Hybrid simulation of a 6-story model using mFOM

A 6-story shear model is used to demonstrate the performance of mFOM for hybrid simulation. The values of the concentrated mass blocks and heights for each floor are displayed in Fig. 5.10. As shown in Fig. 5.10, the bottom floor is chosen to serve as the 1st substructure, while the rest of the structure serves as the 2nd substructure. Both substructures are numerically simulated in OpenSees (2006). Cross section details are shown in Fig. 4.4. The displacement-based beam column element in OpenSees (2006), which allows distributed plasticity with linear curvature distribution along the element, is chosen to simulate the model. Concrete02 and Steel01 material models in OpenSees (2006) are used in the simulation and the associated parameter definitions are shown in Fig. 4.5 and Table 4.1.

The response of the system to the 1940 El Centro earthquake is simulated using four different approaches, including mFOM with updated tangent stiffness, mFOM with initial structural stiffness, OSM, and the conventional numerical method, which is used as the reference solution. An incremental time step of $0.005\,\text{sec}$ is used for all the schemes. UI-SimCor (Kwon et al. 2008) is used as the hybrid simulation platform. In order to show that mFOM is capable of simulating structures with significant nonlinear behavior, the earthquake history record is scaled such that the peak ground acceleration is $1g$. The parameters γ and β in mFOM are chosen as $\frac{1}{2}$ and $\frac{1}{4}$, respectively. The tangent stiffness matrix is updated using the BFGS method (Hung and El-Tawil 2009b).

The displacement history responses of the 1st floor associated with the various solution schemes are plotted in Fig. 5.20a. The figure shows that the responses computed from all

methods match the reference solution well. However, there are some differences between the various schemes, which can be seen more clearly in the magnified view shown in Fig. 5.20b. The figure indicates that while the solution from mFOM with updated tangent stiffness very closely matches the reference solution, the solutions from OSM and mFOM with initial structural stiffness deviate somewhat from the reference solution.

The differences in performance of the various schemes can be better appreciated using the cumulative energy error index (CEEI) (Hung and El-Tawil 2009b). In addition to the previously mentioned schemes, the performance of the regular FOM, which also matched the reference solution very closely, is also included in the discussion.

The resulting CEEI from each scheme (associated with the 1^{st} floor) is plotted in Fig. 5.21. The figure indicates that mFOM with initial structural stiffness results in a solution with error propagation characteristics similar to OSM. This suggests that mFOM with initial stiffness is at least as good as OSM, which also employs the initial stiffness in its calculations. Another observation from Fig. 5.21 is that mFOM with updated tangent stiffness and the regular FOM have similar CEEI values. At the end of the simulation, both schemes generate CEEI values that are less than 10% of that for OSM. Overall, the simulation results indicate that both versions of mFOM are capable of producing reasonable solutions, although the version with tangent stiffness is more accurate than the one employing initial stiffness. This is, however, not surprising, since it is well known that the use of the tangent stiffness instead of the initial stiffness improves the accuracy of predictor-corrector schemes such as mFOM (Hung and El-Tawil 2009a).

5.10 SUMMARY

A new hybrid simulation technique was presented in this chapter. The technique, termed Full Operator Method, or FOM, differs in two significant ways from the commonly used OSM. First, FOM increases the accuracy of the predictor step by including a predictor acceleration term and by relying on the tested structure's estimated tangent stiffness. Second, FOM employs the measured restoring force from the tested structure for the corrector step, without resorting to approximations such as those used in OSM. Based on the advantages of the method, it is suggested that FOM is a better candidate for general hybrid simulation than the Operator-Splitting Method and other similar techniques. Furthermore, since both predictor displacement and velocity are generated from the algorithm, FOM can be applied to real-time hybrid simulation. The capabilities of FOM were demonstrated through a number of numerical simulations, including an elastic SDOF vibrator, an inelastic single-DOF shear wall system, and an inelastic 6-story shear structure. A final exercise showed that FOM can also be used to generate good results even when displacement control errors are present.

The stability of the Full Operator Method (FOM) was then formally investigated. By examining the spectral radius of FOM's characteristic matrix, the technique was found to be conditionally stable. It was found that when the estimated tangent stiffness is equal to the actual structural stiffness, the required sampling frequency for FOM necessary to achieve stability is equal to that for the central difference method. A modified version of FOM, termed mFOM, which accounts for the incremental restoring force between the

predictor and corrector steps, was proposed. The stability and accuracy characteristics of mFOM were then investigated and it was found that mFOM is unconditionally stable when the estimated tangent stiffness of the structure is larger than or equal to the actual stiffness of the structure. mFOM is therefore unconditionally stable when the initial stiffness is employed during hybrid testing of structures in which the stiffness characteristics degrade with loading. The effect of inaccurately estimating the tangent stiffness and damping coefficient on the stability and accuracy of mFOM was discussed in terms of period distortion and numerical damping. The performance of mFOM for hybrid testing was also demonstrated using a 6-story numerical model. The simulation results indicated that the two variations of mFOM considered were able to predict the seismic response of the model with reasonable accuracy.

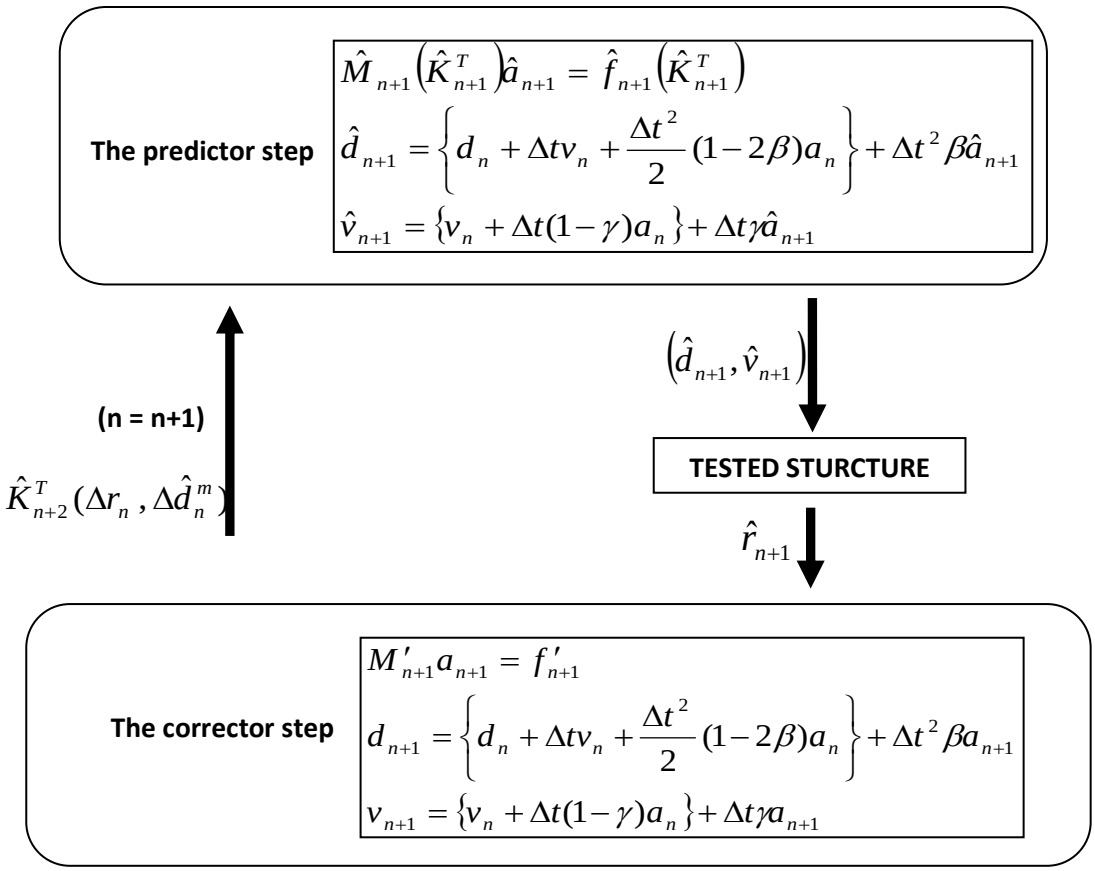

Fig 5.1 - Algorithm for the proposed method

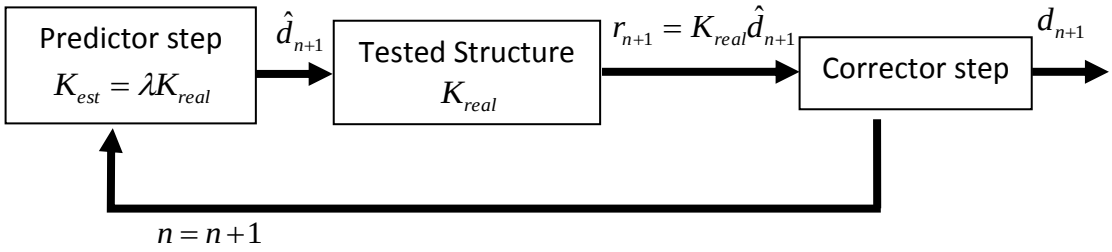

Fig 5.2 - Procedure for investigation of the influence of the corrector step on the simulated solution

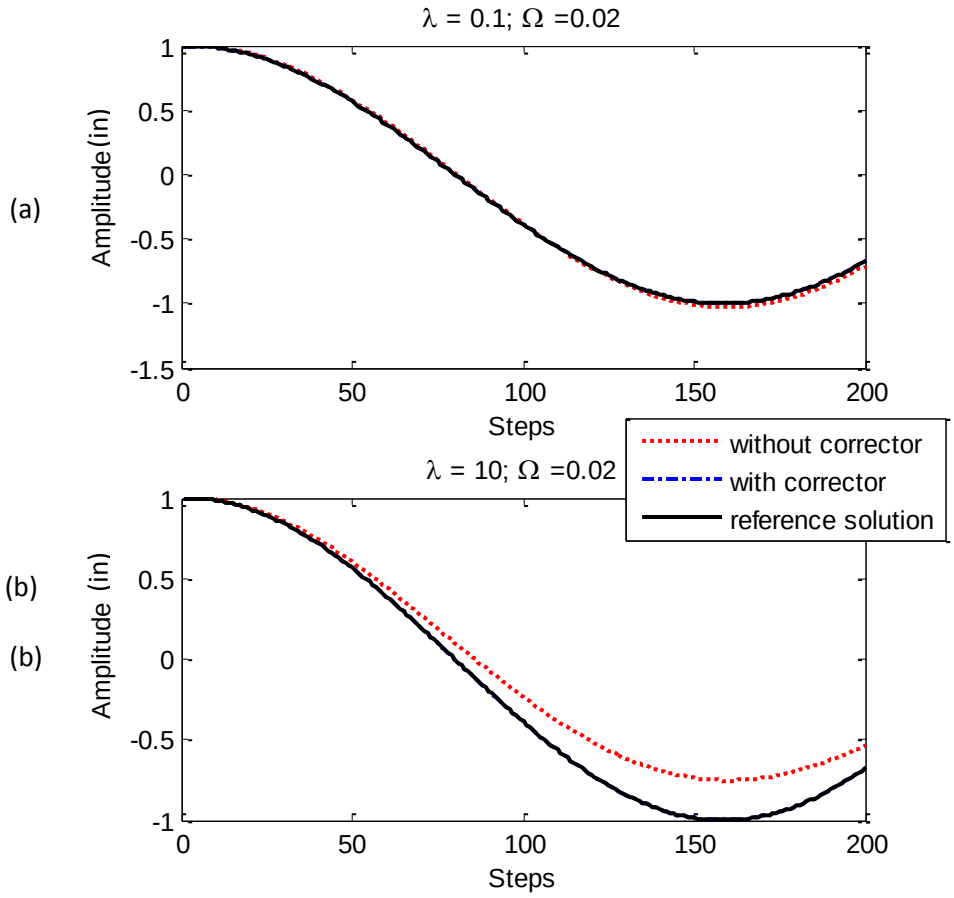

(a)

(b)

Fig 5.3. - Model response with $\Omega = 0.02$ using different stiffness ratios: (a) $\lambda = 0.1$ and (b) $\lambda = 10$

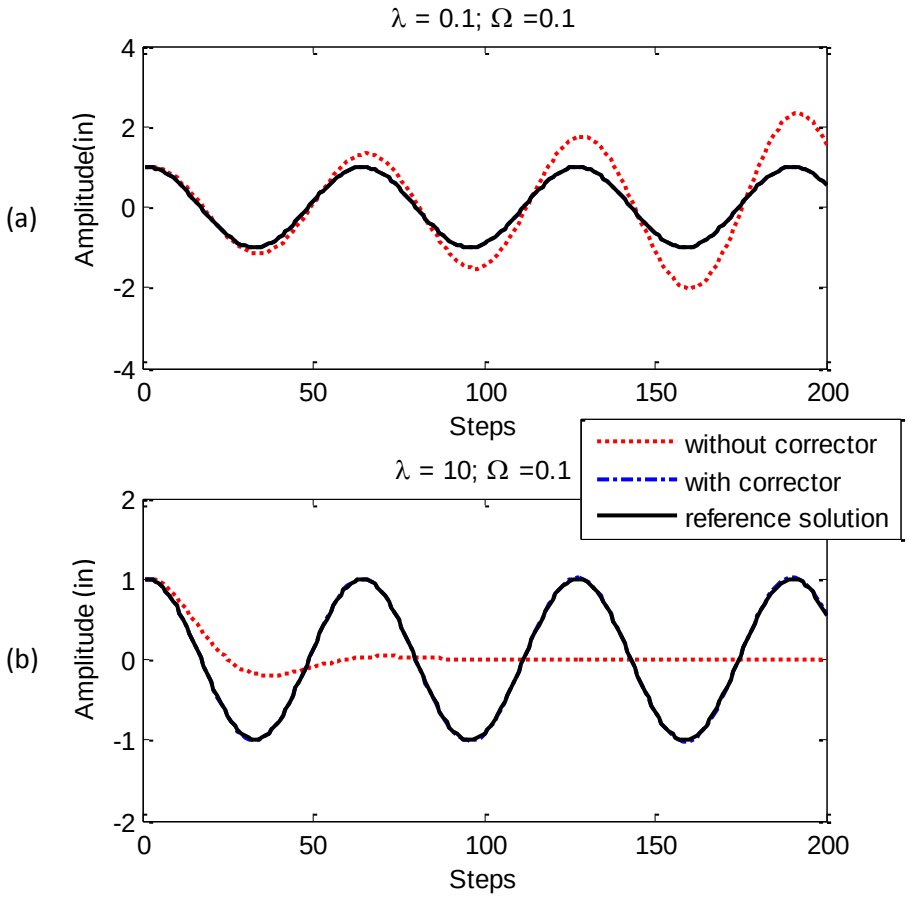

Fig 5.4 - Model response with $\Omega = 0.1$ using different stiffness ratios: (a) $\lambda = 0.1$ and (b) $\lambda = 10$

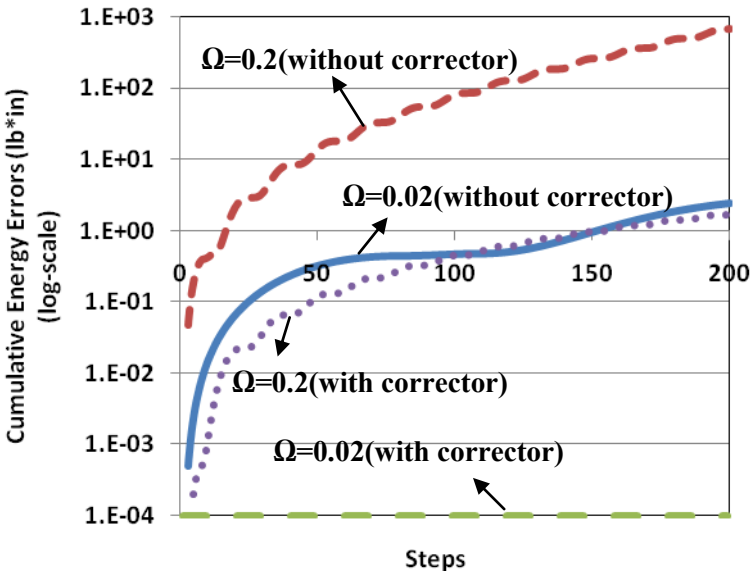

Fig 5.5 - Displacement errors with and without the corrector step when $\lambda = 0.1$

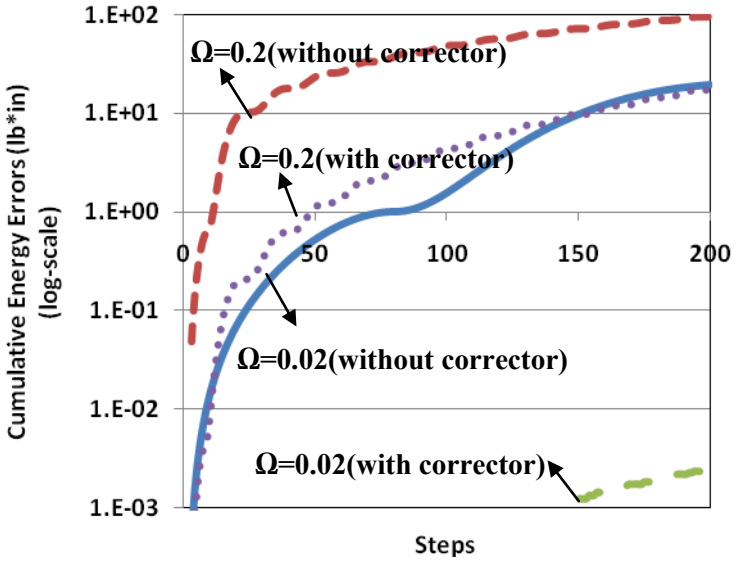

Fig 5.6 - Displacement errors with and without the corrector step when $\lambda = 10$

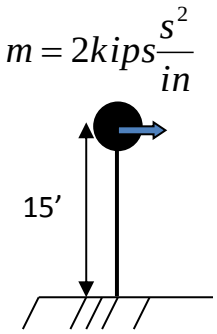

Fig 5.7 - Properties of the shear wall model

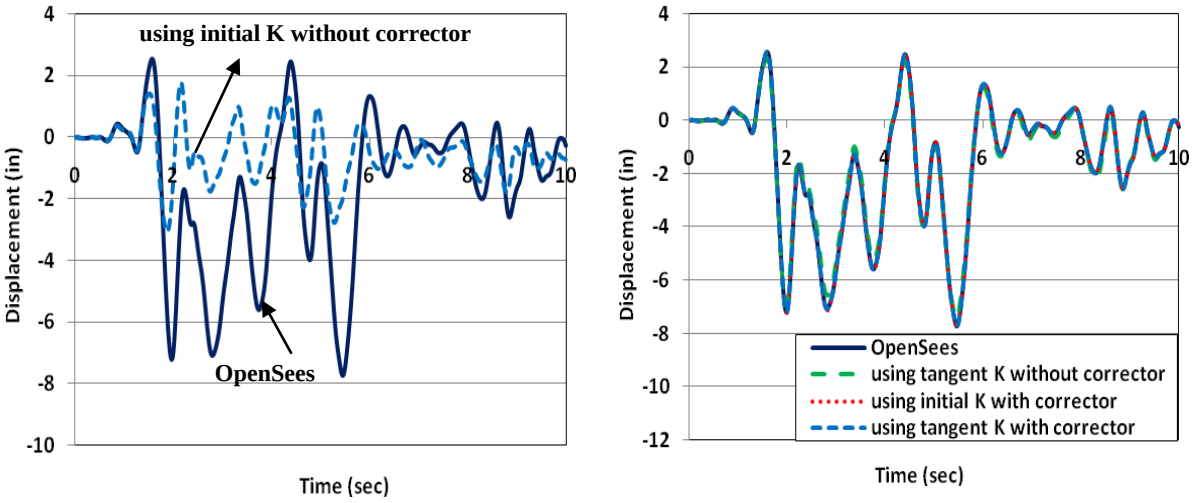

(a) Initial stiffness without the corrector step (b) Results from various FOM schemes

Fig 5.8 - Simulated seismic responses of the shear wall model

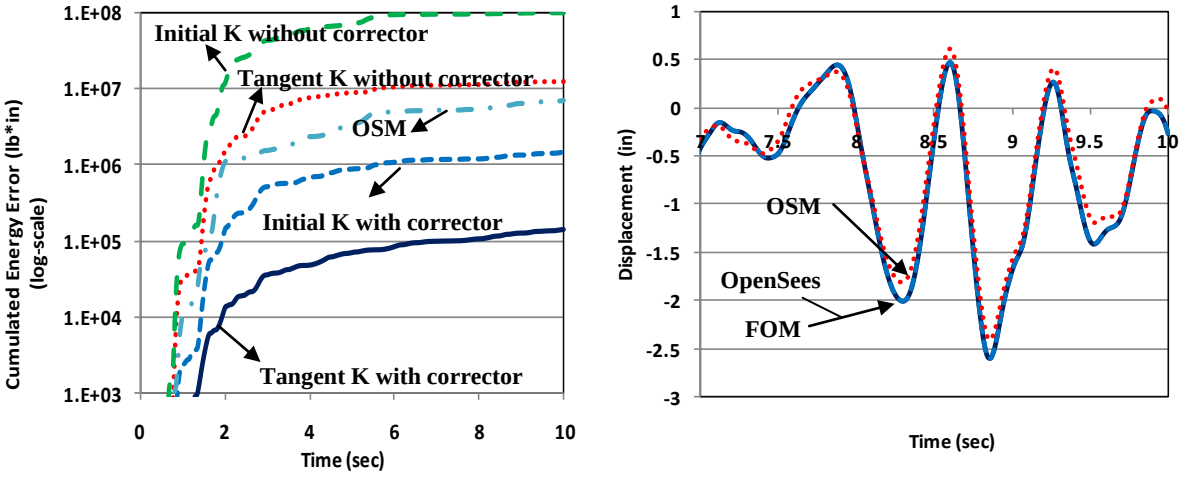

(a) Cumulated energy error, E_c (b) Solutions from OpenSees, FOM and OSM

Fig 5.9 - Comparison of shear wall model results computed from various schemes

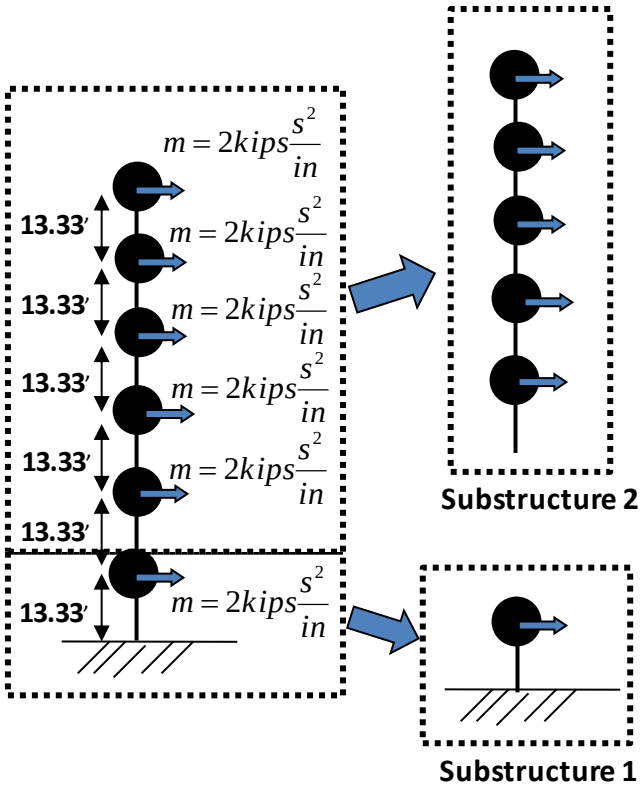

Fig 5.10 - Details of the 6-story model

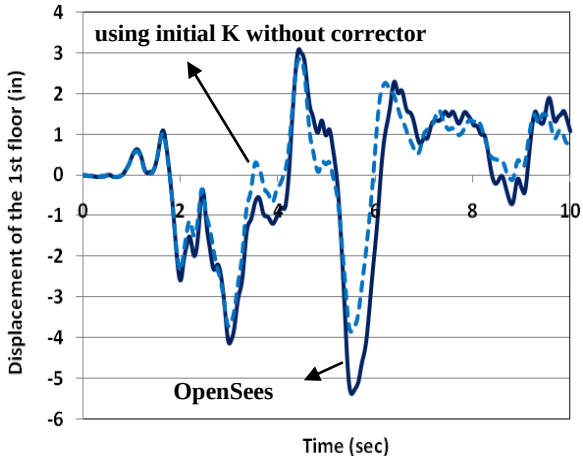

(a) Initial stiffness without the corrector step

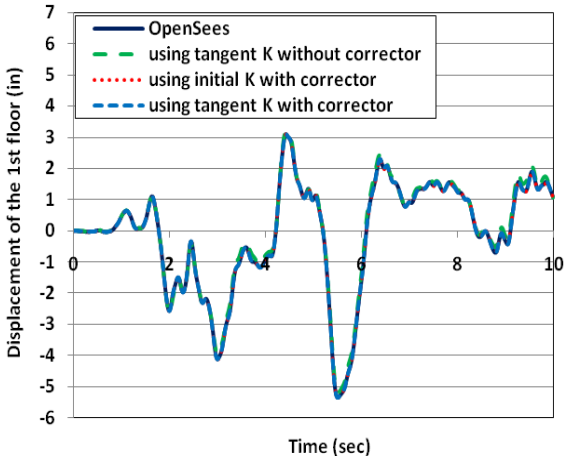

(b) Results from various FOM schemes

Fig 5.11 - Simulated seismic response of the 6-story model

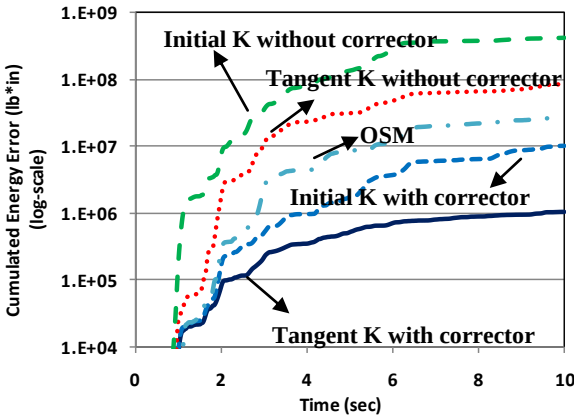

(a) Cumulated energy error, E_c

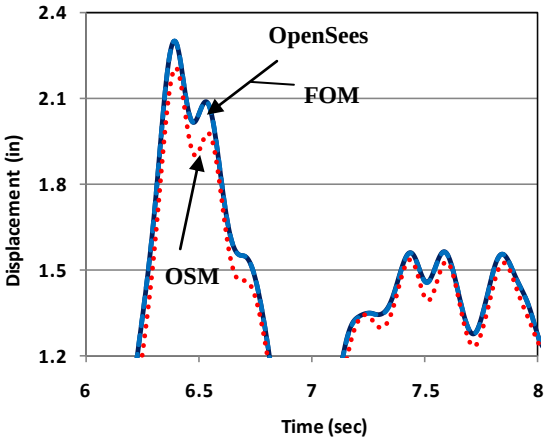

(b) Solutions from OpenSees, FOM and OSM

Fig 5.12 - Comparison of 6-story model results computed from various schemes

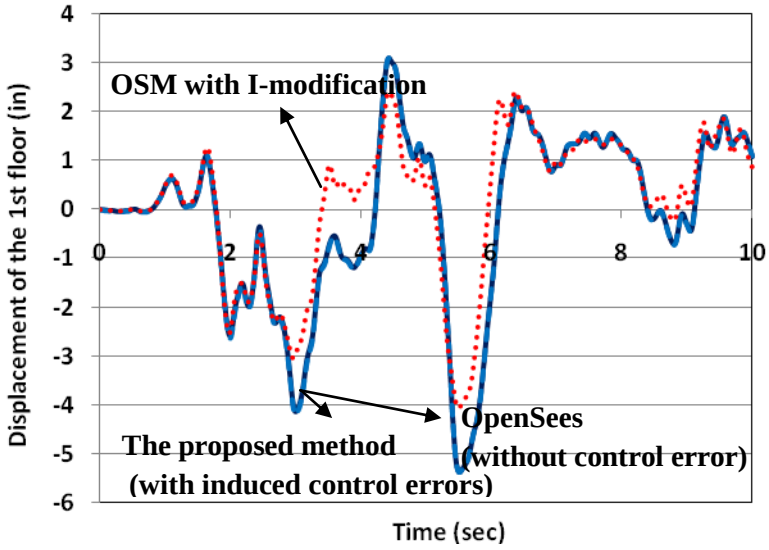

Fig 5.13 - The effect of displacement control error on simulation results

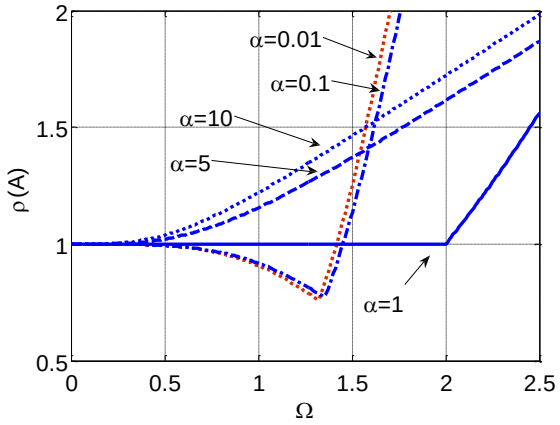

Fig. 5.14 - Relationship between spectral radius and Ω with varying α for FOM

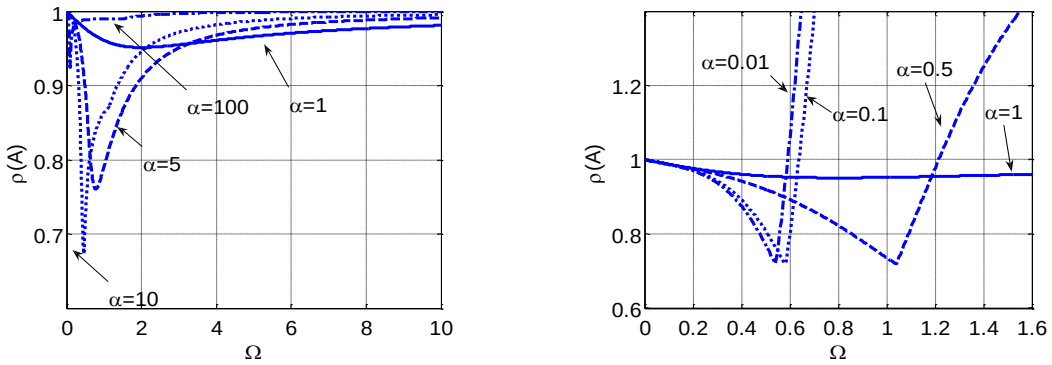

(a) $\alpha \geq 1$ (b) $\alpha \leq 1$

Fig. 5.15 - Relationship between spectral radius and Ω with varying α for mFOM

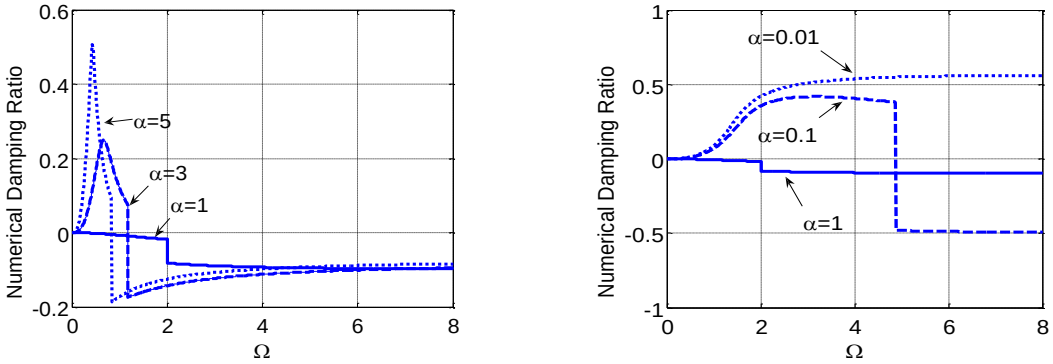

(a) $\alpha \geq 1$ (b) $\alpha \leq 1$

Fig. 5.16 - Relationship between numerical damping ratio and Ω with varying α for mFOM

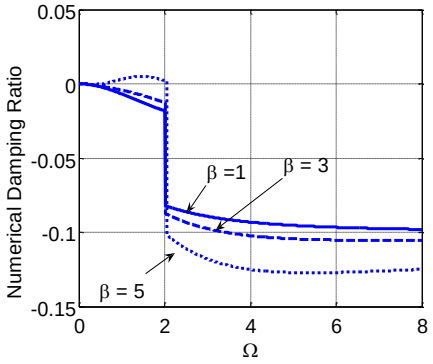

Fig. 5.17 - Relationship between numerical damping ratio and Ω with varying β for mFOM

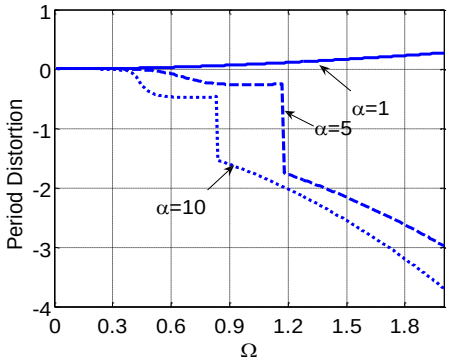

(a) $\alpha \geq 1$

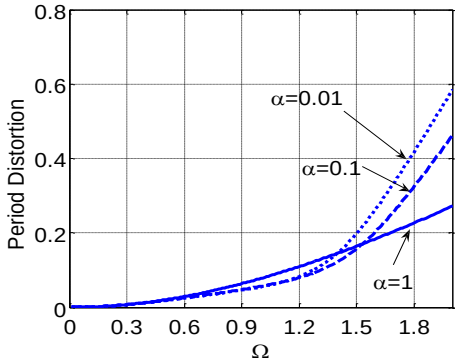

(b) $\alpha \leq 1$

Fig. 5.18 - Relationship between period distortion and Ω with varying α for mFOM

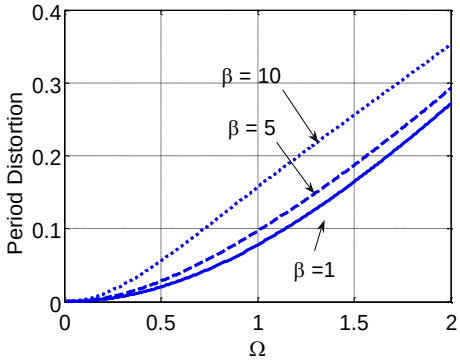

Fig. 5.19 - Relationship between period distortion and Ω with varying β for mFOM

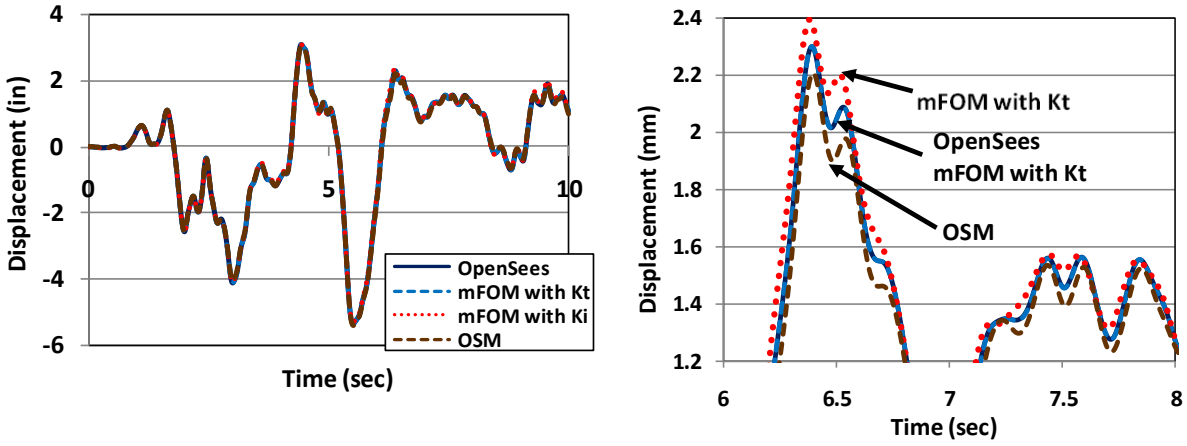

(a) solutions from various schemes

(b) magnified solution curves

Fig. 5.20 - Simulated seismic response of the 6-story model

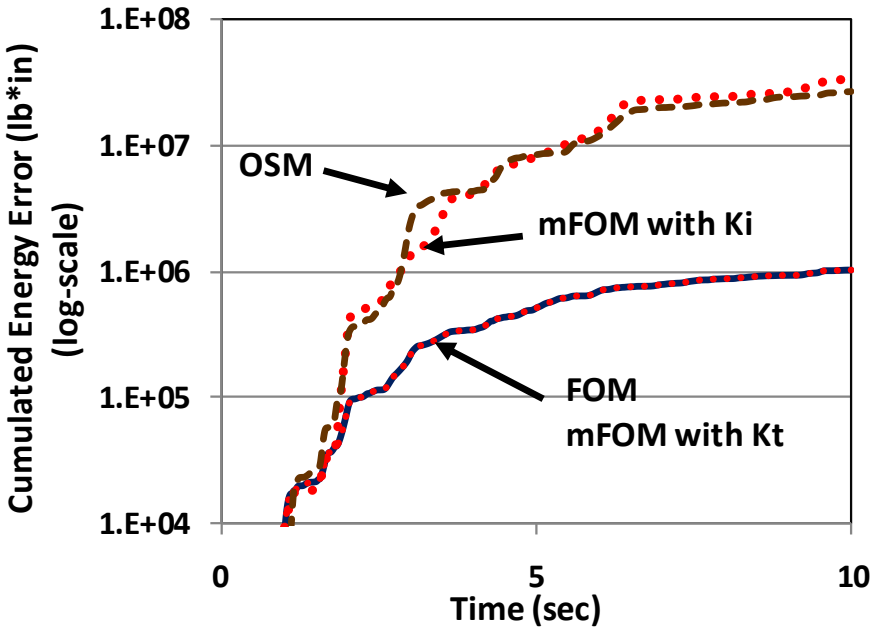

Fig. 5.21 - Cumulative energy errors for the 6-story model

5.11 REFERENCES

Broyden CG. A class of methods for solving nonlinear simultaneous equations. Mathematics of Computation 1965; 19:577-593.

Carrion JE, Spencer BF. Real-time hybrid testing using model-based delay compensation. Proceedings of the 4th International Conference on Earthquake Engineering, Taipei, Taiwan, 2006.

Chopra AK. Dynamics of structures: theory and applications to earthquake engineering. Englewood Cliffs, NJ: Prentice Hall, 2006.

Combescure D, Pegon P. α-operator splitting time integration technique for pseudodynamic testing. Error propagation analysis, Soil Dynamics and Earthquake Engineering 1997, v 16, n 7-8, 427-443.

Hilber HM, Hughes TJR, Taylor RL. Improved numerical dissipation for time integration algorithm in structural dynamics. Earthquake Engineering and Structural Dynamics 1977; 5:283-292.

Hung C-C, El-Tawil S. A method for estimating specimen tangent stiffness for hybrid simulation. Earthquake Engineering and Structural Dynamics 2009a; 38(1): 115-134.

Hung C-C, El-Tawil S. Full operator algorithm for hybrid simulation. Earthquake Engineering and Structural Dynamics 2009b; 38(13):1545-1561.

Igarashi A, Seible F, Hegemeier GA. Development of the pseudodynamic technique for testing a full scale 5-story shear wall structure. Proceedings of U.S.-Japan Seminar on the Development and Future Directions of Structural Testing Techniques, 1990.

Kwon O, Elnashai AS, Spencer BF. A framework for distributed analytical and hybrid Simulations. Structural Engineering and Mechanics 2008; 30(3):331-350.

Nakashima M, Kaminosono T, Ishida M, Ando K. Integration techniques for substructure pseudo dynamic test. 4th U.S. National Conference on Earthquake Engineering, Palm Springs, California, 1990; 515-524.

Nakashima M, Kato H, Takaoka E. Development of real-time pseudo dynamic testing. Earthquake Engineering and Structural Dynamics 1992; 21:79-92.

Nocedal J and Wright SJ. Numerical Optimization. Springer-Verlag. ISBN 0-387-98793-2, 1999.

OpenSees version 1.7 User Manual, Pacific Earthquake Engineering Research Center, University of California, Berkeley, 2006, http://opensees.berkeley.edu.

Shing PB, Mahin SA. Computational aspects of a seismic performance test method using on-line computer control. Earthquake Engineering and Structural Dynamics 1985; 13:507-526.

Wu B, Bao H, Ou J, Tian S. Stability and accuracy analysis of central difference method for real-time substructure testing. Earthquake Engineering and Structural Dynamics 2005; 34:705-718.

CHAPTER 6

HYBRID SIMULATION OF HPFRC COUPLED WALL SYSTEMS

6.1 INTRODUCTION

Two traditional approaches for investigating structural response are physical testing and numerical simulation. Each technique has its limitations and so the results of one method is frequently used in conjunction with the other's to reach a full appreciation of system response.

Physical testing involves testing a specimen under simulated loading and boundary conditions that model the hazard in question. The modeling approximations can influence the physical specimen's response thereby introducing uncertainty about the specimen's true insitu behavior. In earthquake engineering, the two common physical testing methods are member/subassemblage tests and shake table tests. In the first, a member or structural subassemblage with idealized boundary conditions is tested under a specified pseudo static or dynamic loading regime. Relatively large-sized specimens can be tested in this method because only a single member or a small subassemblage of members is tested at a given time. By its very nature, this method cannot accurately model full system response under seismic loading because of the assumed loading and boundary

conditions. Furthermore, the effect of loading rate is not accounted for in the test if the loading rate is pseudo static. For many materials, such as concrete and steel, the influence of seismic loading rate is not significant, but certain other materials, such as viscoelastic materials, are sensitive to the loading rate and must be tested under dynamic loading. Shake table testing, on the other hand, is a more realistic test environment since it allows system testing under simulated earthquake motion. However, the size of the shake table poses a severe limitation on the applicability of the method. In many cases, only small-scale specimens can be tested on a given shake table, which introduces scaling issues that could distort the fidelity of the test results.

The widespread availability of numerical simulation tools has led to a surge in the application of computational tools for investigating the response of new structural systems. However, computational models can be quite sensitive to a host of modeling assumptions, which means that simulation tools should only be exercised by competent analysts who have experience with the intricacies and sensitivities of their tools. In general, the results of simulation models are not acceptable unless a thorough validation exercise is undertaken and the bounds of applicability of the model are established.

The hybrid simulation technique combines features of the member/subassemblage and simulation evaluation methods to provide an attractive option that overcomes many of the individual limitations of each technique by itself. The technique is ideal for structures comprised of a part that is straight forward to simulate and another that is difficult to model and must therefore be physically tested, e.g. critical structural components whose

response is difficult to simulate because of extreme nonlinearity. The method permits testing of specimens in an environment that approaches shake table testing, but without the size constraint. Moreover, the technique permits more accurate representation of the loading and boundary conditions while allowing the use of commonly available static or dynamic actuators.

In this chapter, the effectiveness of using the hybrid simulation technique to predict the seismic behavior of HPFRC coupled wall systems is numerically investigated. While no physical testing is actually conducted, a simulation of the technique itself is done by combining the capabilities of two different computer programs. The objective is to demonstrate that the technique is applicable to coupled wall systems and to show that it is feasible to combine the capabilities of disparate computer models using the hybrid simulation method. The veracity of the solution obtained from hybrid simulation is demonstrated by comparing it to the response computed from conventional computational simulation.

6.2 PLATFORM FOR HYBRID TESTING

UI-SimCor (Kwon et al. 2008) is used as the platform to conduct the hybrid simulation exercise. The main task of UI-SimCor is to transmit target response values and the resulting system response between the tested (in this work, simulated) substructures and the main coordinator computer. In addition, algorithms for hybrid simulation can be implemented in conjunction with UI-SimCor by embedding them as a subroutine within UI-SimCor.

As shown in Fig. 6.1, the coordinator computer, which uses the selected hybrid simulation algorithm for solving the equation of motion, computes the target structural response at a particular time step. After that, the target value is imposed on the tested (simulated) substructures, and the resulting reaction force is measured. The measured reaction force is then transmitted to the main computer to calculate the system response in the next time step. The above procedure is repeated to extract the entire seismic response of the tested (simulated) structure.

The default interface provided by UI-SimCor allows the use of ABAQUS, OpenSees, FEADES Lab, and ZEUS-NL to model the computational substructure. In order to use LS-DYNA for computational HPFRC substructures, a new interface is developed to connect LS-DYNA to the coordinating computer. The interface is developed in Matlab using object-oriented programming. The developed interface has 3 main tasks. First, it receives the target responses from the coordinating computer. After that, it imposes the target responses on the numerical model and restarts a pseudo-static analysis in LS-DYNA. The resulting reaction forces are then read by the interface and sent back to the coordinator computer.

6.3 HYBRID SIMULATION OF THE HPFRC COUPLED WALL SYSTEM

To conduct hybrid simulation, the entire structure is divided into two substructures, i.e. the bottom 4 levels as the first substructure (B-Sub) and the remainder of the structure as the second substructure (T-Sub). The B-Sub, which is intended to represent the

physically-tested substructure in the laboratory, is modeled using macro-scale elements in LS-DYNA as was done in Chapter 3. On the other hand, the T-Sub is modeled in OpenSees using structural-scale elements. As shown in Fig. 6.2, the two shear walls for the T-Sub are represented by beam-column elements which are capable of representing behavior under combined axial force and bending moment. The beam-column elements are located at the gross section centroid of each shear wall.

The numerical model of the prototype HPFRC coupled wall system from Chapter 3 is slightly modified for the hybrid simulation exercise presented in this chapter. Recall that the first 4 stories and all coupling beams of the prototype structure in Chapter 3 are comprised of HPFRC, while the remainder of the system is made of RC. Since OpenSees does not possess a suitable material model to account for the hysteretic behavior of HPFRC, RC coupling beams are used instead of HPFRC in the beams above the 4^{th} floor level.

Some assumptions are made in order to permit use of OpenSees' beam-column elements to represent the response of RC coupling beams with diagonal reinforcement cages. The moment capacity of each coupling beam is computed using the longitudinal reinforcement and the longitudinal component of the diagonal reinforcement of the beam. For shear behavior, the coupling beam is designed to yield, in an elastic perfectly plastic manner, once the design shear demand is reached. To ensure that these assumptions are reasonable, the cyclic behavior of the coupling beam model from the T-Sub (OpenSees) is compared to that from the reference solution computed from the macro-scale model

(LS-DYNA). As shown in Fig. 6.3, the coupling beam model in OpenSees provides a strength capacity that matches the reference solution from the macro-scale model. However, the pinching behavior generated by the structural-scale model (OpenSees) is slightly more pronounced than that from the macro-scale (LS-DYNA) model. The comparison implies that the T-Sub's coupling beam model is able to capture the overall cyclic behavior from the reference model with acceptable resolution despite the simplifications made in modeling the coupling beams in T-Sub.

In order to form the equation of motion for the entire structure, the mass of the B-Sub is represented using 2 lumped mass blocks. Each mass block has 3 DOFs: 2 translational DOFs and 1 rotational DOF as can be seen in Fig. 6.4. For the T-Sub, lumped mass blocks are located at the beam-column connections as well as the boundary connecting to the B-Sub. The lumped mass blocks at the beam-column connections are displacement controlled in the horizontal DOF while the lumped mass blocks at the boundary posses 3 DOFs (Fig. 6.5). Each substructure is modeled in different computers with different IP addresses, and connected using UI-SimCor through a network as shown in Fig 6.2.

The FOM (Hung and El-Tawil 2009) is used to compute the seismic behavior of the coupled wall system and the 1940 El Centro earthquake history record with PGA=0.36g is used as the ground motion excitation. The simulated seismic response of the entire structure from conventional finite element analysis in LS-DYNA is used as the reference solution to judge the performance of the hybrid model. The comparison of the displacement history responses from the two methods is shown in Fig 6.6. It can be seen

that the computed result from the hybrid simulation technique captures the frequency content of the seismic behavior of the coupled wall system provided by the reference solution. The maximum story drift and roof displacement predicted by the methods are listed in Table 1. The hybrid simulation technique generates a maximum story drift 7% smaller than the reference solution, and its prediction of maximum roof displacement is 9% less than the reference solution.

The discrepancy between the solutions of the hybrid simulation model and the reference model can be attributed to the assumptions made in the hybrid simulation model. First, the reference model computes the response solution using a continuum representation while the hybrid simulation technique simplifies the model into a system with a limited number of DOFs. Besides, in the reference model, the selected incremental time step for solving the equations of motion representing the system is optimized by LS-DYNA to provide high resolution. On the other hand, careful judgment needs to be made in hybrid simulation to prevent the use of too-small a step size to avoid extended simulation time and amplified error propagation.

Although the use of hybrid simulation yields a fair prediction of the coupled wall system's seismic behavior, the quality of the solution can be improved by refining the hybrid simulation model. For example, the simulation resolution can be enhanced by shortening the incremental time step from the current 0.01sec to 0.005sec. However, as mentioned above, this will significantly increase the entire simulation time and amplify the displacement control errors associated with the actuators in physical hybrid

simulation. In addition, considering the number and characteristics of actuators commonly available in most laboratories, the current controlled DOFs for B-Sub are limited to the 4th floor level only. The simulation resolution can be improved if the DOFs of the lateral displacements at the bottom 3 floor levels are included, but that will require more actuators to be available and will necessitate high control accuracy at the bottom floor since displacements are expected to be small.

It is also important to note that the overall simulation accuracy is influenced by the capabilities of the simulation models themselves. While the shear walls and coupling beams in T-Sub are modeled using structural-scale elements, they are modeled using macro-scale elements in the reference model. A better simulation result could likely be obtained if a macro-scale model is used for T-Sub instead of a structural scale model. However, this will certainly increase the simulation time.

6.4 SUMMARY

The effectiveness of using hybrid simulation to predict the seismic behavior of HPFRC coupled wall system was explored in this chapter. A prototype model based on the 18-story HPFRC coupled wall system from Chapter 3 was adopted for this purpose. The prototype system was divided into T-Sub and B-Sub, which were modeled using structural-scale elements in OpenSees and macro-scale elements in LS-DYNA, respectively. In order to use finite element models from LS-DYNA for hybrid simulation through UI-SimCor, an interface was developed in Matlab using object-oriented programming. The tasks of the interface were to receive the computed target response

from the coordinator computer, restart the LS-DYNA substructure with target response, and send the resulting reaction force back to the coordinator computer. During the hybrid simulation, the substructures were modeled in different computers connected through UI-SimCor within a network. The computed solutions (from hybrid simulation and conventional finite element analysis) were compared using parameters such as maximum story drift, maximum roof displacement, and displacement history responses. The comparison showed that the hybrid simulation technique can capture the overall response of the system in terms of frequency content and displacement amplitude. Discrepancies between the solutions were attributed to the assumptions made in setting up the hybrid simulation model.

Table 6.1 – Comparison of the story drift and roof displacement

Max Response	Story drift (%)	Roof displacement (in)
Hybrid Simulation (T=2.0 sec)	0.275	4.70
Reference Solution (T=3.1 sec)	0.296	5.19

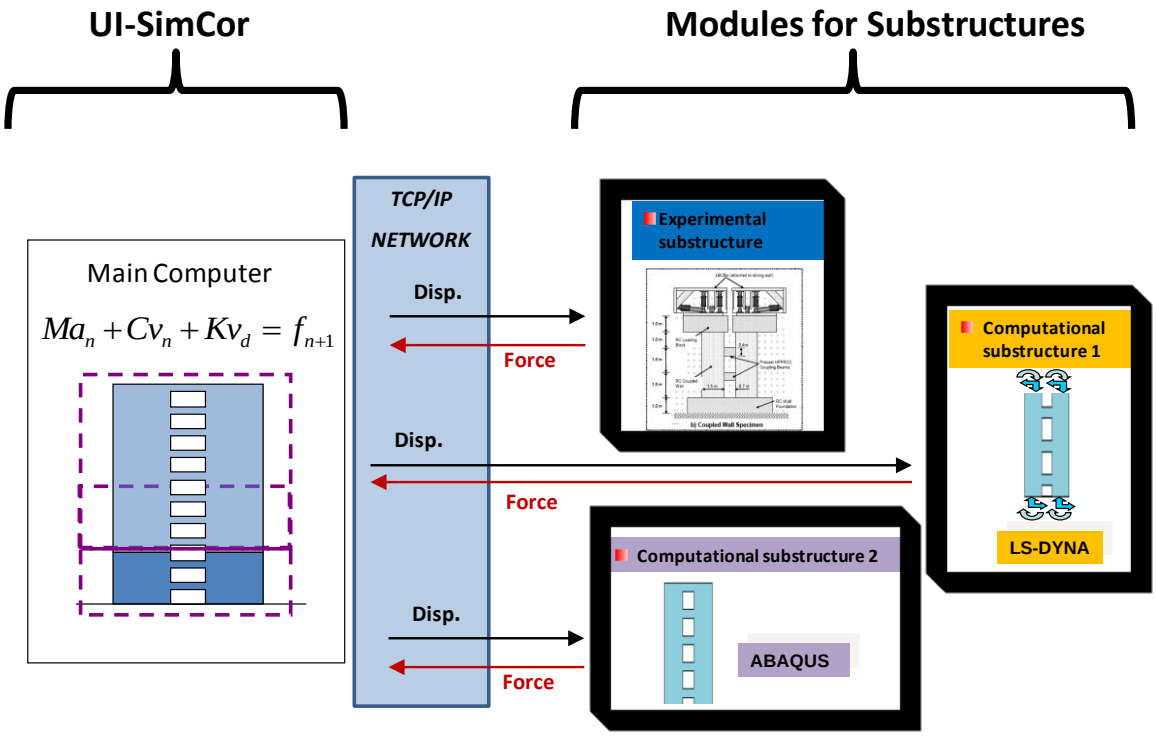

Fig. 6.1 – Implementation of hybrid simulation using UI-SimCor

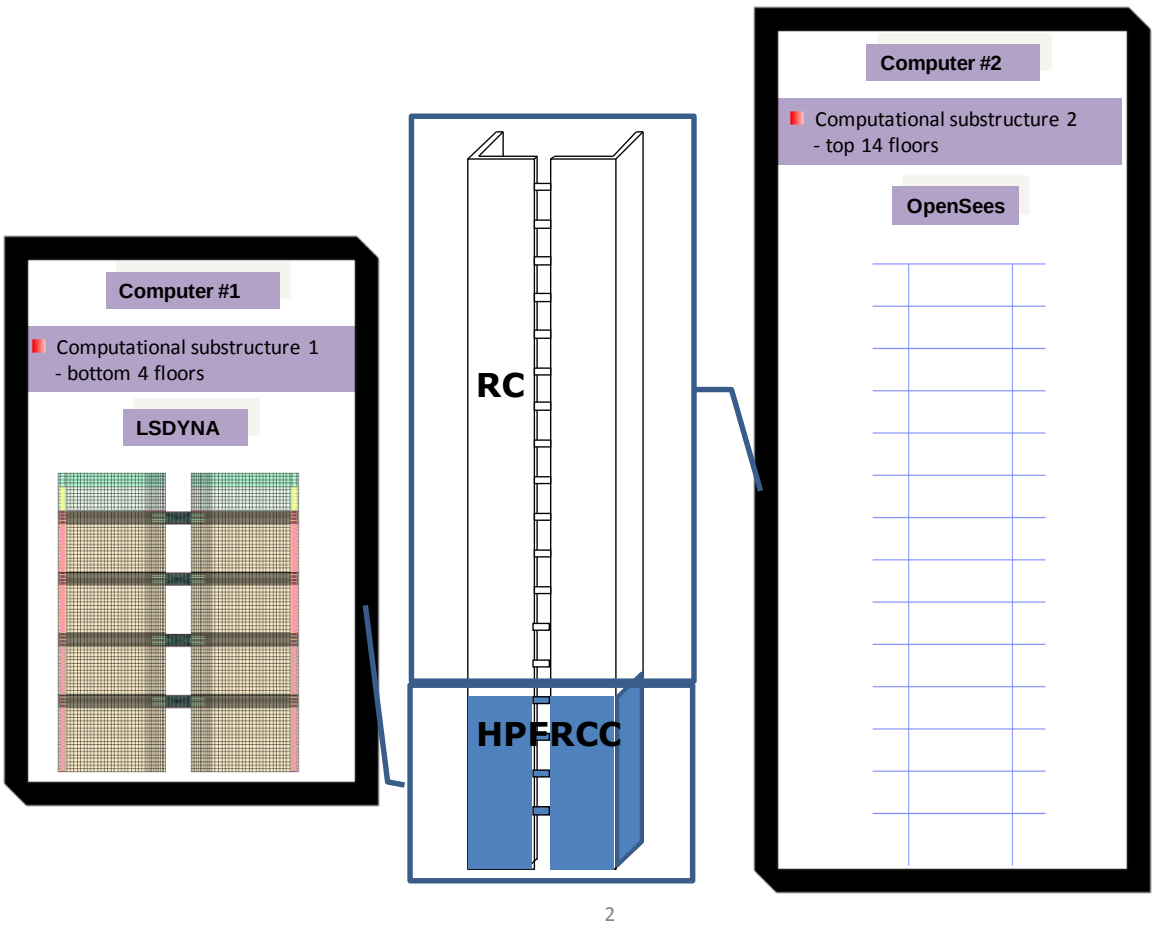

Fig. 6.2 –Numerical hybrid testing of the modified coupled wall system

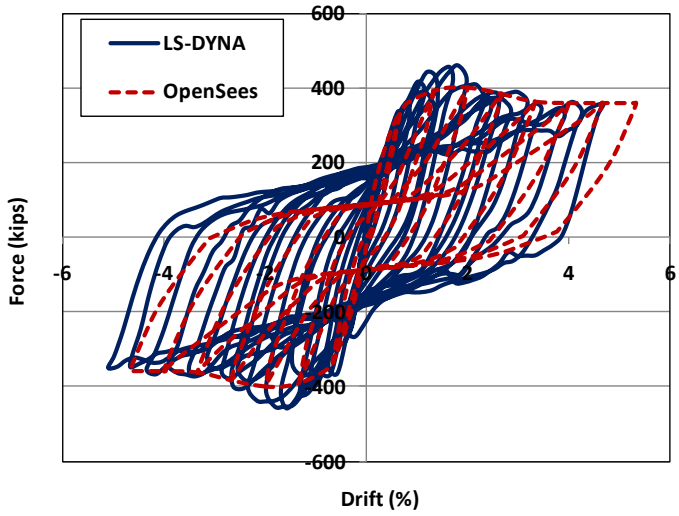

Fig. 6.3 – Cyclic behavior of the coupling beam models from OpenSees and LS-DYNA

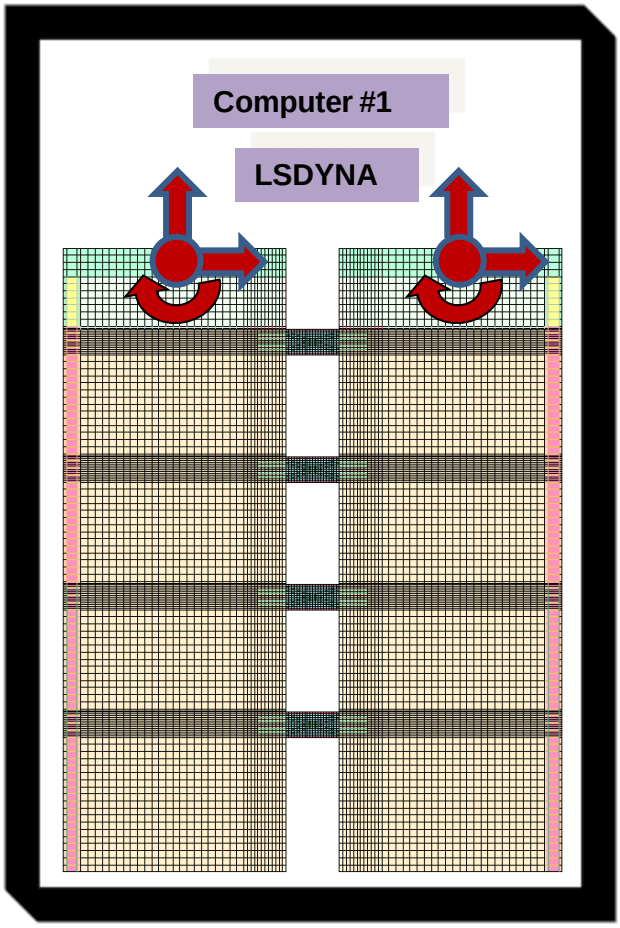

Fig. 6.4 – Controlled degrees of freedoms of the bottom substructure

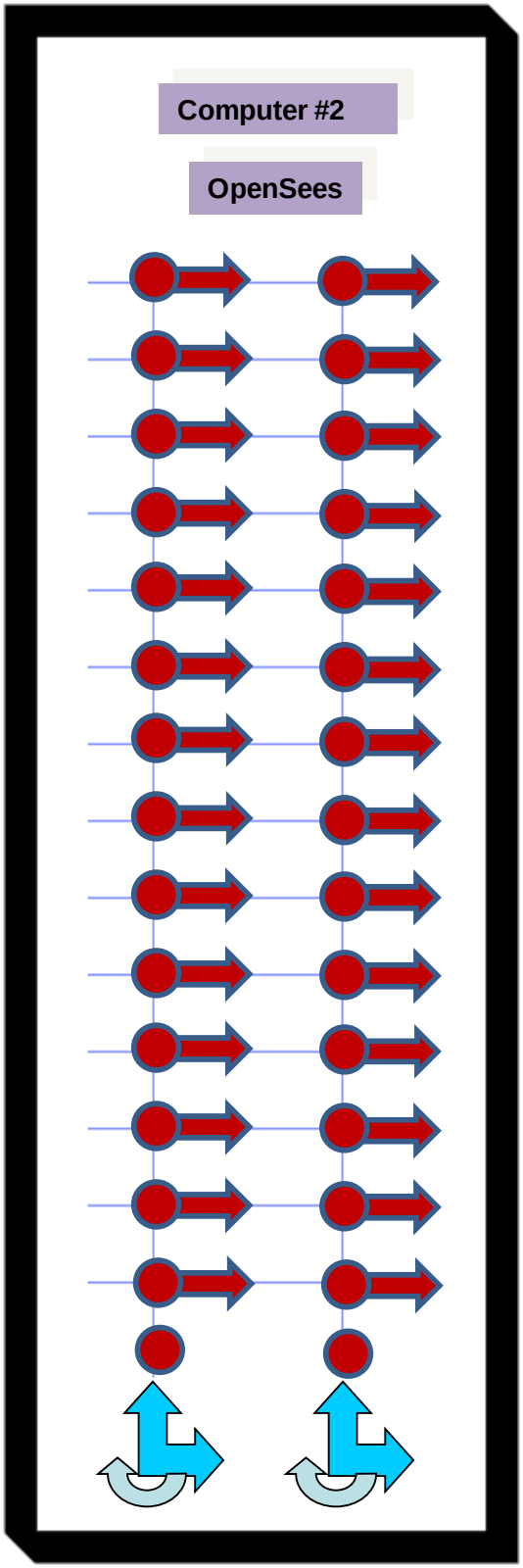

Fig. 6.5 – Controlled degrees of freedoms of the top substructure

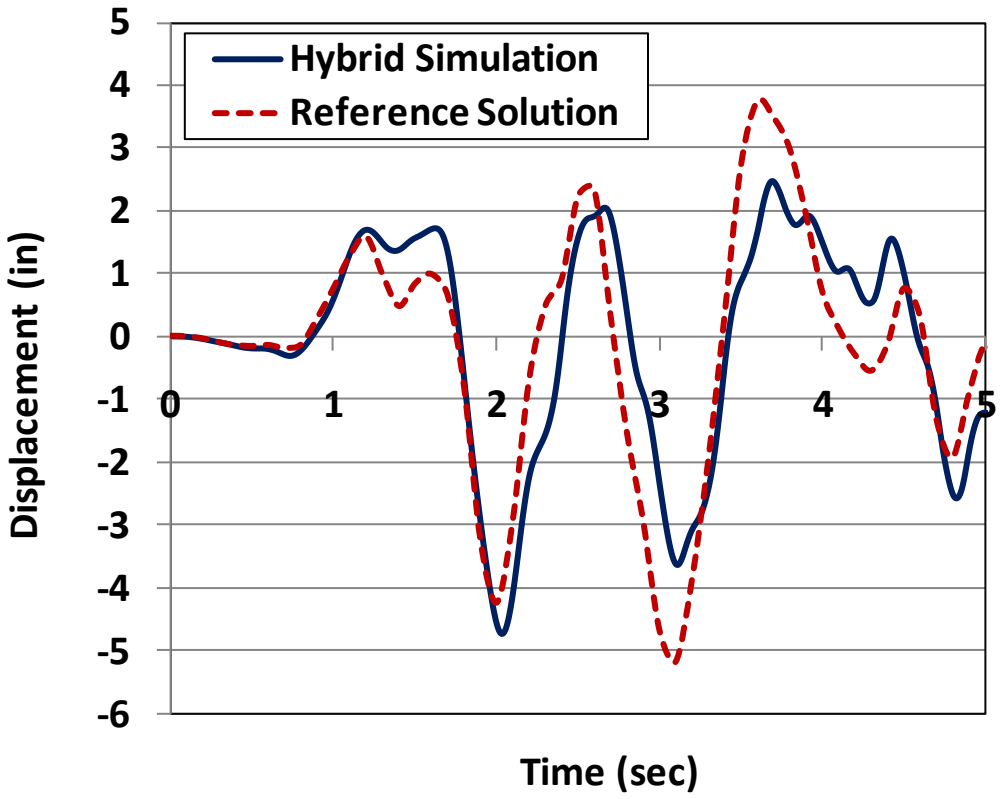

Fig. 6.6 – Comparison of the displacement responses from hybrid simulation and the reference solution

6.5 REFERENCES

Hung C-C, El-Tawil S. Full operator algorithm for hybrid simulation. Earthquake Engineering and Structural Dynamics 2009; 38(13):1545-1561.

Kwon O, Elnashai AS, Spencer BF. A framework for distributed analytical and hybrid Simulations. Structural Engineering and Mechanics 2008; 30(3):331-350.

OpenSees version 1.7 User Manual, Pacific Earthquake Engineering Research Center, University of California, Berkeley, 2006, http://opensees.berkeley.edu.

CHAPTER 7

SUMMARY, CONCLUSIONS, AND FUTURE RESEARCH

7.1 SUMMARY

This dissertation investigated the advantages of using HPFRC material to replace traditional concrete in critical components of a structure. Specifically, computational and hybrid simulation techniques were employed to explore the potential for using HPFRC material in coupling beams and plastic hinge zones of coupled wall systems. A new model that describes the planar response of HPFRC was developed and used to represent material behavior in computational system studies of prototype coupled wall systems. Two new algorithms were proposed to address the limitations of existing hybrid simulation techniques, including a particularly promising method, termed full operator method (FOM). Hybrid simulation of the seismic response of hybrid coupled wall systems with HPFRC was demonstrated using the new FOM technique. Following are more specific details of the innovations in this thesis and the major conclusions that can be drawn.

7.1.1 Inelastic HPFRC material model

An inelastic HPFRC material model was developed to predict the hysteretic behavior of HPFRC structural components under reversed displacements. In order to develop the material model, stress-strain relationships of HPFRC materials in both tension and compression were defined based on the available experimental data. The initiation and growth of cracks in the HPFRC material were described using a smeared crack approach. In addition, the orientation of cracks was defined using a new mixed fixed/rotating crack approach. The newly developed macro-scale constitutive model for HPFRC, based on a plane stress representation, was shown to be able to adequately account for the phenomenological behavior of HPFRC at the macro-scale level and capture responses such as cracking, softening, and hardening. The material model was implemented as a user-defined material model in LS-DYNA. The performance of the material model for modeling HPFRC structural components' behavior under displacement reversals was demonstrated through comparisons between experimental results and computational solutions for a variety of structural components, including a coupling beam, a double cantilever beam, and a slender shear wall. The comparisons were made by focusing on parameters such as loading/unloading/reloading slopes, pinching behavior, strength capacity, and shear deformation. It was demonstrated that the newly implemented model is capable of capturing the hysteretic behavior of HPFRC structural components with reasonable accuracy.

7.1.2 Seismic performance of HPFRC coupled wall system

Two 18-story coupled wall systems were designed using contemporary seismic design specifications. The first system was a traditional RC coupled wall system while the second one was constructed with HPFRC material in its coupling beams and the first four floor levels of the shear walls. Given the enhanced tensile, shear and moment resistance of HPFRC over regular concrete, the reinforcement detailing and amounts in the HPFRC coupled wall system were simplified and reduced from those in the RC system. In particular, the diagonal reinforcement cages with heavy confinement in the RC coupling beams were replaced by single layer steel rebars without confinement. Also, the transverse reinforcement in the HPFRC coupling beams was reduced from the RC coupling beams by 30%. For the shear wall, the vertical reinforcement in the boundary zone and the flange of the HPFRC system was 20% less than that in the RC system. Additionally, the confinement in the boundary zone was reduced by 50%. The seismic performance of the systems was examined using the requirements associated with Life Safety and Collapse Prevention performance level in FEMA 356 (2000). It was found that the seismic behavior of both systems satisfied the acceptance criteria in terms of story drift, coupling beam rotation, and plastic hinge zone deformation, despite the reduced reinforcement and simplified detailing in the HPFRC system. The benefit of using HPFRC to replace RC in the critical regions was clearly seen in the plastic hinge zone deformation. Specifically, it was shown that the pseudo strain-hardening behavior of HPFRC in tension helped extend the size of the plastic hinge zone from the wall base to the fourth floor level, reducing peak rotational deformation demands at the shear wall base as deformation demands increased. In contrast, the plastic hinge in the RC system

concentrated at the wall base as the system response increased. The advantage of using HPFRC also showed in terms of crack localization patterns during and after the prescribed ground motion events. It was found that the HPFRC system suffered much less localized cracks in the coupling beams and shear walls compared to the RC system. It was concluded that using HPFRC to replace RC in critical regions of a structure is able to reduce and simplify the reinforcement amount and detailing while enhancing permanent damage patterns in the aftermath of seismic events.

7.1.3 Enhancements in hybrid simulation techniques

A strategy for estimating the tangent stiffness of structures during hybrid simulation was proposed. The proposed strategy extracts the current tangent stiffness by solving a set of equations related to the displacement responses and reaction forces of the system from a few steps prior to the current time step. The technique for estimating the tangent stiffness was combined with the Operator-Splitting Method (OSM) for hybrid simulation and was shown to result in enhanced simulation accuracy when compared to the traditional OSM. The influence of the accuracy of the estimated tangent stiffness and the damping coefficient on the stability and accuracy characteristics of the modified OSM technique was investigated analytically.

A new predictor-corrector algorithm, termed the Full Operator Method (FOM), was proposed to resolve some of the issues associated with the widely used OSM. The new method was distinguished from OSM by two aspects. First, it increases the accuracy of the predictor response by applying an estimated tangent stiffness to calculate the

predictor acceleration term. A variety of schemes for estimating structures' tangent stiffness were suggested, such as BFGS, Broyden, DFP, and SR1. Second, the corrector response of FOM only resorts to the reaction forces from the tested/simulated structures/substructures without other assumptions like those made in OSM. The enhanced performance of FOM was demonstrated through several numerical hybrid simulation exercises. It was concluded that FOM is able to simulate the seismic behavior of structures with excellent accuracy, especially for structures showing significant nonlinear behavior, particularly when compared to OSM. Furthermore, it was found that when displacement control errors inherent in the hydraulic actuators were induced, the resulting adverse effect on FOM was less than that on OSM. This was attributed to the fact that the corrector response in FOM is only dependent on the true reaction forces.

The stability of FOM was investigated analytically and was found to be conditionally stable. A modified form of FOM, termed mFOM, was proposed to address this stability issue. It was shown that mFOM is unconditionally stable when the estimated tangent stiffness is larger than the real tangent stiffness of the structure. It was suggested that when FOM is applied to a structure dominated by higher mode response, and at the same time, the structure's tangent stiffness is difficult to estimate, the tangent stiffness can be substituted by the initial stiffness of the structure to reach unconditional stability and to allow the use of a larger incremental time step to speed up the hybrid test. The performance of mFOM was demonstrated through hybrid simulation of a 6-dof model. It was concluded from the validation examples that mFOM was able to predict structural seismic behavior with accuracy that is at least as good as OSM.

7.1.4 Hybrid simulation of HPFRC coupled wall system

Hybrid simulation of a HPFRC coupled wall system was demonstrated. The system was divided into 2 substructures, each of which was modeled using a different computer program and model type. The bottom four floors were treated as the first substructure (B-Sub) and the remainder of the system was the second substructure (T-Sub). The B-Sub was simulated using macro-scale elements in LS-DYNA while the T-Sub was modeled using structural-scale elements in OpenSees. The different substructure responses were connected using UI-SimCor within a network. The computed seismic behavior from hybrid simulation was compared with that from the conventional computational method. It was found that while the frequency content and the general displacement amplitude from the hybrid simulation were able to match the reference solution quite well, the hybrid simulation technique was not able to reproduce fine details of the response, especially at the peaks. This discrepancy was attributed to the assumptions that were necessarily made to enable the hybrid simulation involving both OpenSees and LS-DYNA. For example, the continuum system was simplified and represented as a system with 30 lumped mass blocks. Also, T-Sub was modeled using beam-column elements instead of plane-stress elements as was done in the conventional computational method. Further, the shear and moment behavior of the coupling beams were also greatly simplified due to the limitations of the beam-column elements employed in T-Sub. Nevertheless, the exercise demonstrated that hybrid simulation between disparate finite element programs and models is feasible and can produce reasonable nonlinear results in spite of the approximations made.

7.2 CONCLUSIONS

Major findings from this research are as follows.

- The newly proposed mixed fixed/rotating crack model for HPFRC materials is able to predict the hysteretic behavior of various types of HPFRC structural components with reasonable accuracy.
- Despite a significant reduction in the amount of reinforcing steel and simplifications in seismic detailing, using HPFRC materials to replace RC in coupled wall systems can nevertheless enhance the seismic performance of coupled wall systems. This is manifested as a reduction in local deformation demands in the plastic hinge zones and reduced permanent damage after a seismic event.
- The newly developed FOM is conditionally stability. There are two reasons for its enhanced accuracy compared to OSM: 1) it increases the accuracy of the predictor response, and 2) eliminates inaccurate assumptions in the corrector response.
- It is possible to modify FOM into an unconditionally stable algorithm, termed mFOM. The modified method is unconditionally stable when the estimated tangent stiffness is larger than the real tangent stiffness. The stability of mFOM can therefore be guaranteed if the initial stiffness of the structure is used in the mFOM when analyzing structures with degrading stiffness characteristics, a category in which most civil structures fall. The simulation accuracy of mFOM is at least as good as OSM in the examples studied.

- Hybrid simulation between two disparate computational sub-models of a hybrid coupled wall system is able to provide a fair prediction of response in terms of the system's maximum displacement response, story drift, frequency content, and displacement amplitude. However, details of the response can only be roughly modeled due to the assumptions that were necessarily made to enable the simulation to occur.

7.3 Future Research

The work that was conducted in this dissertation offers a strong foundation from which to launch a variety of research directions. These research opportunities can be categorized in four parts: further development of a HPFRC material model, effectiveness of using HPFRC in structures for enhanced seismic behavior, development of hybrid simulation algorithms, and enhancements in using hybrid simulation for coupled wall systems. The following is a description of these recommended areas of research.

7.3.1 Development of a HPFRC material model

Although the proposed material model is capable of accounting for some of the most important sources of nonlinear behavior in HPFRC structural components, it is incapable of addressing some other phenomena such as concrete splitting, sliding shear failure, and tension softening. This deficiency is not due to limitations on the model itself, but rather a lack of pertinent test data by which to calibrate the model. Once such data becomes available, a refined HPFRC material model, which is able to address the above issues, can be developed. Another refinement that can be pursued is to correlate the parameters

controlling the model to characteristics of the HPFRC materials, such as fiber types and the volume fraction of fibers. The HPFRC material model was shown to be able to simulate the hysteretic behavior of coupling beams, double cantilever beams, and slender shear walls. However, the performance of the model in other structural components, such as beam-column connections, which possess more complicated behavior, remains to be explored. In addition, the model herein is based on plane stress elements, and thus it is limited to analyze 2-D problems. A HPFRCC material model which is able to account for full 3-D cyclic behavior is recommended for future work.

7.3.2 Effectiveness of using HPFRC in structures for enhanced seismic behavior

In this dissertation, HPFRC materials were used in coupled wall systems. It is of interest to explore other types of structures that could benefit from HPFRC. For example, using HPFRC can greatly reduce the reinforcement detail and amount in the beam-column connections. A potential research direction is to conduct system level simulations to investigate the influence of using HPFRC beam-column connections on structural behavior since most existing research work has only focused on behavior at the level of a single beam-column connection. Furthermore, the behavior of HPFRC structures subjected to other types of severe events is also worth exploring, e.g. the response of structures to blast and impact.

7.3.3 Experimental validation of FOM

The enhanced performance of FOM was demonstrated under simulated conditions. It is necessary to conduct physical tests to make sure that the FOM would work under

practical hybrid simulation conditions. Moreover, the developed method has been applied to structures with overall hardening response and dominated by first mode behavior. Additional research is necessary to investigate if it will provide similarly good results for softening structures and to develop it for use in structures with higher mode response.

7.3.4 Effectiveness of using hybrid simulation for HPFRC coupled wall systems

The discrepancy between the solutions of the hybrid simulation and the conventional computational method can be attributed to the assumptions that were necessarily made in order to perform the simulation. Future research directions are recommended to refine the model in order to relax these assumptions. First, the number of lumped mass blocks of the B-Sub can be increased from the current two blocks, thus increasing the controlled DOFs of B-Sub and allowing more control over the simulation and improved accuracy. Further, the structural-scale model used to represent T-Sub can be further refined. For example, the beam-column elements used to represent the coupling beams can be improved to allow better representation of coupling beam response. The simulation accuracy can also be improved by reducing the size of the incremental time step. However, it should be noted that reducing the step size not only extends the entire simulation time but also amplifies the control errors related to hydraulic actuators in physical hybrid simulation.

APPENDIX

APPENDIX A

IMPLEMENTATION OF THE NEWLY DEVELOPED HPFRC MATERIAL MODEL IN LS-DYNA

This section gives an overview of the configuration of the user-defined material model in LS-DYNA. The procedure of implementing the inelastic HPFRC material model is also reviewed and detailed.

A.1 CONFIGURATION OF THE USER-DEFINED MATERIAL MODEL

The newly developed HPFRC material model is implemented using the user-defined material subroutine, called UMAT, in LS-DYNA. In the UMAT, the default inputs from the main LS-DYNA program are the previous incremental strain $\boldsymbol{\Delta\varepsilon}_{xy}^{(j-1)}$, the previous state of stresses $\boldsymbol{\sigma}_{xy}^{(j-1)}$ and strains $\boldsymbol{\varepsilon}_{xy}^{(j-1)}$. The inputs are employed by the user to compute the current material state, i.e., stresses $\boldsymbol{\sigma}_{xy}^{(j)}$, strains $\boldsymbol{\varepsilon}_{xy}^{(j)}$, using the material constants and history variables that are defined by the user. The main program then uses the current material state to compute the inputs for the next time step. The user-defined material subroutine, which is written in FORTRAN, is compiled and linked to the LS-DYNA executable file as a static library. The configuration of the UMAT and its

implementation with LS-DYNA can be referred to Fig. A.1 (Moraes and Nicholson, 2001).

A.2 PROCEDURE FOR IMPLEMENTING THE HPFRC MATERIAL MODEL

The procedure for implementing the newly developed HPFRC material constitutive model is recalled from Chapter 2 and further detailed. Fig 2.4 shows the steps constituting the implementation loop for the HPFRC material model using the UMAT. For programming purpose, the entire material subroutine divided into several sub-subroutines, as 1) Total global strain, 2) Principal direction/crack direction, 3) Principal strain and (if crack localization occurs) shear strain, 4) HPFRC material constitutive law, 5) Reduced shear modulus, and 6) Global stress. To start the procedure, the current global strains are first computed using the incremental global strains and the total global strains from the previous time step. Then, depending on whether the crack localization strain has been previously reached, either the principal direction (using Mohr circle) or the crack direction (same direction as in the previous time step) is determined. After that, the computed direction is employed with the HPFRC material constitutive law to calculate the stresses in the principal direction or the crack direction. The newly developed HPFRC constitutive model consists of 4 scenarios for monotonic tensile stress-strain relationships, 3 scenarios for monotonic compressive stress-strain relationships, 5 scenarios for cyclic tensile stress-strain relationships, and 4 scenarios for cyclic compressive stress-strain relationship. The details of these scenarios can be referred to Chapter 2. The last step of the implementation loop is to transform the local stresses into global stresses using Mohr circle.

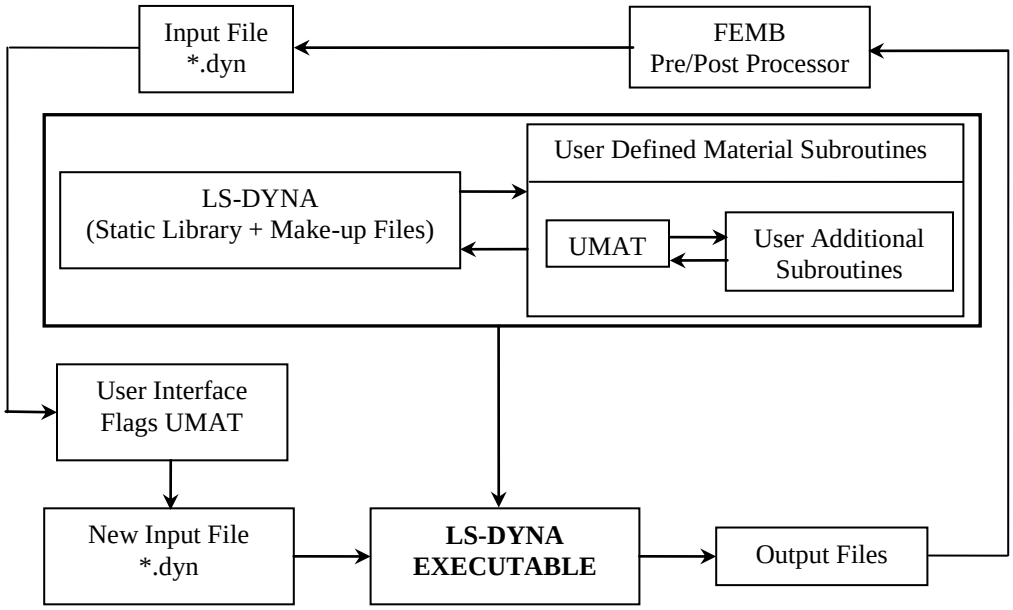

Fig. A.1- Configuration of the user-defined material subroutine and the main LS-DYNA program (Moraes and Nicholson, 2001)

A.3 REFERENCES

Moraes and Nicholson, “Simulation of projectile impact using continuum damage mechanics”, ASME Pressure Vessels and Piping Conference, 2001, pp. 39-46